ON HADRONIZATION PHENOMENOLOGY IN MONTE CARLO EVENT GENERATORS

by Cody B. Duncan

MA, MSc

A thesis submitted for the degree of

Doctor of Philosophy

February 2020

Thesis advisor: Dr. Peter Skands

Copyright notices

To my parents,

who taught me all that I know, and all that I've forgotten.

Contents

Abstract

As the Large Hadron Collider (LHC) at CERN collects unprecedented amounts of data with increasing precision, particle physicists are given the opportunity to test the theoretical frameworks that they have built over the last six decades. Monte Carlo event generators allow theory and experiment to make contact, and help provide a testing ground for the various models and physical processes involved in simulating high-energy particle collisions. Event generators are a key piece of the high-energy triumvirate, along with experiments and theory, serving both as a tool for novel physical models, and as an area of fundamental research in and of itself.

This thesis focuses on improving the low-energy modelling of a high-energy collision. As the protons collide, their constituents, quarks and gluons, emit bremsstrahlung radiation to reduce their energy and momentum, until they reach the confinement scale, an energy scale at which perturbation theory breaks down. At this point, Monte Carlo event generators use phenomenological models to convert these fundamental particles into the composite ones, called hadrons, that experiments detect, a process called hadronization. The two major models of hadronization in high-energy event generation are the cluster model and the Lund string model, and this thesis will study both as well as provide extensions to them.

We have addressed this topic with three projects: first, we describe a small change to the description of the production of strange quarks in the low-energy regime, and aim to bridge the gap that we see in this modelling for electron-positron & proton-proton collisions. We achieve a better description of hadrons containing strange quarks. Second, we build a framework to build up the spacetime structure of a proton-proton collision, and use this information to inform and govern the colour reconnection algorithm, which reconnects quarks and antiquarks in clusters different from their initially assigned ones. We compare our model to data and show reasonable agreement for minimum bias events, where the experimental triggers select events with the least possible bias. Third, we present a model for string-string interactions that preserves energy and momentum, but allows the strings, and thus the hadrons created from their fragmentation, to push on each other. We compare our model to the ordinary baseline Lund string model and show that the new model has some of the signatures seen in recent data from the LHC.

List of research outputs

1. Cody B Duncan, and Patrick Kirchgaeßer, *Kinematic Strangeness Production in Cluster Hadronization*, Eur. Phys. J. C 79 no. 1 (2019) 61, DOI: 10.1140/epjc/s10052-019-6573-2, arXiv:1811.10336 [hep-ph]

2. Johannes Bellm, Cody B Duncan, Stefan Gieseke, Miroslav Myska, and Andrzej Siódmok, *Spacetime Colour Reconnection in Herwig 7*, Eur. Phys. J. C 79 no. 12 (2019) 1003, DOI: 10.1140/epjc/s10052-019-7533-6, arXiv:1909.08850 [hep-ph]

3. Cody B Duncan and Peter Skands, *Fragmentation of Two Repelling QCD Strings*, submitted to SciPost Physics Journal, arXiv:1912.09639 [hep-ph]

Additional Publications

The following papers were produced during my candidature, but are not part of this thesis.

Confronting Experimental Data with Heavy-Ion Models Rivet for Heavy Ions
Christian Bierlich, Andy Buckley, Christian Holm Christensen, Peter Harald Lindenov Christiansen, Cody B Duncan, Jan Fiete Grosse-Oetringhasu, Przemyslaw Karczmarczyk, Patrick Kirchgaeßer, Jochen Klein, Leif Lönnblad, Roberto Preghenella, Christine O. Rasmussen, Maria Stefaniak, and Vytautas Vislavicus
Submitted to Physical Review C, arXiv:2001.10737 [hep-ph]

Declaration

This thesis contains no material that has been accepted for the award of any other degree or diploma at any university or equivalent institution and, to the best of my knowledge and belief, contains no material previously published or written by another person, except where due reference is made in the text of the thesis.

This thesis includes two original papers published in peer reviewed journals and one submitted publication. The core theme of the thesis is the development and investigation of hadronization phenomenology in Monte Carlo event generators for high-energy collisions. The ideas, development, and writing of all the papers in this thesis were the primary responsibility of myself, a PhD candidate in the School of Physics and Astronomy at Monash University, under the supervision of Peter Skands.

My contribution to each of the included works is stated below.

Publication Title: *Kinematic Strangeness Production in Cluster Hadronization*

Status: Published, Thesis Chapter 4

Student contribution: Developed the general model. Wrote the code implementation of the model. Performed the validation and preliminary phenomenological studies. Wrote the paper draft. 50%

Collaborator contribution:

Patrick Kirchgaeßer: Contributed to the model. Performed the final phenomenological studies and responsible for the tuning. Contributed to the write-up. 50%

Publication Title: *Spacetime Colour Reconnection in Herwig 7*

Status: Published, Thesis Chapter 5

Student contribution: Developed the general model. Wrote the code implementation of the model. Performed the validation and preliminary phenomenological studies. Wrote the paper draft. 50%

Collaborator contribution:

Johannes Bellm: Contributed to the discussion and code implementation. Performed the final phenomenological studies and responsible for the tuning. Contributed to the write-up. 20%

Stefan Gieseke: Contributed to the model and discussions. Contributed to the write-up. 10%

Miroslav Myska: Contributed to discussions and code. Contributed to the write-up. 10%

Andrzej Siódmok: Contributed to discussions, some phenomenological studies, and code. Contributed to the write-up. 10%

Publication Title: *Fragmentation of Two Repelling QCD Strings*

Status: Submitted, Thesis Chapter 6

Student contribution: Developed the ideas. Wrote the code implementation of the model. Performed the validation and phenomenological studies. Wrote the paper draft. 60%

Collaborator contribution:

Peter Skands: Developed the ideas. Contributed to discussions. Contributed to the write-up. 40%

I have not renumbered sections of submitted or published papers.

Signature:

Name: Cody B Duncan

Date: 13 February 2020, Melbourne

Acknowledgements

I have had an indescribably life-changing four years in Melbourne. All the people I have met and those who I have worked with have changed me irrevocably. These short sentiments cannot possibly cover everything I have felt or gone through with these people, but I'll try my best.

A large amount of my gratitude lies with my supervisor Peter Skands. He has been a patient teacher, with a keen insight into hadronization and low-energy QCD phenomenology, as well as an understanding human who has encouraged the best in me. I would also like to thank him for all the opportunities he has allowed me to take during my PhD, such as taking six months to go work with other academics, allowing me to expand my horizons and meet some incredible people. I would not have been able to complete this thesis without Monash University's financial support via a Australian Government Research Training Program (RTP) Scholarship and the J.L. William Scholarship from the School of Physics & Astronomy.

I'd like to thank my associate supervisors Tapio Simula and Helen Brooks. They offered a incredible amount of pastoral support, and I have had numerous stimulating conversations with both, about work, life, and everything in between. Similarly, my friends and collaborators Patrick Kirchgaeßer, Johannes Bellm, and Stefan Gieseke deserve special mention for their constant support and enthusiasm. A big thank you to Peter, Helen, and Christian Preuss for proof-reading this thesis.

Administrative staff rarely receive the attention they deserve, and this is doubly true of Jean Pettigrew and Karen Lee, who have been like another set of parents here at Monash. Their tender souls nurtured me throughout my PhD and made every day a joy. I'd also like to thank Monash Health for looking after me in times of sickness and for their reassuring hands guiding me throughout the process.

Without my friends, this thesis would not exist, so thank you all - Kavan, Felix, Agnes, Vanessa, Dale, Taryn, Harry, Albert, Mitch, Christian, Johanna, Marcel, Judith, Leonie, Clemens, and countless others who have been part of my time here. This thesis is as much your work as it is mine. Simon Milz & Phil Taranto, thank you for being my bridges over troubled water. Grace Hattingh, Annah Hattingh, Lochlan Kendrick, Jenna Pignotti, & Simon Shields, thank you for seeing me through thick and thin. Jana Hofmann, thank you for helping me see the forest for the trees and helping me make this thesis look as good as it does.

A special thank you goes out to Francesco Campaioli, my dearest and most understanding friend. So many facets of my life would be so different without you, and your strength & courage helped build me up when I needed it most. It has been a pleasure working and living with you for most of my time here.

Finally, my family, a bunch better than any person could dream of. Elena and Cora, my childhood would have been much harder and drearier without you. Maisy, Tamsin, Callum, and Jamie, I love you all, and I'm so proud of each of the people you are growing up to be. My grandparents, in particular Paw Paw - Helen Strange, for their adamant belief that I could be whatever I wanted to be. And my parents, Monique Strange and Malcolm Rose, who have been the most loving pair that a boy could ever wish for. I cannot begin to tell them how much they mean to me, but hopefully they know.

Das ist ja alles gut
und schön, aber überhaupt
wer hat mein Hinterrad geklaut?
$\sim$ Von Wegen Lisbeth

1

Introduction

The natural sciences are concerned with studying all the observable phenomenology that we have encountered in Nature. The overarching goal of science is to build models that describe these phenomena, while also yielding cogent and coherent predictions for future phenomena. The three most commonly known natural sciences are the ones taught in schools: biology, chemistry, and physics. All three are parts of a larger whole, but each are frameworks with a set of tools that are appropriate to the given task at hand. If one wishes to describe macroscopic and microscopic organisms and the interactions between these bodies, biology is the most appropriate tool to do so. If one asks what these organisms share in common, one needs biochemistry to be able to describe the production of proteins or other biochemical compounds, and how these react with one another. Zooming in on these chemicals' building blocks is fully the remit of chemistry, the study of the periodic table and its inhabitants: atoms.

However if one wants to understand the fundamental interactions between these atoms, one needs fundamental physics, primarily quantum mechanics. We may also ask the question that we have continued to ask, both in this introduction, and throughout human history - what's smaller?

An atom is comprised of negatively-charged electrons, which are electromagnetically bound to the positively-charged nucleus, a dense core of protons and neutrons. However, protons and neutrons are not fundamental particles, but instead strongly-bound composite particles called hadrons, made of quarks bound together by gluons. But at this level, we can no longer use just quantum mechanics to describe these particles nor their phenomenology. We need a new framework: quantum field theory, in particular the Standard Model of particle physics [1–9], where particles are represented by fields. The Standard Model (SM) encapsulates three of the four fundamental forces in Nature - electromagnetism, the weak nuclear force, and the strong nuclear force, and the SM describes these interactions between all known visible matter.

In Quantum Chromodynamics (QCD) [1], also known as the strong nuclear force, the fundamental particles are quarks and gluons, collectively referred to as partons [10, 11], and these fundamental partons are the building blocks for hadrons like protons and neutrons. Partons carry a fundamental charge called colour-charge. This charge is analogous to electric charge in Quantum Electrodynamics (QED), the quantum field theory of electromagnetism that governs the interaction between particles carrying electrical charges and photons - the force-mediating particle of the theory. Electric charge in QED is carried by, for example, electrons [1], but it is not carried by photons. In QCD, both quarks and gluons carry colour charge, meaning that there are interactions between quarks and gluons similar to QED, but also gluon self-interactions which have no analogy in QED. It is this self-interaction that causes most of the headaches associated with studying QCD while vastly enriching the theory.

One of the difficulties associated with studying quarks and gluons is that they cannot be extracted from a proton and studied individually. A key property of QCD is the notion of confinement, whereby particles that carry colour are not observable. We may instead try to approach this problem from a different angle: by probing the constituents of protons with accelerated particles. The Large Hadron Collider (LHC) [12] was created to accelerate protons to within a fraction of the speed of light, and then collide them head on, providing a means to probe the nuances of their internal substructure and to test the predictions of QCD.

Monte Carlo event generators [13–16] form the third member of the triumvirate of high-energy physics, along with theory and experiment. Event generators perform highly detailed simulations of the various physical processes involved in a collision. Since Nature is inherently quantum, event generators mimic this randomness by probabilistically producing events, starting from the initial protons, and ending with as detailed a final-state as possible. This property affords Monte Carlo event generators great flexibility in being able to perform a battery of tests and present

[1] Their antiparticle counterpart, the positron, also carries electric charge, see Chap. 2.

firm predictions to be tested against experimental data. To do so, event generators separate the numerous physical processes that occur during a collision in a hierarchy of energy or resolution scales. The hard process forms the backbone of an event - a short-distance, high-energy scattering that is calculated from perturbation theory. This is combined with parton distribution functions - quantities that cannot be calculated from first principles and must be experimentally extracted. While the hard process forms the base of an event, determining the largest energy scale, the proton is a composite object, meaning that when two collide there may be several parton-parton interactions, known as multiple parton interactions (MPI) [17].

In the hard process, the colliding partons undergo large momentum transfers and correspondingly are accelerated, and undergo bremsstrahlung. In QCD, quarks and antiquarks can radiate gluons, gluons can split into quark-antiquark pairs, and gluons can radiate other gluons. Event generators model this process via the parton shower [18–25], iteratively producing radiation probabilistically to evolve from one resolution scale to a lower one. This process cannot be continued to arbitrarily small resolutions scales, as parton showers hit an infrared cutoff in the form of the hadronization scale $\mathcal{O}(\Lambda_{\mathrm{QCD}}) \sim 200$ MeV. At this point, perturbative techniques become inadequate, and instead event generators use phenomenological models to convert all the individually coloured quarks and gluons produced from all the previous steps, into the composite colourless hadrons that can be, in principle, detected. This process is known as hadronization, and it is the phenomenology of this process that this thesis is concerned with.

There are two major models of hadronization used in general-purpose high-energy Monte Carlo event generators: the Lund string model [26,27], and the cluster model [28]. In both of these models, quark-antiquark pairs are produced during the hadronization process, creating hadrons as they do so. Many of these hadrons will be unstable, and as such will undergo further particle decays [29], with probabilities determined by experimentally measured branching ratios, where available.

At the LHC, and at any future colliders, QCD processes make up the majority of the observed data. In order to study rare processes or to search for any new physics, such as supersymmetric particles or other extensions to the Standard Model, modelling the background plays a vital role. Indeed, there are already signs that the hadronization models and general soft-physics modelling in contemporary Monte Carlo event generators are insufficient to model some of the recent results from the ALICE [30–33] and CMS [34–36] experiments at the LHC, with the ATLAS [37] experiment also following up on several of these results [38, 39]. The conventional Lund string and cluster models are unable to qualitatively describe key collective effects, such as strangeness enhancement or flow-like observables. The aim of this thesis is to build and study new hadronization models inspired by these anomalous results.

Outline of the Thesis

This thesis is structured as follows: in Chap. 2 we give a broad overview of the Standard Model, and review the key concepts of Quantum Chromodynamics and Monte Carlo event generators. In Chap. 3, we focus on the two major models of hadronization in high-energy event generators, and their shortcomings with regards to describing collective effects in proton-proton collisions. Chapters 4, 5, and 6 present published material. In Chap. 4, we present a reparameterization of the production of strange quarks during the non-perturbative stages of event generation. We then build a framework to introduce spacetime coordinates into the Herwig event generator in Chap. 5, and then use spacetime separation as a discriminant for the colour reconnection mechanism. Chap. 6 presents a new model for string-string interactions in the event generator Pythia, and we show that this model may be able to explain the flow-like observables seen at the LHC. Lastly, we end this thesis with a summary and concluding remarks in Chap. 7.

2

The Standard Model and Quantum Chromodynamics

The Standard Model of particle physics (SM) [1–9] is a relativistic quantum field theory [1] that is able to describe three of the four known forces in Nature: electromagnetism, the strong nuclear force, and the weak nuclear force. The particles described by the Standard Model are represented by fields, and obey a number of fundamental symmetries. These symmetries are made manifest with group theory, and the Standard Model uses the product of three gauge groups:

$$\mathrm{SU}(3)_{\mathrm{C}} \times \mathrm{SU}(2)_{\mathrm{L}} \times \mathrm{U}(1)_{\mathrm{Y}}, \tag{2.1}$$

which contains the strong nuclear force, governed by $\mathrm{SU}(3)_{\mathrm{C}}$, and the combined electromagnetic and weak nuclear forces, described by $\mathrm{SU}(2)_{\mathrm{L}} \times \mathrm{U}(1)_{\mathrm{Y}}$, collectively referred to as the electroweak sector [2, 8, 48, 49]. The strong force has eight generators [50] which correspond to the eight gluons - the force-mediating particle of QCD. In the electroweak gauge group, the subscripts L and Y denote the quantum numbers of left-handedness and hypercharge respectively. This gauge group has four generators [50], and thus four massless bosons: three weak isospin boson W_1, W_2, W_3, and a hypercharge boson B. However, due to spontaneous symmetry breaking (SSB) caused by the Higgs mechanism [4, 6, 7, 9] which introduces the scalar Higgs boson,

[1] Quantum field theory is now a mature field, and an interested reader is directed to the many excellent pedagogical textbooks available [40–47].

the electroweak gauge group collapses:

$$\mathrm{SU}(2)_L \times \mathrm{U}(1)_Y \xrightarrow[SSB]{} \mathrm{U}(1)_{\mathrm{Q}}. \tag{2.2}$$

The Higgs boson does not couple to electric charge Q, a quantum number that is a linear combination of one generator of the weak interaction T_3 and hypercharge Y:

$$Q = T_3 + Y. \tag{2.3}$$

The Higgs mechanism generates mass terms for three linear combinations of the W_i and B bosons, which correspond to the physical, massive $W^{\pm}$ and Z^0 bosons. The fourth and final linear combination corresponds to the remaining (i.e. unbroken) symmetry of $\mathrm{U}(1)_{\mathrm{Q}}$. This boson remains massless and is identified as the photon γ.

Two classes of particles exist: fermions and (gauge) bosons. In the SM, fermions are spin-1/2 particles, while bosons are either spin-0 or spin-1. For each fermion, there exists an antipartner [51], for example the electron's antiparticle counterpart is the positron. Antiparticles have the same physical mass as their particle counterpart, though the quantized charges, such as electric charge, are the opposite [50].

Particles in the SM are characterized by their electroweak and strong quantum numbers. Due to the parity [2] violation in weak interactions [52], different weak quantum numbers are assigned to the left- and right-handed components of these particles. This results in left- and right-handed projections of quarks belong to different multiplets of the electroweak gauge group, namely left-handed projections Q_L are grouped in the fundamental representation of $\mathrm{SU}(2)_L$, i.e. a doublet, while right-handed projections Q_R are singlets:

$$Q_L = \begin{pmatrix} u_L \\ d_L \end{pmatrix}, \begin{pmatrix} c_L \\ s_L \end{pmatrix}, \begin{pmatrix} t_L \\ b_L \end{pmatrix}, \qquad Q_R = u_R, d_R, c_R, s_R, t_R, b_R.$$

The subscripts L, R refer to the left- and right-handed projections of the fermion

[2]The parity operator reverses the sign of all spatial components of a vector: $\mathcal{P}[(x, y, z)] \rightarrow (-x, -y, -z)$.

fields:

$$\Psi_L = \frac{1}{2}(1-\gamma_5)\Psi, \tag{2.4}$$

$$\Psi_R = \frac{1}{2}(1+\gamma_5)\Psi. \tag{2.5}$$

Leptons (fermions that do not interact strongly) can be grouped similarly:

$$l_L = \begin{pmatrix} \nu_{e,L} \\ e_L \end{pmatrix}, \begin{pmatrix} \nu_{\mu,L} \\ \mu_L \end{pmatrix}, \begin{pmatrix} \nu_{\tau,L} \\ \tau_L \end{pmatrix}, \qquad l_R = e_R, \mu_R, \tau_R.$$

Only left-handed neutrinos ν_e, ν_μ, ν_τ have been observed [53], and consequently the right-handed neutrinos are removed from the theory. Neutrinos are also considered to be massless in the SM. While both electroweak and Higgs physics are incredibly rich theories and research avenues, this thesis is concerned with the intricacies of the strong force.

2.1 Quantum Chromodynamics

Quantum Chromodynamics (QCD) is a quantum field theory that describes the interactions between quarks and gluons, and in doing so composite particles such as protons and neutrons. Particles that are composed of quarks are collectively referred to as hadrons, and fall into two major subclasses: mesons, which are bound quark-antiquark pairs, and baryons, which are bound triplets of (anti-)quarks. More exotic bound states, such as tetraquarks, pentaquarks [54] or glueballs, are allowed in the current framework of QCD. There have been several potential tetraquark candidates proposed [55–57], and similarly for pentaquarks [58].

In QCD, there are 6 quark species, known as flavours, that can be categorized into 3 families of pairs: up and down, charm and strange, and top and bottom, as shown in Tab. 2.1. Quarks carry fractional electric charge, meaning they couple to photons like electrons and they are spin-1/2 particles, i.e. fermions. They also carry an additional quantum number for the strong force, known as colour.

QCD is a non-abelian gauge theory, with a gauge group of SU(3) [1], with quarks belong to the fundamental representation, meaning that they carry one of three

Flavour	Charge (e)	Mass
up (u)	$\frac{2}{3}$	2.2 MeV
down (d)	$-\frac{1}{3}$	4.7 MeV
charm (c)	$\frac{2}{3}$	1.3 GeV
strange (s)	$-\frac{1}{3}$	93 MeV
top (t)	$\frac{2}{3}$	173 GeV
bottom (b)	$-\frac{1}{3}$	4.2 GeV

Table 2.1: Table of quark properties, where the 3 families of quark flavours are pairs of rows. Charge is given in units of electron charge. Masses quoted for the three lightest quarks $u, d,$ and s are the so-called current masses, evaluated in a mass-independent subtraction scheme such as $\overline{\text{MS}}$ scheme [59], at a scale of $\sim$ 2 GeV. The c and b quarks are the running masses in the $\overline{\text{MS}}$ scheme. The t quark's mass is taken from direct measurement. Taken from the Particle Data Group review [60].

colours at any given moment, commonly referred to as red, green, and blue. Similarly, there are three anti-colours, which antiquarks carry, since they belong to the conjugate representation. Gluons belong to the adjoint representation and consequently carry one of the eight linearly independent colour states - the colour octet - meaning that they are allowed to undergo self-interactions.

The QCD Lagrangian [46] is given by:

$$\mathcal{L}_{\text{QCD}} = \sum_f \bar{q}_i^f \left(i\gamma^\mu D_\mu - m_f\right)_{ij} q_j^f - \frac{1}{4} G^a_{\mu\nu} G^{a\mu\nu}, \tag{2.6}$$

where the sum is over the flavours f of quark fields q^f, which have mass $(m_f)_{ij} = m_f \delta_{ij}$. The index $i = 1, 2, 3$ counts the three colour-states of the quark. The field strength tensor $G^a_{\mu\nu}$ is given by:

$$G^a_{\mu\nu} = \partial_\mu A^a_\nu - \partial_\nu A^a_\mu - g_s f^{abc} A^b_\mu A^c_\nu, \tag{2.7}$$

where A^a_μ is the gluon field, with gauge coupling g_s, and structure constants f^{abc} of SU(3). The index $a = 1, ..., 8$ counts the eight independent colour-states of the gluon.

If a field ψ transforms under a local gauge transformation [1] as:

$$\psi(x) \to \psi'(x) = e^{i\alpha(x)}\psi(x), \tag{2.8}$$

$$\bar{\psi}(x) \to \bar{\psi}'(x) = e^{-i\alpha(x)}\bar{\psi}(x), \tag{2.9}$$

then taking the usual partial spacetime derivative yields:

$$\partial_\mu \psi'(x) = e^{i\alpha(x)}\partial_\mu \psi(x) + i\left(\partial_\mu \alpha(x)\right)e^{i\alpha(x)}\psi(x). \tag{2.10}$$

The naïve kinetic term of $\bar{\psi}\partial_\mu\psi$ in the Dirac equation would not be invariant under the local gauge transformations in Eq. 2.9, since:

$$\bar{\psi}\partial_\mu\psi \to \bar{\psi}\partial_\mu\psi + i\left(\partial_\mu\alpha\right)\bar{\psi}\psi. \tag{2.11}$$

where the dependence on spacetime coordinates x has been suppressed. In order for the kinetic term to preserve gauge symmetry, the QCD covariant derivative D_μ in Eq. 2.6 is then given by:

$$\left(D_\mu\right)_{ij} = \delta_{ij}\partial_\mu + ig_s T^a_{ij} A^a_\mu, \tag{2.12}$$

where T^a_{ij} are the generators of the SU(3) Lie group. The covariant derivative contains the usual spacetime derivative ∂_μ, but the second term ensures gauge invariance, namely that:

$$\bar{\psi}' D_\mu \psi' = \bar{\psi} D_\mu \psi, \tag{2.13}$$

where we have suppressed the colour indices of the fields and the covariant derivative.

In Fig. 2.1, we illustrate the QCD Lagrangian pictorially. The first set of terms correspond to the quark propagator and the quark-gluon interaction vertex, which along with the gluon propagator on the second line, are analogous to QED[3]. The last two terms in Fig. 2.1 have no analogy in QED as the photon cannot self-interact since it carries no electric charge.

While the QCD Lagrangian in Eq. 2.6 is remarkably simple, there are several caveats. Firstly, the first term in Eq. 2.6 contains the quark mass terms $m_f\bar{q}^f q^f$,

[3] One would need to replace the gluon propagators (curly) with photon propagators.

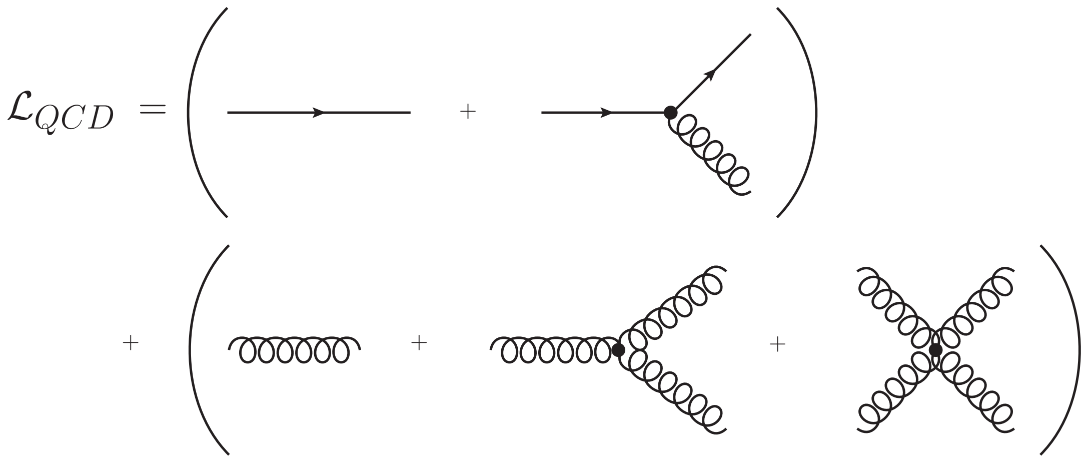

Figure 2.1: Diagrammatic QCD Lagrangian, adapted from [61]. Quark lines are solid, while gluon lines are curly. The last two terms - the three-gluon and four-gluon vertices - occur due to the fact that the gluon carries colour.

though these terms may only exist in a model where QCD is treated as a separate theory from the Standard Model. In the full Standard Model, these mass terms are not invariant under electroweak symmetry, i.e. quarks (and fermions in general) cannot have such mass terms *a priori* since they break electroweak symmetry. Instead their mass must be generated by another mechanism, which in the Standard Model is the Higgs mechanism [4, 6, 7].

Secondly, in Eq. 2.6, in order to quantize the gluon field in the path integral formalism [62] there need to be some extra terms, namely a gauge fixing term and a ghost field term, see e.g. [47]. The gauge fixing term introduced by Faddeev and Popov [63] is given by:

$$\mathcal{L}_{\mathrm{FP}} = -\frac{1}{2\xi}\left(\partial^{\mu} G^{a}_{\mu}\right)^{2}. \tag{2.14}$$

The ghost field, η, terms for the gluon field is given by:

$$\mathcal{L}_{\mathrm{ghost}} = \partial_{\mu}\bar{\eta}^{a}\partial^{\mu}\eta^{a} + g_{s} f^{abc}\partial_{\mu}\eta^{c} G^{b\mu}\eta^{a}, \tag{2.15}$$

and these terms are necessary to remove the unphysical timelike and longitudinal components of the gluon. These modifications mean that the Lagrangian in Eq. 2.6 becomes:

$$\mathcal{L}_{\mathrm{QCD}} \rightarrow \mathcal{L}_{\mathrm{QCD}} + \mathcal{L}_{\mathrm{FP}} + \mathcal{L}_{\mathrm{ghost}}. \tag{2.16}$$

Finally, the QCD Lagrangian can include a CP-violating term, where C is charge and P is parity:

$$\mathcal{L}_\theta \propto \theta G^{a\mu\nu}\tilde{G}^a_{\mu\nu} \tag{2.17}$$

where $\tilde{G^a_{\mu\nu}} = \frac{1}{2}\epsilon_{\mu\nu\rho\sigma}G^{a\rho\sigma}$ is known as the dual field and $\epsilon_{\mu\nu\rho\sigma}$ is the antisymmetric Levi-Civita symbol, and coupling constant θ. Experimental constraints have set an upper bound on the coupling $\theta \ll 10^{-9}$ [64, 65]. While CP-violation occurs in the electroweak sector, there is currently no evidence for this violation in the strong sector, an open question that is known as the strong CP problem [4].

2.2 The Strong Coupling α_s

Perturbative calculations using the Lagrangian in Eq. 2.16 still yield divergent results in the ultraviolet limit, i.e. infinities when integrating over loop-momenta [5] in gluon and quark self-energy processes. The remedy for this is to introduce the notion of renormalization [67], where the couplings and masses entering into the Lagrangian are actually 'bare' couplings and masses. Introducing identical copies of the terms with a multiplicative factor allows one to absorb the individual logarithmic divergences into these factors, and producing well-defined, finite answers[6]. The result of these changes mean that the couplings and masses now depend on the energy scale involved in the interaction in question. This dependence is referred to as the 'running' of the coupling.

The coupling strength $\alpha_s(q^2) = g_s^2(q^2)/4\pi$ between quarks and gluons varies drastically as a function of energy scale q^2, and its functional dependence is encoded in the so-called beta function:

$$\beta(\alpha_s) = q^2\frac{\partial\alpha_s}{\partial q^2}. \tag{2.18}$$

Using perturbation theory to expand the beta function in terms of the strong coupling leads to (at the lowest order):

$$\beta(\alpha_s) = -\alpha_s^2 b_0, \tag{2.19}$$

[4]For more details, there are many reviews on the strong CP problem, see e.g. [65, 66]
[5]See Sec. 2.3 for more details on loops.
[6]An interested reader can find an in-depth review of renormalization in e.g. [43, 46, 47, 68]

where the coefficient b_0 [69,70] is given by:

$$b_0 = \frac{33 - 2n_f}{12\pi}, \tag{2.20}$$

where n_f is the number of flavours of quarks, which depends on the scale q^2, as only quarks with mass $\lesssim \sqrt{q^2}$ may contribute to b_0. For $n_f \leq 16$[7], which is true of the Standard Model where n_f is at most 6, the beta function has a negative sign, and consequently the coupling α_s decreases with increasing energy scale q^2. Substituting Eq. 2.18 into Eq. 2.19, we obtain:

$$-\alpha_s^2 b_0 = q^2 \frac{\mathrm{d}\alpha_s}{\mathrm{d}q^2} = \frac{\mathrm{d}\alpha_s}{\mathrm{d}\ln q^2}, \tag{2.21}$$

which, upon rearranging, yields:

$$-\frac{\mathrm{d}\alpha_s}{b_0 \alpha_s^2} = \mathrm{d}\ln q^2. \tag{2.22}$$

Integrating between scales q^2 and μ^2 then gives:

$$\frac{1}{\alpha_s(q^2)} - \frac{1}{\alpha_s(\mu^2)} = b_0 \ln\left(\frac{\mu^2}{q^2}\right), \tag{2.23}$$

where μ^2 is an arbitrary reference scale. A typical choice for this reference scale is the mass of the Z^0 boson, and the coupling at this scale has been experimentally measured to be $\alpha_s(m_{Z^0}^2) \sim 0.118$ [60]. The solution to Eq. 2.23 can then be written as:

$$\alpha_s(q^2) = \frac{1}{b_0 \ln\left(q^2/\Lambda_{\mathrm{QCD}}^2\right)}, \tag{2.24}$$

where Λ_{QCD} is an infrared cutoff given by:

$$\Lambda_{\mathrm{QCD}}^2 = \mu^2 \exp\left(-\frac{1}{b_0 \alpha_s(\mu^2)}\right). \tag{2.25}$$

Upon inspecting Eq. (2.24), it becomes clear that the strong coupling can exceed unity, and indeed even diverge as $q^2/\Lambda^2 \to 1$, while, conversely, in the limit of $q^2/\Lambda^2 \to \infty$, the coupling vanishes.

[7]There is also the extra constraint that there are no additional colour-charged fields.

The key result of Eq. 2.24 is that the strong coupling between quarks and gluons decreases as the energy of the interaction increases, meaning the partons become more and more weakly interacting at higher energies, a phenomenon known as asymptotic freedom [69,70]. Consequently, processes at these corresponding energy scales can be calculated via the conventional perturbative techniques available to particle physicists.

On the other hand, as the energy scale of the interaction decreases, the coupling strength grows larger, until one reaches scales close to the hadronization scale of $\mathcal{O}(\Lambda_{\mathrm{QCD}}) \sim 200$ MeV where the coupling diverges and perturbative techniques begin to break down, since they are dependent on expansions in α_s. As α_s grows for decreasing q^2, at some point the perturbative expansion is no longer well-defined, namely the terms one discards are of the same order, if not larger than the last terms entering into the calculation. It is in this regime that colour confinement [71] occurs, the phenomenon by which we cannot directly observe individual coloured partons. Due to the perturbative techniques deteriorating, physicists need other approaches. There are two main avenues for low-energy physics studies: lattice QCD, and phenomenological models in Monte Carlo event generators. The latter will be covered in depth in Chap. 3.

Lattice QCD [71–73] discretizes spacetime into a hypercube, and quarks are defined on the lattice sites while gluons are defined on the links connecting sites. The discretization process is implemented by a lattice spacing a which introduces a natural ultraviolet cutoff of $1/a$, regulating the high-energy behaviour of the theory. To recover continuum QCD, the lattice spacing can be taken to $a \to 0$. This is the typical procedure taken by lattice studies in order to extrapolate their discretized results to make predictions about continuum QCD. In discretizing spacetime, time is Wick-rotated [8] and as such becomes Euclidean. The result of this is that the results that lattice QCD yield are steady-state solutions, and the configurations these studies investigate cannot include time evolution. While lattice QCD is an active and fascinating field of research, it is outside of the scope of this thesis.

[8] For more details, see e.g. [47].

2.3 Cross Sections and the Factorization Theorem

At particle colliders, the detectors count the number of occurrences of given events, which is directly related to the likelihood of the associated scattering process occurring - known as the cross section. Calculating cross sections is thus an important task from the theoretical side, and the factorization theorem [74–79] allows physicists to factorize the cross section into two parts: the high-energy (short-distance) scale physics, and the low-energy (long-distance) scale physics. The inclusive[9] cross section for two colliding protons A, B to produce final n-particle state can be factorized as:

$$\sigma(AB \to n) = \sum_{a,b} \int \mathrm{d}x_a \mathrm{d}x_b f_{a/A}\left(x_a, \mu_F^2\right) f_{b/B}\left(x_b, \mu_F^2\right) \times \hat{\sigma}_{ab\to n}(\mu_F^2, \mu_R^2), \quad (2.26)$$

where the so-called parton distribution functions (PDFs) $f_{a/A}, f_{b/B}$ are experimentally extracted quantities, and encode the distributions of a given parton species a, b in the respective protons as a function of the respective momentum fraction x_a, x_b they carry. The momentum fractions $x_{a,b}$ of partons a, b are a fraction of the incoming protons' momentum: $p_{a,b} = x_{a,b} p_{A,B}$. The PDFs also depend on the factorization scale μ_F^2, an unphysical, but computationally useful, energy scale at which the high-energy and low-energy physics are factorized. Since the PDFs probe hadronic properties, the infrared singularities that arise in this realm are absorbed into the PDFs through their dependence on the factorization scale. This introduction of a scale dependence parameters is similar to the effect of using of renormalization to remove ultraviolet divergences. The partonic-level cross section $\hat{\sigma}_{ab\to n}$ is calculable from perturbation theory, and it depends on the factorization scale μ_F^2 and the renormalization scale μ_R^2.

It should be noted that while the factorization theorem has been proven to all orders in the context of electron-positron and deep inelastic scattering collisions, it has yet to be rigorously proven for proton-proton collisions beyond so-called leading twist, where the composite nature of protons complicates matters significantly. Recent advances in the field have started building the pieces for rigorously extending the factorization theorem to proton-proton collisions by studying double-parton scattering [80–84]. A Monte Carlo simulation for double-parton scattering based on these

[9]Inclusive here means that one sums over all possible final states.

approaches has recently been implemented [85, 86].

The partonic-level cross section from Eq. 2.26 can be written at leading-order, also known as the Born-level, as:

$$\hat{\sigma}^{(\mathrm{LO})}_{ab\to n} = \int F_{ab}|\mathcal{M}(a+b\to n)|^2 \mathrm{d}\Phi_n, \tag{2.27}$$

where F_{ab} is the flux factor of the incoming partons a, b, given by:

$$F_{ab} = \frac{1}{4\sqrt{(p_a\cdot p_b)^2 - m_a^2 m_b^2}}. \tag{2.28}$$

In Eq. 2.27, $\mathcal{M}(a+b\to n;\mu_F^2,\mu_R^2)$ is the scattering amplitude for the parton-level process $a+b\to n$, and its evaluation depends on the factorization and renormalization scales. The invariant squared matrix element $|\mathcal{M}|^2$ and the flux factor are integrated over the n-particle Lorentz-invariant phase space:

$$\mathrm{d}\Phi_n = (2\pi)^4\delta^{(4)}\left(p_a + p_b - \sum_{i=1}^{n} p_i\right)\prod_{i=1}^{n}\frac{\mathrm{d}^3 p_i}{(2\pi)^3 2E_i}. \tag{2.29}$$

These squared matrix elements are calculated through the application of Feynman rules, see for example [43, 47], which can be derived from the Lagrangian given in Eq. 2.6. The fundamental building blocks of the invariant matrix elements are vertex factors for interaction points, wave functions for external particles, and propagator factors for internal particle lines (i.e. virtual particles that connect interaction points).

In order to perform precision calculations, it is necessary to go beyond the leading-order partonic-level cross-section in Eq. 2.27 and to calculate higher-order terms. These higher-order terms can have l loops and m extra external particles, leading to a general form for a partonic-level cross section of:

$$\hat{\sigma}_{ab\to n} = \sum_{m=0}^{\infty}\int F_{ab}\left|\sum_{l=0}^{\infty}\mathcal{M}^{(l)}(a+b\to n+m)\right|^2 \mathrm{d}\Phi_{n+m}. \tag{2.30}$$

Choosing the number of loops and extra external particles defines the order of the perturbative expansion, for example next-to-leading-order (NLO) corrections have

$l + m = 1$, so the full NLO partonic-level cross-section can be written as:

$$\hat{\sigma}^{(\mathrm{NLO})}_{ab\to n} = \hat{\sigma}^{(m=0,l=0)}_{ab\to n} + \hat{\sigma}^{(m=1,l=0)}_{ab\to n} + \hat{\sigma}^{(m=0,l=1)}_{ab\to n}, \tag{2.31}$$

namely, as the sum is of the leading-order cross section, the real (i.e. additional external particle) correction, and the virtual (i.e. additional loop) correction respectively. Successively higher-order cross sections will involve more loops and/or more external legs such that the sum $l + m \leq n$ for a given order.

In the NLO partonic-level cross section of Eq. 2.31, there will arise two sets of singularities, i.e. infinities: first, when integrating over the Lorentz-invariant phase space for the real correction term, and second, when integrating over the loop-momenta in the virtual correction term. The KLN theorem [87–90] ensures that these singularities will cancel order-by-order, if one keeps both real and virtual corrections.

2.4 Monte Carlo Event Generators

While particle physicists have crafted an elegant and successful framework with QCD, we need ways to compare the theory to the data that experiments observe and collect. Monte Carlo event generators [13, 60], such as Pythia [14, 91], Herwig [15, 92, 93], and Sherpa [16, 94], are computer programs that aim to simulate all the physical processes involved in high-energy collisions. The above Monte Carlo event generators are general-purpose, being able to simulate a large number of different types of scattering processes such as electron-positron, electron-proton, or proton-proton, but this thesis will focus on the latter.

Monte Carlo event generators separate physical processes in terms of a hierarchy of energy scales, starting with the primary hard process using the factorization theorem, calculated with a fixed-order expansion in perturbation theory. This process determines the highest energy scale in a given event. The partons produced from and incoming to the hard process are fed into the parton shower algorithm, evolving the partons down in energy scale by bremsstrahlung. Once the energy scales are close to the hadronization scale, the parton shower ends, and hadronization takes over, converting the partons via a phenomenological model into colourless hadrons. These hadrons undergo further particle decay and act as input to detector simulations.

2.4.1 Hard Process

The hard process is the most energetic part of a given collision, and in the case of QCD and proton-proton scattering, involves fundamental partonic interactions. These interactions are calculated by perturbation theory, truncating the calculation at some order, then convolved with parton distribution functions as in Eq. 2.26. Event generators such as Pythia and Herwig come included with several $2 \to 2$ and $2 \to 3$ (leading-order) processes automatically. As the technology of computers and matrix element calculations improves, more event generators have surfaced, solely specializing in performing higher-order calculations, ready to be used in more general-purpose event generators. In order to carefully combine the parton shower radiation with these higher-order terms, one needs a prescription to avoid thorny issues such as over- or under-counting regions of phase space. Two such prescriptions are matching, and merging. Examples of matching procedures include MC@NLO [95], and POWHEG [96], while merging procedures include CKKW(-L) [25, 97], and MENLOPS [98]. More detailed reviews of matching and merging can be found in [13, 99].

Examples of matrix element generators include Comix [100], and MadGraph5_aMC@NLO[10] [102]. There are also generators dedicated to specific processes such as vector-boson interactions: VBFNLO [103, 104], and MCFM [105–107]. Herwig has its own dedicated interface for handling the hard process as well as performing matching, called MATCHBOX [108].

2.4.2 Parton Shower

Partons produced from the hard process are evolved from the corresponding energy scale down to the shower cutoff scale, chosen to be close to the hadronization scale. During this evolution, the partons emit *bremsstrahlung* - braking radiation. Incoming partons may also emit bremsstrahlung, known as initial-state radiation, typically implemented via backwards-evolution [109, 110]. Partons produced during the parton shower also undergo the subsequent showering process until they reach the cutoff scale.

[10] A modern unification of the matrix element generator MadGraph5 [101] with the matching formalism of MC@NLO.

The physical roots for a parton shower lie in the fact that the cross section is enhanced in certain regions of phase space. In particular, if a QCD parton is present as an external leg, the matrix element gets enhanced for the case of: the splitting/emission of two partons very close in angle - the collinear singularity, and the emission of a low-energy gluon - the soft singularity. In gauge theories, such as QCD, amplitudes and phase space factorize in these soft and collinear limits of the theory [20, 22, 111]. As a result, the cross section σ_{n+1} for a given number of particles n with one additional emission can be factorized into the n particle cross section σ_n and a universal splitting function that creates the extra emission. Using this notion of a splitting function, one can construct the parton shower, with each parton probabilistically evolved down in energy scale, starting from the hard process momentum-transfer scale, down to a shower cutoff scale.

In Monte Carlo event generators, there are two major paradigms of parton showers: either a DGLAP-based [18–20] parton shower [112–116], where a single parton splits or emits as a $1 \to 2$ process, or a dipole/antenna shower [21, 117–129], where a pair of partons radiate as a $2 \to 3$ process. The DGLAP formalism starts from the factorization of the matrix element in the collinear limit, for final-state parton $a \to bc$:

$$|\mathcal{M}_{n+1}|^2 \xrightarrow[\text{collinear}]{} 8\pi\alpha_s \frac{P_{a\to bc}}{q^2}|\mathcal{M}_n|^2, \tag{2.32}$$

where $P_{a\to bc}$ are known as the DGLAP splitting functions or kernels [18–20]. These splitting functions also contain colour factors that are process dependent - $C_A = N_C = 3, C_F = 4/3$, and $T_R = 1/2$. At leading-order, the allowed DGLAP splitting processes are gluon emissions: $q \to qg$ or $g \to gg$, and gluon splitting: $g \to q\bar{q}$, depicted in Fig. 2.2. Due to energy and momentum conservation, a $1 \to 2$ splitting process cannot occur with all partons being on-shell. Thus parton showers using the DGLAP formalism need to have a recoil strategy or kinematics map to reshuffle momentum. This can either occur at each individual branching step by designating a single recoiling parton or a system of recoiling partons, or at the end of the entire shower process.

The dipole/antenna formalism begins from the factorization of the matrix element in the soft limit, for final-state partons emitting in the following process

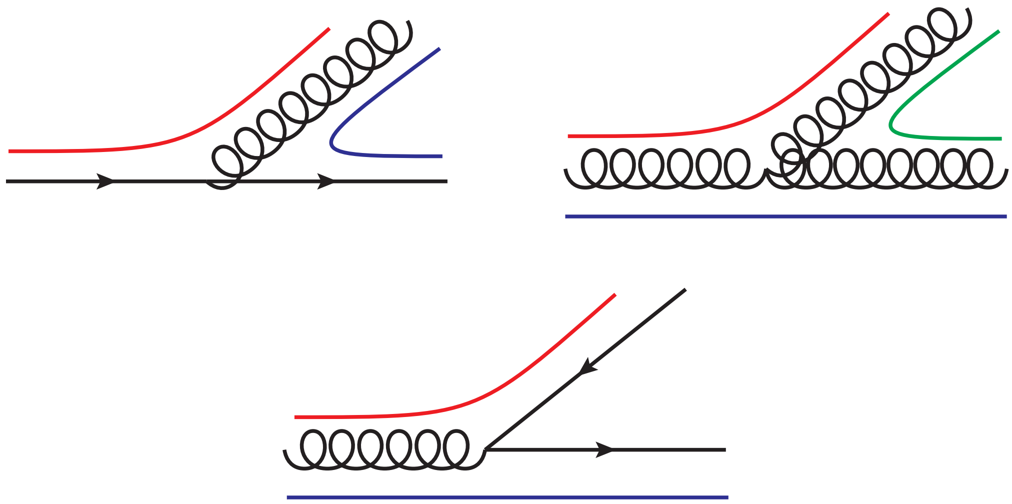

Figure 2.2: The different branchings in a DGLAP-based QCD parton shower: *(top left)* $q \to qg$, *(top right)* $g \to gg$, and *(bottom centre)* $g \to q\bar{q}$, along with the colour flow produced using the leading-colour approximation. There is one more branching: $q \to gq$, though it is directly related to the left branching.

$IK \to ijk$:

$$|\mathcal{M}_{n+1}|^2 \xrightarrow[\text{soft}]{} 4\pi\alpha_s \mathcal{C}\mathcal{S}_{ijk}|\mathcal{M}_n|^2, \tag{2.33}$$

where $\mathcal{C}$ is the process-dependent colour factor, and $\mathcal{S}_{ijk}$ is the universal soft (eikonal) factor, given by (for massless partons):

$$\mathcal{S}_{ijk} = \frac{2s_{ik}}{s_{ij}s_{jk}}, \quad \text{where} \quad s_{ij} = 2p_i \cdot p_j. \tag{2.34}$$

The allowed dipole/antenna processes depend on the pair of radiating partons. The recoiler is specified by the factorization process that produces the dipole/antenna splitting function. For dipole showers, one parton in the pair is designated the emitter, while the other is a recoiler, while antenna showers are agnostic to which parton is the emitter or recoiler as both participate in the process and as such both will recoil.

While QCD in its full form is an SU(3) gauge group, Monte Carlo event generators typically use the leading-colour approximation [130, 131]. This approximation generalizes the QCD gauge group to one with an arbitrary number of colours N_c to give a gauge group of SU(N_c). This produces terms which will depend on N_c, and subleading terms of $\mathcal{O}(1/N_c^2)$. The leading-colour approximation finally takes the limit of $N_c \to \infty$, removing any terms that are subleading in colour[11]. As a result of

[11]It should be noted that although the leading-colour approximation drops terms subleading in

this approximation, only planar Feynman diagrams [130, 131], i.e. diagrams where the colour flow between partons can be drawn exclusively in the plane, enter into the event generation, and no two quarks in an event may share the same colour. In the leading-colour approximation, gluons carry a colour and an anti-colour. A key consequence of taking the leading-colour approximation is that there is no quantum interference in the splitting process, since these terms are subleading.

For the single parton branching used in DGLAP showers, this results in the colour flow shown in Fig. 2.2. For the dipole shower, this means that only colour-connected dipoles radiate, since there are no 'repeated' colours, reducing the number of dipoles to consider during the parton shower, as there is no dipole-dipole interference. In comparison, in QED showers, one must consider all possible dipoles for radiation [132], since there is no such leading-colour approximation, and instead terms can only become suppressed from the lack of available phase space. While the DGLAP-based parton shower does not have coherence between partons, it can be imposed via certain constraints on the showering process [133], such as angular ordering [134], whereby subsequent emissions have a smaller emission angle than the emission before. The two pictures of showering, DGLAP-based and dipole/antenna based, are dual frameworks to each other, with the former capturing the full collinear and the partial soft structure of QCD emissions, while the latter captures the full soft and partial collinear structure.

While three is very different from infinity, the leading-colour approximation works remarkably well in electron-positron collisions, a relatively clean environment since only the outgoing products of the collision may carry colour. One strength of the leading-colour approximation is that colour-suppressed contributions are also kinematically suppressed. In the more busy and complicated environment of proton-proton collisions, this approximation is still used, though the accuracy of the approximation is somewhat diminished. However, recent research has delved into introducing parton showers without this approximation, instead choosing to improve the shower with QCD colour structures or to use a full-colour parton shower [108, 135–142].

Working in the DGLAP framework, the differential probability for a final-state

colour, numerical values are still obtained with $N_c = 3$, e.g. in the β function in Eq. 2.19, and in the colour factors C_A and C_F in amplitudes.

parton a to undergo a branching is given by:

$$\frac{\mathrm{d}\mathcal{P}_{a,\mathrm{branch}}}{\mathrm{d}q^2} = \frac{\alpha_s}{2\pi}\frac{1}{q^2}\int_{z_{\min}}^{z_{\max}} \mathrm{d}z \sum_{b,c} P_{a\to bc}(z), \tag{2.35}$$

where q^2 is an energy or resolution scale, z is the energy fraction of parton b with respect to a i.e. $E_b = zE_a$, with c taking the rest, i.e. $E_c = (1-z)E_a$, and z is bounded between $[z_{\min}, z_{\max}]$, and $P_{a\to bc}$ are the DGLAP splitting functions [18–20] depicted in Fig. 2.2. The parton shower evolves partons from a scale Q_0^2 down to a lower energy scale Q_1^2 by generating emissions. In order to do so, we need to define the probability that there are no emissions between these two scales. If $\delta q^2 = Q_0^2 - Q_1^2$, then the naïve application of Eq. (2.35) would yield a branching probability of:

$$\frac{\delta q^2}{q^2}\frac{\alpha_s}{2\pi}\int_{z_{\min}}^{z_{\max}} \mathrm{d}z \sum_{b,c} P_{a\to bc}(z). \tag{2.36}$$

The naïve probability of no branching is then:

$$1 - \frac{\delta q^2}{q^2}\frac{\alpha_s}{2\pi}\int_{z_{\min}}^{z_{\max}} \mathrm{d}z \sum_{b,c} P_{a\to bc}(z). \tag{2.37}$$

Subdividing δq^2 into n steps would then yield a probability for no emissions that is n multiplicative copies of Eq. 2.37, since each interval must have no emissions. Taking the infinitesimal limit of $n \to \infty$ yields the Sudakov form factor, i.e. the no-emission probability for parton a between two scales $Q_0^2 > Q_1^2$:

$$\Delta_a(Q_0^2, Q_1^2) = \exp\left(-\int_{Q_1^2}^{Q_0^2} \frac{\mathrm{d}q^2}{q^2}\frac{\alpha_s}{2\pi}\int_{z_{\min}}^{z_{\max}} \mathrm{d}z \sum_{b,c} P_{a\to bc}(z)\right). \tag{2.38}$$

The Sudakov form factor can be similarly defined in the dipole/antenna framework, and forms the backbone of the parton shower algorithm.

Parton shower research is an extremely active area of research, and includes building a parton shower from quantum mechanical amplitudes, rather than the conventional matrix elements [143, 144], implementing next-to-leading order parton showers [145–148], developing showers that use helicity-dependent matrix element corrections or splitting functions [149,150], as well as including spin correlations [151–157].

2.4.3 Multiple Parton Interactions

As protons are composite objects, when two collide there may be more than one subcollision between the partonic constituents of these protons. These subcollisions between partons are called Multiple Parton Interactions (MPI) and these processes form a vital part of proton-proton collision event generation.

MPI were first introduced to Monte Carlo event generators in [17], where the pairwise interactions between partons were produced in an approximately independent fashion, i.e. with Poissonian statistics as an initial ansatz, and extended from the perturbative regime of high-$p_\perp$ down to the low-$p_\perp$ region. The model also introduced the notion of an impact parameter dependence on the number of MPI in an event. Protons are extended objects, with a finite size, and when they collide at extremely high energies, they are Lorentz-contracted into two colliding discs or pancakes. Accordingly, these discs may overlap more or less, depending on the distance between the centres of the discs, known as the impact parameter.

When MPI are produced, the colour structure connecting them to each other and to the beam remnant is unclear. There are no first-principles guidelines, and indeed colour reconnection was first introduced in [17] to change the initially produced colour structure for MPI. We will discuss colour reconnection more in Sec. 3.4.

Most early implementations of MPI did not include parton showers for the additional partonic interactions, with only the hard process undergoing initial-state and final-state radiation. However, Pythia, Herwig, and Sherpa have since introduced showers for the partons entering into or produced from additional MPI [158]. In Herwig and Sherpa, the MPI modelling is separated from the parton shower, while in Pythia, the two processes are interleaved [115], so that new MPI and additional initial-state radiation act as competitors for the energy available in a given collision.

Since the introduction of MPI, a proliferation of research in the area has continued. Herwig uses an MPI model based on the eikonal factorization [159–162]. Herwig has also recently studied and improved the MPI model on several fronts [163,164]. We will discuss the MPI model used in Herwig in more depth in Chap. 5.

2.4.4 Hadronization

One of the most distinctive features of QCD is confinement. Since confinement dictates that we cannot measure or detect quarks and gluons directly, we need a phenomenological model that converts the individual partons that carry colour into colourless composite hadrons, some of which will be detected by experiments and some of which will undergo further decay. This conversion process is known as hadronization. There are two major paradigms of hadronization in high-energy event generators: the Lund string model [26, 165] implemented in Pythia, and the cluster model [28, 166], implemented in Herwig and Sherpa. We will present the main features of the two models in Chap. 3, as well as other hadronization-related phenomenology.

2.4.5 Decays

There are two major stages of decays in a Monte Carlo event generator: perturbative resonance decays, and hadronic decays. For resonance decays, such as the decay of the electroweak bosons $W^{\pm}$ and Z^0, the Higgs boson, or the top quark, if the products of the decay have energy scales above the hadronization scale, they will be evolved down via the parton shower. Recent work has begun to phrase top quark resonance decays in the language of antenna showers [167]. Note that the top quark decay process is considered in most event generators to be perturbative since its decay width is larger than the hadronization scale. Consequently, the top quark is the only quark that is not involved in hadronization modelling.

A vital part of modelling the low-energy regime of an event is accurate simulation of hadronic decays. During the hadronization phase, Lund strings and clusters can break up through a number of steps, finally creating on-shell excited hadrons, called primary hadrons. These primary hadrons are typically unstable, and event generators have to handle the decay processes of these unstable hadrons, using decay tables with experimentally extracted branching ratios. These decay tables have to be supplemented with additional free parameters to model any branching ratios that are unmeasured, and to ensure that the sum of all branching ratios is unity. Another approach for modelling particle decays is to use quantum mechanical decay amplitudes, for example by using simple phase space models like those in Pythia/Jetset [168], or more sophisticated frameworks, with QQ [12], and EvtGen [29] for hadron decays, and TAUOLA [169–171] for tau decays.

2.4.6 Detector Simulations

General-purpose Monte Carlo event generators do not have detector simulation, i.e. they do not simulate the minute and intricate processes involved in produced particles colliding with the surfaces of the detector, nor the geometry of the detector itself. When experimentalists wish to model the whole event down to the detector level, they use the output from event generators as input into dedicated simulation software, such as Geant4 [172, 173], which simulates the propagation of particles through matter.

[12] QQ - The CLEO Event Generator, see http://www.lns.cornell.edu/public/CLEO/soft/QQ

3

Hadronization and Colour Reconnection

Hadronization is the phenomenological model that describes individually coloured partons from the end of the parton shower process and their subsequent transition into colourless hadrons. This chapter aims to give an overview of some of the models of hadronization used in high-energy event generators, their respective sets of colour reconnection models, and the signs of collectivity in proton-proton collisions. An excellent and in-depth review of hadronization as it applies to Z^0 decays can be found in [174].

3.1 Independent Fragmentation

Independent fragmentation [175] is the oldest framework for hadronization, offering arguably the simplest picture: each parton hadronizes independently of any other ones. To achieve this, the model uses an iterative branching[1], akin to the parton shower, of the form $q \to h + q'$ where h is the produced hadron, containing quark content $q\bar{q}'$. The $q'\bar{q}'$ pair are created out of the vacuum, with a Gaussian transverse momentum distribution. A schematic illustration of the iterative branching is shown in Fig. 3.1. One of the most widely known versions of independent fragmentation is the Field-Feynman model [176, 177].

As Fig. 3.1 illustrates, there is a natural 'rank ordering' of the hadrons produced,

[1]The iterated branching is also known as the unit cell.

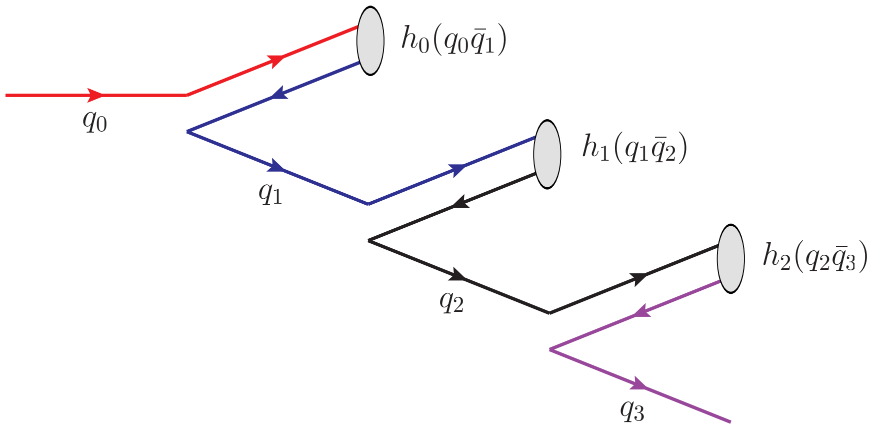

Figure 3.1: Schematic diagram of the iterative branchings of the form $q_i \to h_i + q_j$ used in independent fragmentation. Each hadron h_i produced will take a fraction of the energy and momentum of quark q_i.

with the most energetic being produced first, i.e. hadron h_0 being produced before hadron h_1, and so and so forth, creating an outside-in fragmentation process. It should be noted that this rank ordering cannot be interpreted as time ordering.

3.2 Lund String Model

In the short distance regime, the potential between a quark-antiquark pair is dominated by a Coulombic potential, very much like the potential between an electron and positron, as shown in the top panel of Fig. 3.3. The Lund string model [26, 165, 178–180] takes inspiration from results in lattice QCD[2], see e.g. [182, 183] amongst other phenomenological calculations[3] that indicate that the potential between a quark and an antiquark grows linearly with distance, as shown schematically in Fig. 3.2. The form of the potential $V(r) = \kappa r - \frac{a}{r}$ between two static quarks as a function of their spatial separation, sometimes known as the Cornell potential [186], though strictly speaking the Cornell potential has extra terms that are of the form $1/r^2$ and a constant in order to obey conservation laws. For 'large' distances, i.e. $r \gtrsim 1$ fm, the potential tends to $V = \kappa r$, where $\kappa \sim 1$ GeV/fm is the constant growth rate of the potential - more commonly known as the string tension. There is a Coulombic term

[2] Lattice QCD is an approach to study non-perturbative phenomena in QCD by discretizing space-time. Quarks are fields defined at the lattice sites, while gluons act as the links interconnecting the sites. A thorough review of lattice QCD can be found in [181].

[3] Examples include Regge phenomenology, see e.g. [184], and quarkonium spectroscopy, see e.g. [185].

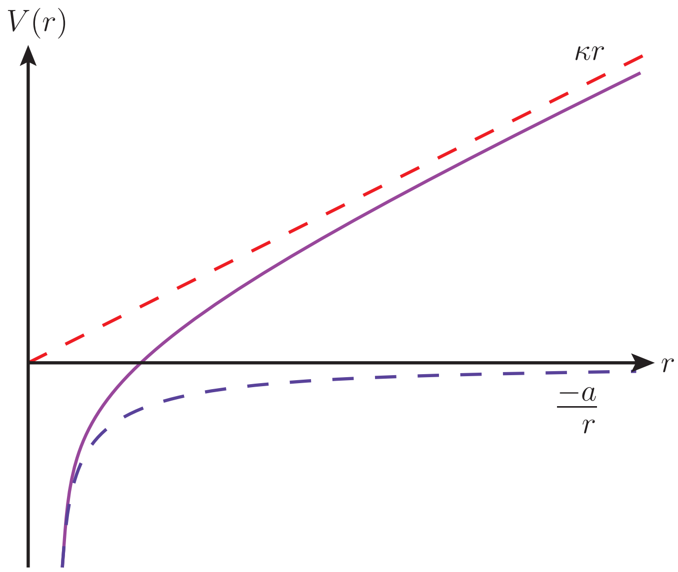

Figure 3.2: Schematic diagram of the Cornell potential between a static quark-antiquark pair [186].

in the potential as well, but this is ignored in the Lund string model. The physical interpretation of the linear potential is that the QCD vacuum tries to expel [4] the field lines between the quark and the antiquark, causing the field lines to be confined to a thin tube of gluonic flux lines, as shown in the bottom panel of Fig. 3.3.

3.2.1 Yo-yo motion

The simplest string possible is thus a massless quark-antiquark pair, propagating away from each other in one spatial direction x and one temporal t. They start with only kinetic energy, but as they travel away from each other, the attractive force between them causes the quarks to lose energy and momentum, and transfer it to the string stretched between them, stored as potential energy. Once the quarks have lost all their kinetic energy, their motion reverses and the string transfers its potential energy back to the quarks. This is known as the yo-yo mode, shown schematically in Fig. 3.4.

The quarks are initially at $(t, x) = (0, 0)$ and travelling with equal and opposite momenta, and there is no potential energy in the string:

$$\begin{aligned} (E, p_x) &= \frac{E_{\text{cm}}}{2}(1, \pm 1), \\ E_{\text{string}} &= 0, \end{aligned} \tag{3.1}$$

[4] This is the colour-superconductivity analogue of the Meissner effect, see e.g. [187]

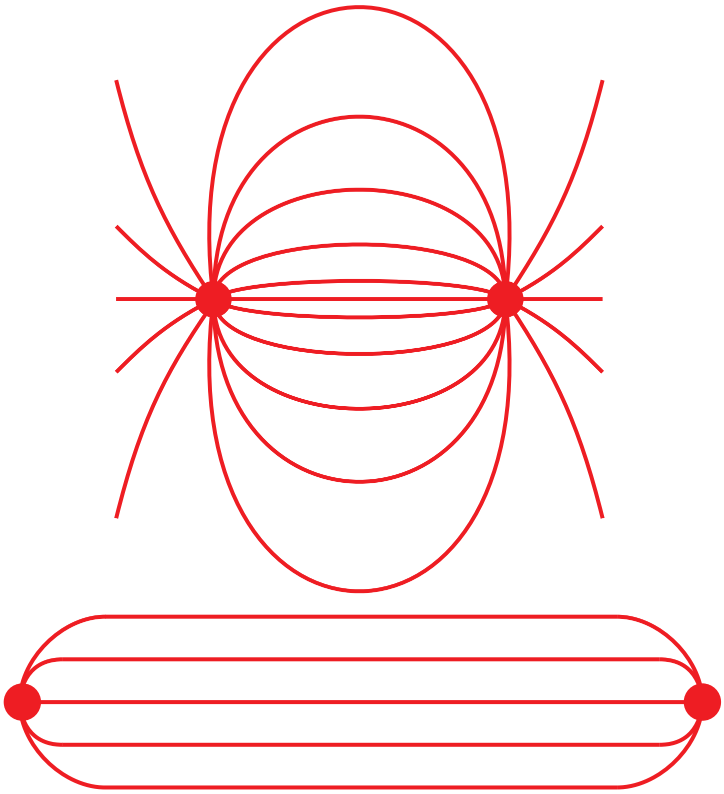

Figure 3.3: Schematic diagram of the field lines of (*top*) the Coulombic potential between static quark-antiquark pairs at short distances, which resembles the potential between positive and negative charges in QED, and (*bottom*) the linear potential between the same static quark-antiquark pair at larger distances, forming a Lund string, a potential without an analogy in QED.

where we set the speed of light $c = 1$. Each endpoint propagates away from the origin, losing kinetic energy until it is stationary. At this point, the string has maximum potential energy and extent:

$$\begin{aligned} (E, p_x) &= (0, 0), \\ E_{\text{string}} &= E_{\text{cm}}. \end{aligned} \tag{3.2}$$

The time taken until this point from the origin, is then simply given by $\kappa t_1 = p_x(0)$, i.e.:

$$t_1 = \frac{E_{\text{cm}}}{2\kappa}, \tag{3.3}$$

which is the quarter period of motion.

Once the quarks have been pulled back to $x = 0$, they are back to the initial configuration, but with their momenta swapped, thus this point in time t_2 is the

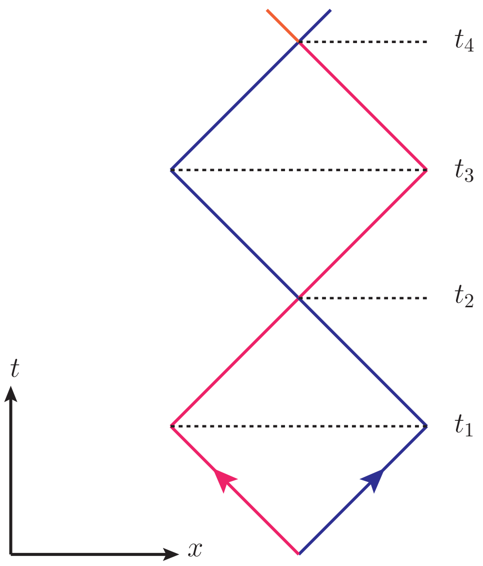

Figure 3.4: Schematic diagram in (1+1)-D of a massless quark-antiquark pair undergoing classical yo-yo motion in the Lund string model. The different coloured trajectories are to track the endpoints as they reach the various times: t_1 is a quarter period and is reached when the quarks are at maximum separation, t_2 is the half period, where the partons are back to the start, but travelling in the opposite direction, t_3 is the third quarter period, and lastly, t_4 is the full period, where the yo-yo has returned to its initial configuration.

half-period of motion: $t_2 = \frac{E_{\rm cm}}{\kappa}$. The two other times in Fig. 3.4 are then:

$$\begin{aligned} t_3 &= \frac{3E_{\rm cm}}{2\kappa}, \\ t_4 &= \frac{2E_{\rm cm}}{\kappa}, \end{aligned} \tag{3.4}$$

at which point, the $q\bar{q}$ pair has completed one full period of motion. The area swept out by the yo-yo mode by t_4 is proportional to the invariant mass of the string:

$$\kappa^2 A = m^2 = E_{\rm cm}^2. \tag{3.5}$$

To see this, let the starting coordinates of the $q\bar{q}$ pair be $(t, x) = (0, 0)$. At t_1, the distance the quark has travelled is given by: $x_{1,q} = t_1 = E_{\rm cm}/2\kappa$, and similarly for the antiquark: $x_{1,\bar{q}} = -t_1$, where we have let the quark propagate in the positive x-direction. The total area swept out is then simply 4 sets of triangles with equal sub-area: $t_1(x_{1,q} - x_{1,\bar{q}})/2$, giving:

$$A = 4 \cdot \frac{t_1(x_{1,q} - x_{1,\bar{q}})}{2} = \frac{E_{\rm cm}^2}{\kappa^2}. \tag{3.6}$$

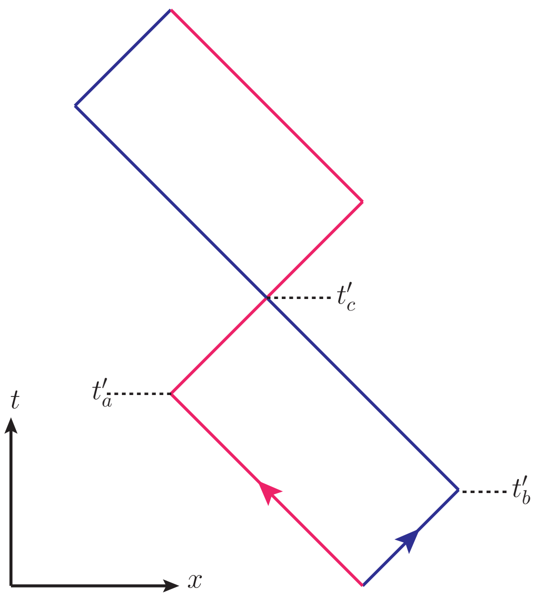

Figure 3.5: Schematic diagram of the yo-yo mode in Fig. 3.4 after a boost in the positive x direction.

It may seem that this string is not Lorentz covariant, since the shape of the yo-yo mode in Fig. 3.4 is clearly not invariant under boosts along the x-axis. If we boost in the positive direction, the square-shaped motion becomes rectangular, as shown in Fig. 3.5. However, while the shape of the yo-yo motion is not invariant, nor the time at which the ends turn around t'_a and t'_b, the area swept out during one full period $2t'_c$ is indeed invariant, since this is proportional to the total invariant mass of the string.

Since the yo-yo motion in Fig. 3.4 is determined for massless quarks propagating along lightcones, one question one might ask is what happens for strings with massive quark endpoints? Since the lightcones represent the massless limit, massive quarks travel along hyperbola, the asymptotes of which are the lightcones. A thorough review of the massless relativistic string as well as extending the Lund string model to massive quarks can be found in [165].

3.2.2 String fragmentation

The yo-yo motion described was inspired by the massless classical relativistic string, but as we have mentioned particle physics is inherently quantum mechanical. As the endpoints of the string propagate, they may transfer enough energy to the string to create quark-antiquark pairs between the original endpoints. In the string model, string fragmentation occurs by $q\bar{q}$ pairs quantum tunnelling in the force field between

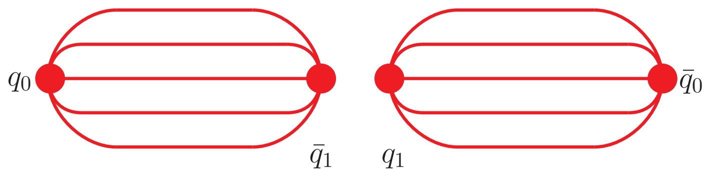

Figure 3.6: Schematic diagram of the tunnelling process in the field lines of a given quark-antiquark pair. The newly produced quark-antiquark pair no longer have field lines stretched between them. Since the $q_1\bar{q}_1$ pair has to tunnel out with some finite $m_\perp$, the pair production reduces the overall string 'length'.

the string endpoints, as demonstrated in Fig. 3.6. The distance the pair has to tunnel is proportional to the transverse mass of the pair per unit string tension: $d = m_{\perp,q}/\kappa = \sqrt{m_q^2 + p_{\perp,q}^2}/\kappa$.

Using the WKB approximation [26, 165] to calculate the probability for tunnelling, one then obtains:

$$P \sim \exp\left(-\frac{\pi m_{\perp,q}^2}{\kappa}\right) = \exp\left(-\frac{\pi m_q^2}{\kappa}\right)\exp\left(-\frac{\pi p_{\perp,q}^2}{\kappa}\right). \tag{3.7}$$

In other words, the transverse momentum distribution for quarks produced via string breaks is independent of the mass, and as a consequence the type, of quark produced. While the $p_\perp$ distribution is universal, there is a Gaussian mass suppression in Eq. 3.7, suggesting that heavier species are suppressed relative to the lighter ones. In particular, only three species of quarks may be produced during the string fragmentation process in Pythia: up, down, and strange, with a relative weight of approximately $1 : 1 : 0.22$, since the top quark does not participate in hadronization, and the charm and bottom quarks are too massive to be pair-produced at any reasonable rate. It should be noted that while the mass suppression is well-motivated from Eq. 3.7, there is no a priori knowledge of which masses to use, e.g. the values in Tab. 2.1, the so-called constituent masses, or some other mass definitions. Instead, the relative production rates are free parameters tuned to data.

Baryons can also be produced in string fragmentation, via two different mechanisms: pair-production of a two-quark system, known as diquarks, at a single vertex, analogous to the ordinary string fragmentation discussed above, and the so-called popcorn mechanism. In an ordinary string break, the produced $q\bar{q}$ pair has to have the right colours to produce a colourless hadron, i.e. given an initial pair $q_0\bar{q}_0$ with

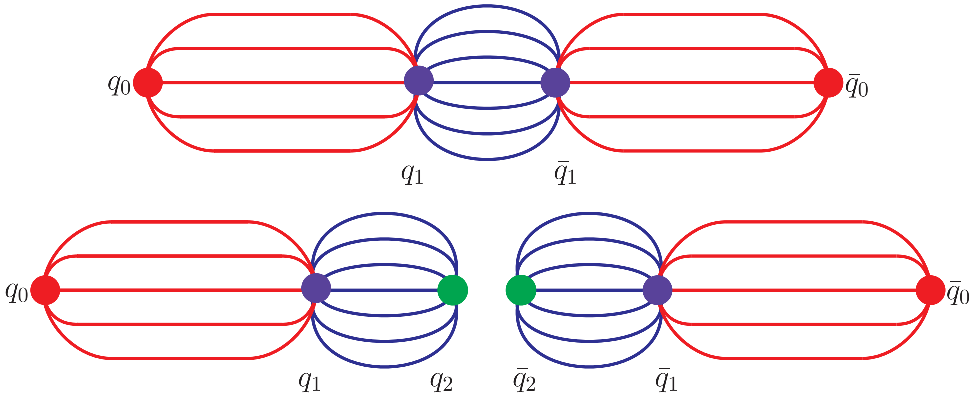

Figure 3.7: Schematic diagram of the popcorn mechanism, in which (*top*) a $q\bar{q}$ pair tunnel out but do not have the correct colour to break the string, until (*bottom*) the third colour pair of quarks are produced, creating a baryon and an antibaryon.

colours red and anti-red, all other subsequent $q\bar{q}$ pairs must also have those colours. In the popcorn mechanism, a $q\bar{q}$ pair may be produced with the 'wrong' colour to break the string, meaning that the produced pair does not break the string. A subsequent pair may break the string, as long as they have the third and final colour to make a colourless baryon. We have included Fig. 3.7 as an example. The popcorn model also allows for mesons to be produced between the baryons, reducing the strong correlations introduced by producing two primary baryons adjacent to each other. We will not discuss this mechanism further, but instead direct the interested reader to [188–190].

The tunnelling mechanism in Eq. 3.7 is a stochastic iterative process whereby a string produces a string (remnant) and a hadron. Sampling the tunnelling probability determines the flavour content of the new hadron to be produced, as well as its $p_\perp$ relative to the string axis, but we need one final piece of the fragmentation puzzle to create a hadron: the longitudinal momentum taken from the string along its axis. This fraction z follows the distribution of the so-called symmetric Lund fragmentation function:

$$f(z) = N\frac{(1-z)^a}{z}\exp\left(\frac{-bm_\perp^2}{z}\right), \tag{3.8}$$

where z is the fraction of the string's available lightcone momentum taken by a created hadron, while the string retains the remainder $1-z$. The parameters a and b are two free parameters in the string model, $m_\perp^2 = m^2 + p_\perp^2$ is the transverse mass of the produced hadron, and N is an overall normalization constant. The form of

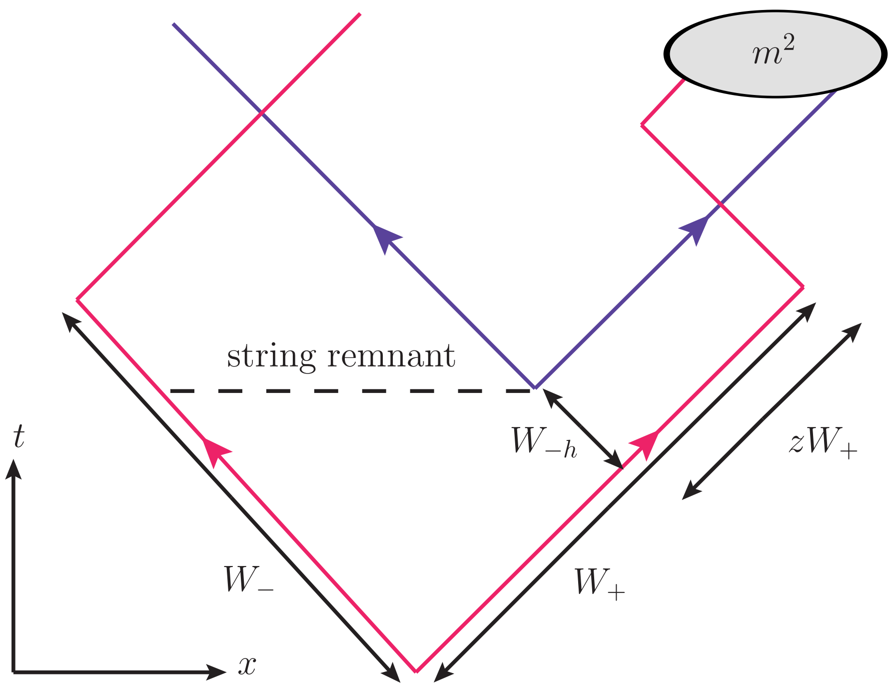

Figure 3.8: Schematic diagram in the (1+1)-D undergoing a single fragmentation, producing a hadron with invariant mass m^2 by taking a fraction z of the positive lightcone momenta W_+ of the right-most string endpoint. In order to put the hadron on-shell, the string must also donate some negative lightcone momenta, denoted W_{-h}, to the hadron.

the fragmentation function is uniquely defined by some very simple constraints such as left-right symmetry, which are presented in App. A. The free parameter a may in general be flavour-dependent, while b is strictly independent of the flavour of the produced pair. Large a suppresses the hard region of $z \to 1$ where a fragmenting hadron takes a large fraction of the lightcone momentum, while large b suppresses the soft region of $z \to 0$. For strings with very massive quark endpoints, namely charm and bottom quarks, there have been several models modifying the fragmentation function, such as the Bowler model [191], and the Peterson/SLAC model [192].

Having selected $m_\perp$ and z for the fragmenting hadron, the string remnant is updated to conserve energy and momentum, i.e. one of the pair-produced quarks will replace the fragmenting endpoint, and will receive $-p_{\perp,q}$ to conserve the transverse momentum along the string. Fig. 3.8 depicts a single string break, with a hadron taking z from the positive lightcone momenta $W_+ = E + p_z$, leaving behind $(1-z)W_+$ for the remnant. In order for the hadron to be put on-shell with transverse mass $m_\perp$,

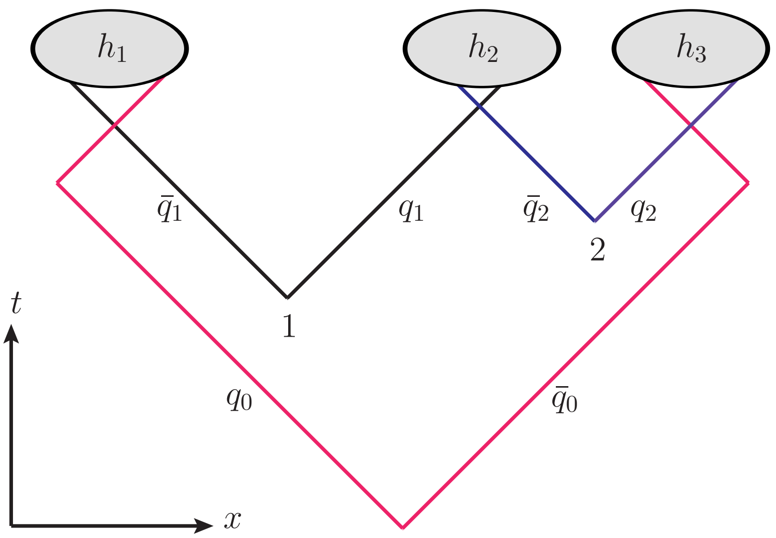

Figure 3.9: Schematic diagram of a string fragmenting in (1 + 1)-D via two breaks (numbered vertices 1 and 2) and creating three primary hadrons h_1, h_2, h_3. The primary hadrons will then undergo particle decay, decaying into more stable particles.

it must also take some of the negative lightcone momenta $W_{-h} = z_- W_-$ given by:

$$z_- = \frac{m_\perp^2}{z W_+ W_-} \tag{3.9}$$

String fragmentation proceeds iteratively from either end of the string, choosing an end at random for each string break, until finally, the string remnant falls below a given cutoff invariant mass W^2_{stop}, implemented as a free parameter of the model. This remnant then undergoes isotropic decay into two hadrons. All the hadrons produced from string breaks are called primary hadrons, and are typically unstable, undergoing further particle decays.

We include an example of multiple string breaks in Fig. 3.9, an initial pair of string endpoints $q_0\bar{q}_0$ propagate away from each other, and there are two subsequent string breaks labelled 1 and 2. After both breaks have occurred, the string has been completely converted into three hadrons: h_1, h_2, and h_3, which have as their quark content $q_0\bar{q}_1$, $q_1\bar{q}_2$, and $q_2\bar{q}_0$, respectively.

Overall, the string fragmentation has a number of similarites with the independent fragmentation scheme. Firstly, there is also a notion of rank ordering, since one can trace out the history of the hadrons produced from the string fragmentation process. Secondly, one can view the whole string fragmentation with a quark-antiquark pair undergoing independent fragmentation, but with an additional constraint of being kinematically entangled, via the so-called left-right symmetry. By having the full string fragment, the joining procedure required in independent fragmentation becomes far simpler, as well as maintaining energy-momentum conservation. The symmetric Lund fragmentation function in Eq. 3.8 can be compared to the analogous fragmentation function in the independent fragmentation scheme:

$$f_{\text{ind.}}(z) \sim (1-z)^{c-1}, \tag{3.10}$$

for a constant c.

The largest difference between the Lund string model and the independent fragmentation model is that the latter is unable to describe what is now called the 'Lund string effect' in three-jet events [193–196]. Three-jets events in electron-positron collisions can be attributed to a hard scattering process of $e^+e^- \to qg\bar{q}$. In the Lund string model, this configuration of partons are all connected by a long colour string, with a $q-g$ string and a $g-\bar{q}$ string, and no string stretched between the quark and antiquark. The particle density observed between the quark and antiquark jets decreased more strongly with increasing transverse mass of the produced particles than the particle density between the gluon-identified jet and either of the two other jets [195]. In the independent fragmentation model, the reduced particle density between the q and $\bar{q}$ jets cannot be described, while in the Lund string model, there is no string in this region, thus the likelihood of particle being produced there is significantly lower. While independent fragmentation is only of historical interest in contemporary hadronization, the iterative cascade process did survive, albeit with some modifications, in the fragmentation process of the Lund string model.

3.2.3 Other string structures

While the yo-yo mode is an instructive guide to the principles behind the Lund string model, there are many more aspects to the model. Parton showers create long colour-chains that connect a quark to an antiquark via a series of gluons, as shown in Fig. 3.10. In the string model, these connecting gluons act as kinks to the structure of the straight string as described above. While these gluons add a number of computational complexities to the mechanics of string motion, the Lund model is extremely

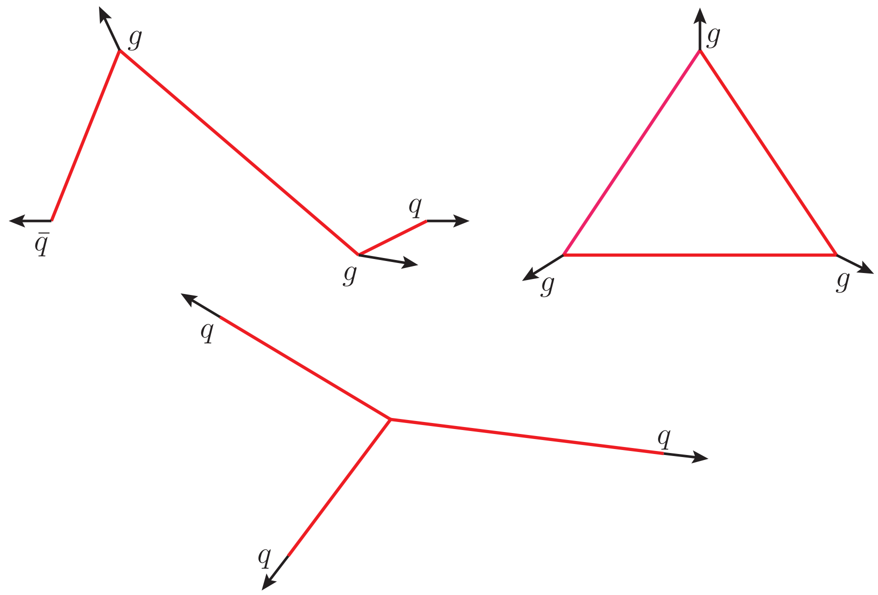

Figure 3.10: Schematic diagram of the more complicated string topologies that can occur in the Lund string model: (*top left*) general strings with gluon kinks, (*top right*) gluon loops, and (*bottom centre*) junctions. Red lines indicate the string segments between the connections, and the black arrows the momentum vectors of the connected partons.

powerful in its momentum-space description of hadronization, since gluon kinks are well-motivated in its framework and add very few new parameters.

Other colour topologies that may occur in the string model are: gluon loops, where there are no quark/antiquark endpoints, and instead two gluons with any number of gluonic connections between them; and junctions, which are used in describing baryons, and connect three (anti-)quarks together in a Y-shaped meeting point. A schematic diagram of these general strings has been included in Fig. 3.10, and one can build more general and complicated string topologies out of these building blocks [197]. While they are extremely interesting to study and a necessary part of modelling hadronization, they are outside the scope of this thesis.

3.2.4 Strings or bags?

One approach to model low-energy QCD has been to use techniques from condensed matter field theory, namely, to describe the QCD vacuum as a dual[5] superconductor [187, 198]. There are two such types of superconductor: type-I and type-II. In type-I superconductors it is energetically favourable for field lines to coalesce and vor-

[5]Dual here meaning the roles of magnetism and electricity have been transposed.

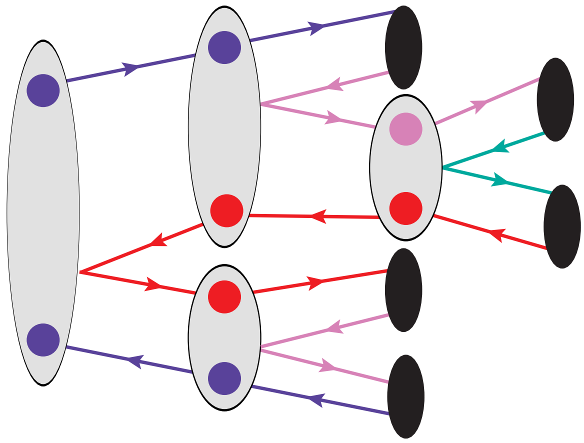

Figure 3.11: Schematic diagram of a (grey) cluster undergoing fission, and the produced clusters undergoing decay (creating two black hadrons), or continuing to fission once more. Coloured lines trace the partonic constituents of the clusters.

tex lines can carry many units of flux, while in type-II superconductors, the vortex lines may only carry a single unit of flux. Translating these types to QCD leads to two different QCD models: the bag model [199, 200], and the string model respectively.

The Lund string model is just one model of string-based hadronization and there are a variety of other approaches [174], such as the UCLA model [201], the Artru-Mennessier string [202, 203], and the CalTech-II model [204], though the Lund string is by far the most widely used one.

While some results in lattice QCD originally supported a strongly type-II QCD vacuum [205, 206], more recent lattice studies suggest that QCD vacuum is somewhere between type-I and type-II [207, 208], suggesting that both models will need to be reconsidered and perhaps married. Work such as rope hadronization [209] has incorporated these nuances of the boundary between type-I and type-II superconductors into the more conventional hadronization models. Hadronization physics is ripe for introducing and adapting well-documented vortex-vortex interaction [210, 211] phenomena from superconductor physics.

3.3 Cluster Model

The cluster model [28, 166] starts from the notion of preconfinement [212], where the evolution of partons from the hard process can be calculated with perturbation theory, up to a 'preconfinement' scale. This results in finite mass clusters of colourless combinations of partons, decoupled from the scale of the hard process, and indeed the total centre of mass energy of the collision [92].

The first stage of the cluster model in Herwig is to take partons and put them on-mass-shell. In particular, a non-perturbative parameter in the cluster model is the constituent mass of the gluon, m_g, which controls how much phase space is available for the kinematics and flavour of quark-antiquark produced pair. In Herwig, all quarks are massive during the non-perturbative stages of hadronization modelling, and the masses used are the constituent masses[6]. In theory, diquark pairs may be produced via the same mechanism, though this would only be consistent with showers that end at a larger cutoff than typical, since at this point m_g would have to be significantly larger than the shower cutoff. After making every gluon massive with mass m_g, Herwig isotropically splits these gluons into light quarks, with the option for strangeness production [213]. In Chap. 4, we present a publication which reparameterizes strangeness production during the non-perturbative gluon splitting process, as well as during the cluster fission and decay (see Sec. 3.3.1). After gluon splitting, the event only contains colour-connected quark-antiquark pairs, called clusters. Once all gluons have been split, nearest neighbours in colour space are paired up to form colourless clusters, i.e. the leading-colour colour-topology produced in the parton shower is retained. This choice is motivated by the fact that for angular-ordered showers in electron-positron collisions, the nearest neighbours in colour space are nearest neighbours in phase space [28].

Clusters should be viewed as the highly excited progenitors of the hadrons detected, with a universal mass spectrum at LEP, independent of the hard process scale, in dijet production in e^+e^- annihilation. For proton-proton collisions, this universal mass spectrum property begins to break down, due to the nature of multiple parton interactions and the corresponding colour structures.

3.3.1 Cluster fission and decay

Like the string model, the cluster model can produce $q\bar{q}$ pairs from the vacuum, breaking the cluster in two. There are two types of this pair-production: cluster fission and

[6]The constituent mass value of a quark is model dependent, but typical masses for up and down quarks are approximately one-third of the proton mass, i.e. $m_u, m_d \sim 330$ MeV, since three of them are required to form the proton.

cluster decay. The two stages are schematically outlined in Fig. 3.11. Heavy clusters undergo cluster fission, which breaks a cluster up into either two lighter cluster, or a lighter cluster and a hadron. The latter case may be compared with the string fragmentation mechanism, though the exact mechanism and momentum redistribution may be different.

Clusters too light for fissioning undergo cluster decay, where hadrons are produced. Clusters produced from fissioning will also undergo cluster decay. In cluster decay, a cluster may decay into one or two hadrons, depending on the kinematics of the situation. In the latter case, energy-momentum conservation can be done immediately. In the former, momentum has to be reshuffled with neighbouring clusters in order to conserve energy and momentum.

3.4 Colour Reconnection

If two MPI have outgoing partons that are close together in phase space, then one would expect that they can interfere during the parton shower[7], due to the limited number of colours in QCD. However, since the parton shower is formulated in the leading-colour approximation, interference effects between different colour-ordered amplitudes are neglected.

Indeed, even if the two MPI did not have an overlap in momentum space, they must be correlated via some common colour-topology, since they were both produced from the same initial pair of colourless protons. This ambiguity in the colour structure of MPI can have drastic effects on the overall colour structure of an event.

As the leading-colour approximation drops suppressed terms of $\mathcal{O}(1/N_c^2)$, it is ignoring corrections that can contribute $\sim 10\%$ for $N_c = 3$. In precise predictions, the approximation requires some corrections, one method of which is colour reconnection (CR). The historical aspects of colour reconnection on precise measurements are reviewed in depth in [214]. As the points above highlight, there are two reasons for including colour reconnection [215]: first, as a corrective measure for small errors in e.g. the leading-colour approximation, which one may refer to as *static* CR;

[7]In the purely energy-momentum framework, there is no notion of spatial separation. If one introduces spacetime coordinates, and the parton showers in each MPI occur at shorter scales than the transverse separation of the two MPI, then the interference effects may be neglected.

and second, as a means of approximating the dynamical exchange of extremely soft, long-range gluons between different parts of an event, also known as *dynamic* CR.

The first example of colour reconnection as it applies to Monte Carlo event generators arrived with the original MPI model developed in [17], where it was a necessary ingredient to explain the rising average transverse momentum distribution with respect to multiplicity. Here, colour reconnection rearranged the strings' colour topologies to reduce the string 'length' λ:

$$\lambda = \sum_{i,j} \ln\left(\frac{m_{ij}^2}{m_0^2}\right), \tag{3.11}$$

where the sum runs over the string colour-connected pairs of partons i and j. By minimizing the string length, the total invariant mass of the string is also lowered. Less massive strings produce on average fewer hadrons, resulting in an increase in the average transverse momentum.

Colour reconnection is typically implemented in event generators as a non-perturbative phenomenon, though recent work has aimed to approach the problem in a number of ways: from a perturbative perspective during the parton shower [216–218], using perturbative colour evolution as inspiration for new models [219], or using the colour structure and rules of full QCD to guide the colour reconnection model [197]. We will now review the different colour reconnection models in the string and cluster hadronization models.

3.4.1 String-Based CR

Several different models for string-based colour reconnection in Pythia have been developed since its inception [214]. We have included a schematic diagram of how colour reconnection can work for an example pair of strings in Fig. 3.12. As mentioned above, the original model for string-based colour reconnection was based on the colour structure produced when generating multiple parton interactions, and merged partons from an MPI with low-$p_\perp$ with those from a high-$p_\perp$ MPI probabilistically. The CR model is biased towards low transverse momentum MPI, which have a larger spatial extent, and continues attempting to reconnect increasingly higher $p_\perp$ MPI systems, with decreasing probability.

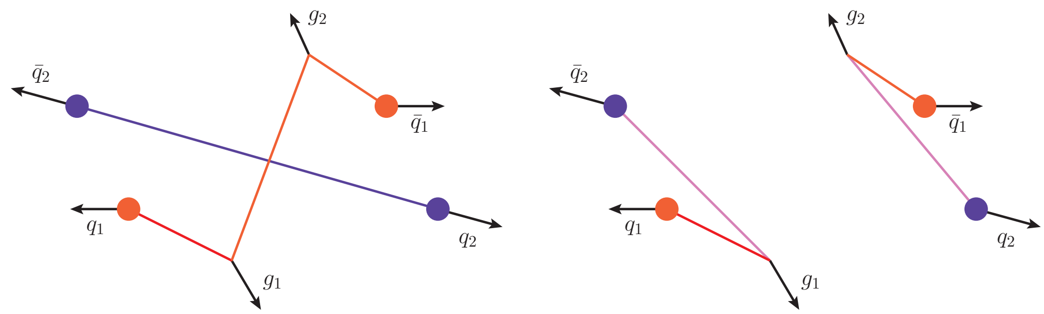

Figure 3.12: Schematic diagrams of two strings (*left*) before colour reconnection, and (*right*) after. Colour reconnection can change the colour topology of an event by reconnecting different partons from two different Lund strings to minimize global string 'length'. Quark endpoints are denoted as full circles, and kinks in the structure are connecting gluons (see Fig. 3.10).

Double boson production, e.g. $e^+e^- \to W^+W^-$, at LEP in principle provided an excellent theoretical test-bed for how colour reconnection is tied to spacetime separation [220]. The double boson system can decay via hadronic channels, creating a colour disconnected pair of quark-pair systems: $q_1\bar{q}_1$ and $q_2\bar{q}_2$. Since the bosons will decay at different spacetime points, and the quark-antiquark pairs will themselves develop a spatial separation, the colour reconnection model uses spacetime information to guide the colour-topology modifications. The CR model also had two variants, one for each type of superconductor (see Sec. 3.2.4). While the model is very powerful at modelling the clean environment of electron-positron collisions, it has not been extended to hadronic collisions yet.

In [197], the colour reconnection model uses the gauge group structure of QCD to probabilistically modify the colour topology of strings, while also allowing more complex and rich string structures to form. It also ensures that the colour connections between the MPI as they are produced from the beam remnant can have non-trivial colour correlations, as an attempt to go beyond the usual leading-colour MPI colour structure.

3.4.2 Cluster-Based CR

Since the first step of the cluster model is to kinematically remap the partons to have their constituent mass, and then to force all gluons at the end of the shower to non-perturbatively split into $q\bar{q}$ pairs, cluster-based colour reconnection occurs after this stage, but before cluster fission and decay.

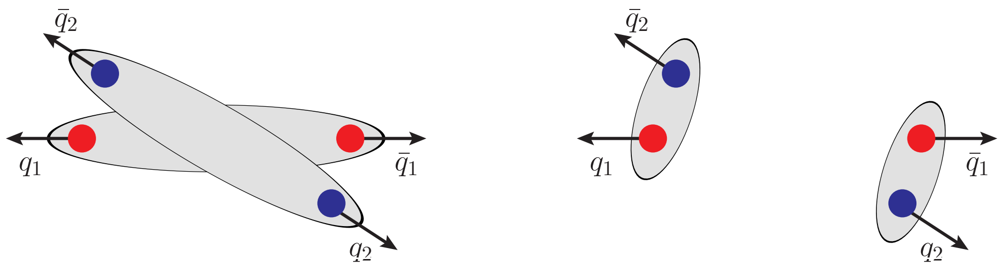

Figure 3.13: Schematic diagrams of two clusters (*left*) before colour reconnection, and (*right*) after. Cluster colour reconnection aims to minimize the sum of the two cluster masses and probabilistically reconnects the cluster constituents accordingly.

Three different models for cluster-based colour reconnection have been investigated in Herwig 7: Plain [221], Statistical [221], and Baryonic [213]. Plain CR aims to minimize the sum of cluster masses in a pair-wise fashion, as shown in Fig. 3.13. For a given cluster, the plain CR algorithm finds the corresponding cluster (if there is one) that gives the smallest reconnected mass sum, and accepts with a constant probability. It applies this sequentially to all the clusters in the event, removing any reconnected clusters as it does so. This model does not find the global minimum which is not only computationally expensive and unfeasible for environments such as proton-proton collisions which can have many tens of clusters, but most likely unphysical, but instead finds a local minimum. It should also be noted that cluster reconnections that would produce clusters in an octet (i.e. they come from the same gluon splitting that produced them) are automatically vetoed [221, 222].

Statistical CR is a simulated-annealing [223] method of performing colour reconnection, aimed at providing an approximate solution to the mass sum minimization problem. Statistical CR, much like the plain CR model, aims to minimize the total sum of cluster masses during its reconnection process. However, rather than considering each cluster individually and looking for the partner that minimizes the cluster mass sum of the pair, the statistical CR model selects random pairs of clusters from the event. Treating colour reconnection as a thermodynamic-type problem, if the sum of cluster masses is lowered by a potential reconnection, this reconnection is immediately accepted, with a probability of 1. Otherwise, if the mass sum would increase, the reconnection is accepted with the probability:

$$p_{\mathrm{acc}} = \exp\left(\frac{-\Delta\lambda}{T}\right), \tag{3.12}$$

where $\Delta\lambda = \sum\left(m^2_{\text{post}}\right) - \sum\left(m^2_{\text{pre}}\right) \geq 0$ is the change in invariant mass sum after performing colour reconnection. The temperature-type parameter T controls the number and size of possible mass increases, slowly lowered over the runtime of the model, analogous to the clusters 'cooling' down. While an interesting model, it has many more parameters than the plain CR model, without any sizeable changes in the comparisons to data [221].

Baryonic CR extends the cluster model from simple $q\bar{q}$ pairs to also include so-called baryonic clusters of triplets of (anti-)quarks that then get converted to a diquark-quark pair during cluster fission and decay. The baryonic CR algorithm works as follows: for a given cluster, boost back to its rest frame, and search for clusters that have the largest rapidity span along the given cluster's quark axis. If the largest span is aligned in the same direction, i.e. the orientation of the $q\bar{q}$ systems is the same, then the type of reconnection will be a baryonic one. The algorithm will then select the cluster with the second largest rapidity span to perform a baryonic reconnection, converting three conventional clusters into two baryonic clusters (a triple quark cluster and a triple antiquark cluster). If instead the largest rapidity span is anti-aligned with the given cluster's quark axis, then the reconnection will be a so-called mesonic one, analogous to the plain CR algorithm above.

By transforming to the rest frame of a given cluster and using rapidity span maximization, the baryonic CR algorithm circumvents the issue of comparing cluster masses before and after colour reconnection. Baryonic clusters are typically heavier than the conventional clusters, and indeed, comparing the sum of three masses to two is somewhat an unbalanced comparison, thus rendering a mass-based CR algorithm unfeasible. By using rapidity span maximization, the baryonic CR algorithm is able to select cluster constituents that are flying in similar directions, which has the same physical intuition involved in mass minimization algorithms. One shortcoming of the model is that baryonic clusters cannot be created outside of the colour reconnection algorithm, nor can they currently re-reconnect, i.e. they can only be produced, not destroyed. However, recent studies of soft gluon evolution inspired colour reconnection have allowed baryonic cluster creation and destruction [219].

While the baryonic CR model improves Herwig's description of baryonic observables, it does not have a spacetime description. This results in an algorithm that does

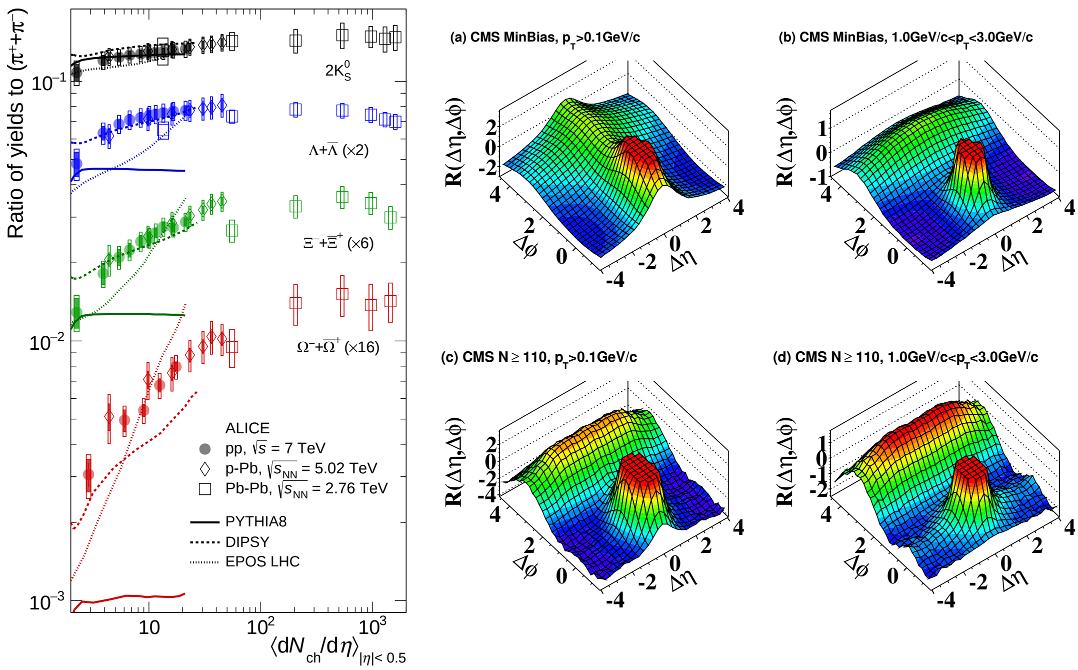

Figure 3.14: Evidence for collective effects in proton-proton collisions: (*left*) strangeness enhancement as a function of particle multiplicity observed by ALICE [31] and (*right*) near-side ridge effect in high-multiplicity events observed by CMS [35].

not have any notion of spacetime separation and as a result causality. Chap. 5 presents a framework to introduce spacetime coordinates during the multiple parton interactions and the end of the parton shower. These coordinates combined with rapidity will then be used as the CR measure that we aim to minimize in the baryonic CR model.

3.5 Collectivity in Proton-Proton Collisions

While both the Lund string model and the cluster model have had a large amount of success at describing a wide variety of final-state observables at the LHC, recent evidence from ALICE and CMS have pointed to some severe shortcomings in the two approaches. Two major pieces of evidence of collective effects have been reproduced in Fig. 3.14, namely the strangeness enhancement as final state particle multiplicity increases observed by ALICE, and the near-side ridge effect in high-multiplicity events observed by CMS, which are discussed below.

Strangeness enhancement has been seen by ALICE [31,33,224] and ATLAS [39], where it appears to be easier to produce mesons and baryons containing strange quarks[8] than the Lund string model and the cluster model can explain. In both models, non-perturbative strangeness production is given by a constant weight that is the rate of suppression of $s\bar{s}$ pairs relative to up or down pairs. Due to this probability being static, the left panel of Fig. 3.14 showcases the utter failure of the Lund string model to describe strange-containing hadrons as a function of charged multiplicity, i.e. the total number of charged particles detected. The solid flat line in the left panel of Fig. 3.14 highlights the Lund string model's agnosticism to multiplicity, since the production rate solely depends on the produced quark's mass, and has no understanding of the dynamics of the event. The two models that are better able to describe the strangeness enhancement are the Dipsy-implemented[9] [226] rope model [209], and the heavy-ion inspired event generator EPOS [227,228].

The other major piece of evidence for collective effects is the so-called near-side ridge seen in high multiplicity events at CMS [35,36]. CMS uses a 'distance' measure between a pair of detected particles i, j, which is defined as:

$$R_{ij}^2 = (\eta_i - \eta_j)^2 + (\phi_i - \phi_j)^2 , \tag{3.13}$$

where η is the pseudo-rapidity of the particle:

$$\eta = \frac{1}{2} \ln \left(\frac{|\vec{p}| + p_L}{|\vec{p}| - p_L} \right) , \tag{3.14}$$

where $\vec{p}$ is the 3-momentum of the given particle, p_L is the longitudinal component, and ϕ is the azimuthal angle of the particle's momentum. Plotting R_{ij}^2 in Eq. 3.13 for every particle pair (excluding self correlations) and normalizing to background correlations, one obtains the right-side set of plots in Fig. 3.14. In the bottom right panel, there are three distinctive features: a peak at $(0, 0)$ corresponding to intra-jet particles, i.e. a large number of hadrons all travelling in a collimated spray; a far-side ridge at $\Delta\phi \sim \pi$ corresponding to energy and transverse momentum conservation; and lastly, the near-side ridge at $\Delta\phi \sim 0$. It is this final feature that the Lund string model and the cluster model cannot describe. In heavy-ion collisions, this is a well-known feature attributed to the quark-gluon plasma (QGP) expanding outwards, creating az-

[8] Hadrons containing at least one strange quark are sometimes collectively referred to as hyperons.
[9] It has also been implemented in Pythia and Angantyr [225].

imuthal correlations as a result of the non-trivial geometric spacetime structure of the dense medium of the QGP and the resultant impact this structure has on propagating partons.

The main shortcoming in both of these hadronization models is that the fundamental object in each model (the string and the cluster respectively) has almost no knowledge of any other such object in a given event. Typically the only way to allow strings or clusters to 'interact' with each other is via colour reconnection. Recent work suggested that colour reconnection [229] can produce some of the flow-like correlations detected. As described in Sec. 3.4.2, baryonic colour reconnection [213] was developed to better model strangeness enhancement and the overall description of baryon production in Herwig 7, using the results from ALICE [31] as inspiration. Similarly, the effects of colour reconnection on hadron-flavour observables in Pythia were studied in [230]. While these studies on colour reconnection have shown some promise, there are no conclusive results yet.

There have been a wide variety of attempts to model the collective phenomena at the hadronization level. A study of the string fragmentation model in Sec. 3.2.2 investigated modifications to the transverse momentum distribution inspired by thermodynamics [231]. Rope hadronization [209] allows nearby strings to form a colour rope of a higher colour-multiplet. The roots for the rope and shoving model lie in results from lattice QCD [183,232], which found Casimir scaling in the potential between higher multiplets compared to the baseline potential between a quark-antiquark pair. Interpreting this as an increase in string tension and building so-called ropes out of the Lund strings, the rope model was able to better describe the enhancement of strangeness and baryon production via the popcorn mechanism.

The shoving model [233, 234] pushes overlapping strings apart transversely by adding a series of very soft gluon kicks to each string. EPOS [227, 228, 235] uses a hadronization model based on string density, whereby strings produced on the peripheries of a collision, called the corona, act as if they are in relative isolation. Meanwhile, strings produced in the centre of a collision, called the core, will hadronize collectively in a heavy-ion inspired manner. In Chap. 6, we present a framework to allow two strings to interact with each other by compressing longitudinally and repelling off each other transversely during string fragmentation.

4

Strangeness in the Cluster Model

Just as the strong coupling α_s runs, as discussed in Sec. 2.2, the masses of quarks entering into the QCD Lagrangian in Eq. 2.6 must also be renormalized and consequently they scale with energy. This scaling is dependent on the renormalization scheme one chooses. A typical choice is the $\bar{\text{MS}}$ scheme [43, 47, 68], a modification of the minimal subtraction scheme [236, 237]. The so-called 'current' masses are calculated in an analogous fashion to the steps for the strong coupling. Current masses are not suitable for non-perturbative, low-energy physics, since their definition and calculation belong to the perturbative regime. If the current masses in Tab. 2.1 are used in Eq. 3.7 for the Lund string model, the relative production rate for up : down : strange quarks is approximately $1 : 1 : 0.87$, suggesting that strangeness is produced at roughly the same rate as up and down quarks.

Another mass for quarks is the so-called constituent mass, where hadrons (and their mass) are created by "gluing" together constituent quarks. The masses of constituent quarks is calculated by comparing the quark content of hadrons, singling out the appropriate flavour, and taking the effective mass difference. This provides a rough effective mass for a valence quark caused by the interaction of the valence quark and the sea gluons and quarks. Using constituent quark masses of $m_u = m_d = 330$ MeV and $m_s = 486$ MeV in Eq. 3.7, results in a drastically different set of production rates: $1 : 1 : 0.14$. Due to the ambiguity in the choice of quark masses, strangeness production at the non-perturbative level in both the string and cluster model is implemented as a tuneable free parameter of the model. For example, in Pythia, the production rates of strange quark-antiquark pairs relative to up or down pairs is approximately

0.22, which is somewhat close to the constituent masses value seen above.

However, having this free tuneable parameter is not a fully satisfactory solution, for several reasons. Firstly, while these constant weights are useful parameters in tuning and modelling average effects in event generation, they offer no insight into how the topology of the event impacts the rate of strangeness production. Recent extensions to the string model [209,231] have demonstrated that modifying the strangeness production rate according to the environment in a given event can give a better description of the strangeness enhancement that has been seen by ALICE.

Secondly, as we show in Sec. 4.1, the values of the cluster strangeness production rate that result from tuning to e^+e^- data and LHC minimum bias data independently do not match up well, and present vastly different explanations of strangeness production during the cluster evolution in the cluster model. In particular, at e^+e^-, strangeness production is preferred during the cluster fission and decay stages, while at LHC, the main source of non-perturbative strangeness arises from the non-perturbative gluon splitting mechanism.

In the publication presented in Sec. 4.1, we study the modelling of the sources of non-perturbative strangeness in the cluster model in Herwig. We devise a simple model that reparameterizes the strangeness production for the three main stages of cluster physics: production, fission, and decay. The model is motivated by the strangeness enhancement seen at ALICE [31], and changes the relative production rates from constant average weights to dynamic probabilities that depend on the topology of a given event. The reparameterization uses the invariant mass of the relevant system in a given stage of the cluster model. We present two tunes for the new parameterization, one for e^+e^- and one for LHC minimum bias respectively, and show an improvement in the description of Kaon production rates (the lightest hadron containing a strange quark).

4.1 Published Material

Kinematic Strangeness Production in Cluster Hadronization

Cody B Duncan and Patrick Kirchgaeßer

Published in The European Physical Journal C 79 no. 1 (2019) 61

DOI: 10.1140/epjc/s10052-019-6573-2

e-Print: arXiv:1811.10336 [hep-ph]

MCNET-18-29, CoEPP-MN-18-9, HERWIG-2018-04, KA-TP-34-2018

Paper begins overleaf

Eur. Phys. J. C (2019) 79:61
https://doi.org/10.1140/epjc/s10052-019-6573-2

THE EUROPEAN PHYSICAL JOURNAL C

Regular Article - Theoretical Physics

Kinematic strangeness production in cluster hadronization

Cody B. Duncan[1,2,a], **Patrick Kirchgaeßer**[2]

[1] School of Physics and Astronomy, Monash University, Clayton, VIC 3800, Australia
[2] Institute for Theoretical Physics, Karlsruhe Institute of Technology, 76128 Karlsruhe, Germany

Received: 30 November 2018 / Accepted: 20 December 2018 / Published online: 28 January 2019

Abstract We present a modification to the non-perturbative strangeness production mechanisms in the Monte-Carlo event generator Herwig in order to make the processes more dynamic and collective. We compare the model to a series of observables for soft physics at both LEP and LHC.

1 Introduction

The non-perturbative elements of simulating LHC events remain an active area of research in light of recent ALICE and CMS data [1,2]. Signs of strangeness enhancement and collective effects in high multiplicity events respectively have inspired several phenomenological models, ranging from interacting strings [3,4], to relativistic hydrodynamics [5], to tweaks to the existing multiple parton interaction mechanisms [6] and colour reconnection [7,8] models. Monte Carlo event generators [5,9–11] provide a useful testing ground for these models.

Arguably the most successful models of hadronization which try to reproduce strangeness enhancement in high-multiplicity events are rooted in the physics of collectivity, where the dense environment of high multiplicity events leads to more complicated systems which interact with one another. Heavy ion event generators typically prefer a hydrodynamic viewpoint, where the quark-gluon plasma acts as a perfect fluid, changing the dynamics of hadronization. High-energy pp event generators tend to use sophisticated iterations of the more conventional proton collision techniques, such as the DIPSY rope model where several overlapping Lund strings [12] combine into a higher-representation colour field, which then may enhance strangeness production and may also shove each other transversely outwards, mimicking the fluid behaviour of quark-gluon plasma. Another model [13] has attempted to use a thermodynamics inspired route to string fragmentation and was able to explain a harder transverse momentum spectrum for heavier particles.

Herwig [9] has recently developed a new model for colour reconnection, where baryonic clusters were allowed to be produced in a geometric fashion [8], in an attempt to explain the results of [1]. The model was able to create heavier hadrons, and in particular more baryons, but in order to better describe the data, the non-perturbative gluon splitting mechanism was allowed to produce $s\bar{s}$ pairs as well as the default lighter species. However, the production weight was simply set to a flat number, tuned to Minimum Bias events at the LHC. In this paper, we will mainly focus on the fundamental mechanisms of strangeness production in cluster hadronization, namely the production rate of $s\bar{s}$ pairs during non-perturbative gluon splitting, cluster fission, and cluster decay. In doing so, we are taking the first steps to a rework of strangeness production in the Herwig hadronization phase. A full model would also need to consider colour reconnection, since this rearranges the colour topology and thus the mass distribution inside an event, affecting the scaling that we are interested in studying.

In this study, we aim to introduce a simple dynamic model of strangeness production in Herwig, in which each non-perturbative production stage uses the kinematic information of the relevant surrounding colour-singlet system. After reviewing the current mechanisms of hadronization in Sect. 2, we perform two separate tunes to a number of light strange meson observables for LEP and LHC Minimum Bias events in Sect. 3. We show that the tuned current strangeness production parameters are drastically different between the two collider types, and propose a mass-based scaling for the relevant production weights in Sect. 4, comparing two different mass-like measures to scale the probability. In Sect. 5, we tune our new model and compare the results with the old model in Herwig, as well as perform a comparison to the default Lund string model in Pythia [10] with the Monash tune [14]. We briefly summarize the work and possible future avenues for research in Sect. 6.

[a] e-mail: cody.duncan@monash.edu

2 The Herwig Hadronization Model

To accurately describe a full QCD event, one must be able to model the non-perturbative physics contributions, e.g. hadronization of individual quarks & gluons from the parton shower and the multiple parton interactions to form colour-singlet hadrons.

Figure 1 sketches a schematic event, focusing on the final state. After generating a hard matrix element for the event, Herwig performs a parton shower, producing a number of soft and collinear partons. After the parton shower reaches $\mathcal{O}(1)$ GeV, the hadronization phase of simulation occurs. In Herwig, the hadronization model is the cluster model [15], based on the colour preconfinement [16] property from the angular-ordered parton shower. A cluster can be considered to be a highly primordial, excited colour-singlet $q\bar{q}$ pair.

There are several parts to the hadronization model in Herwig, in the following algorithmic order:

- Non-perturbative gluon splitting,
- Colour reconnection,
- Cluster fission,
- Cluster decay to hadron pairs,
- Unstable hadron decays.

In Fig. 1, we have omitted colour reconnection since this step simply changes the colour topology of the event, not the content of the clusters. While modifying the colour reconnection algorithm would have a non-trivial impact on the later stages of hadronization, namely cluster fission and decay, it is outside the scope of this paper, but these correlations will be studied and addressed in future work. Since the scope of this project is mainly focused on light strange hadron production, we tune predominately to pion and kaon observables. We will also ignore unstable hadron decays for the purposes of this paper.

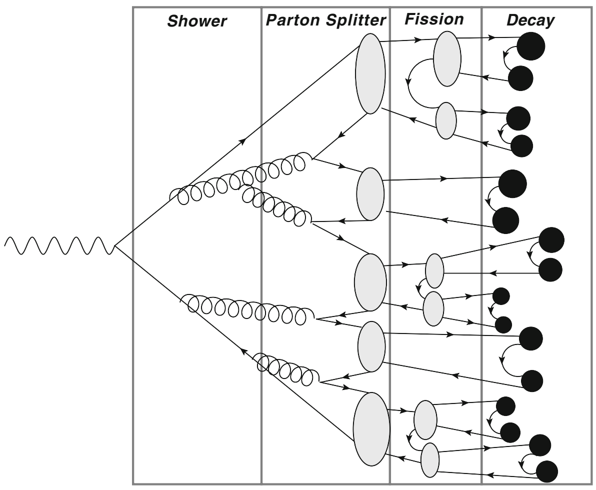

Fig. 1 Figure of a simplified event where we show the major stages of hadronization after the parton shower that can contribute to non-perturbative strangeness production. Grey ellipses are clusters, while black are hadrons

The three other listed stages in hadronization are each allowed to contribute to the overall strangeness in the event, since they each produce new $q\bar{q}$ pairs. We briefly recall the details of each step as presented in depth in [9].

2.1 Non-perturbative gluon splitting

Once the parton shower ends, all gluons undergo a non-perturbative splitting into $q\bar{q}$ pairs. The species of the pair is determined by a given weight, e.g. in the tune from [8] the weights of up, down, and strange are 2:2:1. The default version of Herwig does not allow for strangeness production at this step, only $u\bar{u}$ and $d\bar{d}$ pairs. The only constraint on the gluon splitting is that the gluon mass is at least twice the constituent mass of the species in question, and the gluons are split isotropically.

After all the gluons in an event have been split, nearest neighbours in momentum space are most likely to be nearest neighbours in colour space [16], and clusters are formed from the momentum-space neighbouring $q\bar{q}$ pairs, with a mass distribution decoupled from the hard scattering process that created them.

2.2 Cluster fission

Exceptionally heavy clusters are allowed to fission into two lighter, less excited clusters if the mass M of the original cluster satisfies the condition:

$$M^p \geq q^p + (m_1 + m_2)^p, \tag{1}$$

where p and q are parameters that control the fissioning rate criteria, and $m_{1,2}$ are the parton masses of the heavy cluster. In Herwig, p is given separate values for light quarks (u, d, s), charm, and bottom. The light quark weights are further subdivided, and strangeness is suppressed by a flat weight. q has a similar divide between the quark species.

After selecting clusters to fission, the cluster fissioner produces a $q\bar{q}$ pair from the light quarks with a fixed weight, distinct values for each flavour of quark (bar top), and diquarks. Each parton from the pair go into a separate cluster, giving the new pair of clusters a mass distribution of:

$$M_i = m_i + (M - m_i - m_q)R_i^{1/w}, \tag{2}$$

where w is the splitting parameter that controls the rate of splitting for clusters containing different species of quarks.

2.3 Cluster decay

The last stage of cluster-based physics is at the cluster decay level, in which clusters decay into excited hadrons. Given a cluster with constituents $q_1, \bar{q}_2$, the weight for producing hadrons $h_a = q_1\bar{q}, h_b = q\bar{q}_2$, where q denotes a quark or diquark species, is given by:

$$\mathcal{W}(h_a, h_b) = P_q w_a s_a w_b s_b p^*_{a,b}, \tag{3}$$

where P_q is the production weight for the given quark or diquark species, w_i are the weights for the relevant hadron production, and s_i are the suppression factors for the corresponding hadrons. The final factor in the weight is the two-body phase space factor that controls how readily the cluster can decay into the two chosen hadrons.

2.4 Herwig strangeness parameters

The Herwig parameters that control non-perturbative strangeness production are the gluon splitting weight - `SplitPwtSquark`, and the cluster fission & decay weight - `PwtSquark`. In the original model, cluster fissioning and cluster decaying are controlled by the same parameter. The first step in our understanding of the different contributions is to disentangle cluster fission from cluster decay and introduce one additional parameter which controls the production of a $s\bar{s}$ pair during cluster fission - `FissionPwtSquark`. The decay parameter remains the same.

3 Tuning of the existing model

In this section we tune the parameters for strangeness production of the existing model first to LEP and then to LHC data. Hadronization models are typically tuned to LEP data if they do not rely on pp-specific event topology, e.g. multiple parton interactions and their effects on colour reconnection, since LEP provides a clean QCD final state environment which imposes relatively strict constraints on what one's hadronization model is allowed to do.

The tuning is achieved by using the Rivet and Professor frameworks for Monte Carlo event generators [17,18]. In order to understand the overall effects of strangeness production on different stages of the event generation, we keep all other hadronization parameters that were previously tuned to LEP data at their default values [9,19]. In the first tune (TUNE1), we only consider the effects of the parameters that are *directly* responsible for strangeness production as explained in Sect. 2.

In a second tuning attempt (TUNE2), we introduce the new parameter for the cluster fission stage. Tuning these 3 different parameters will allow us to study the phases of strangeness production during event generation and will shed light on the differences between LEP and LHC.

We note that this section is an extended part of the introduction to visualize and highlight the effects of the aforementioned different parameters and to see at which stage non-perturbative strangeness production is preferred.

3.1 LEP tuning

For the tuning to LEP data, the following observables from ALEPH [20,21], DELPHI [22], SLD [23] and PDG hadron multiplicities [24], which represent a good description of event shapes and π, K multiplicities, were used with equal weights:

- Mean charged multiplicities for rapidities $|y| < 1.0$, $|y| < 1.5$ and $|y| < 2.0$
- K^0 spectrum
- Mean π^0 multiplicty
- Mean $K_S + K_L$ multiplicity
- Mean K^0 multiplicity
- Mean π^+/π^- multiplicty
- Mean K^+K^- multiplicity
- Ratio (w.r.t $\pi^\pm$) of mean $K^\pm$ multiplicity
- Ratio (w.r.t $\pi^\pm$) of mean K^0 multiplicity
- $K^\pm$ scaled momentum

The resulting parameter values for the two different tunes are listed in Table 1.

While being able to describe all the considered LEP data on equally good footing, we improve the simulation of the observables which were considered in the tuning procedure. TUNE2 gives better agreement to the data, at least with respect to the $K^\pm$ multiplicity, highlighting the necessity to disentangle the cluster fission and cluster decay parameters. The corresponding plots are shown in Fig. 2, where we compare the default version with our two new tunes.

Table 1 Results of the parameter values for strangeness production at the different stages of the event generation (LEP). In both default Herwig and TUNE1, cluster fission and decay have the same parameter. In TUNE2, they are allowed to be different, but the tuning procedure returned equal values. In default Herwig, there is no $g \to s\bar{s}$ option

LEP	Default	TUNE1	TUNE2
Gluon Splitting	–	0.24	0.19
Cluster Fission	0.66	0.53	0.69
Cluster Decay	0.66	0.53	0.69

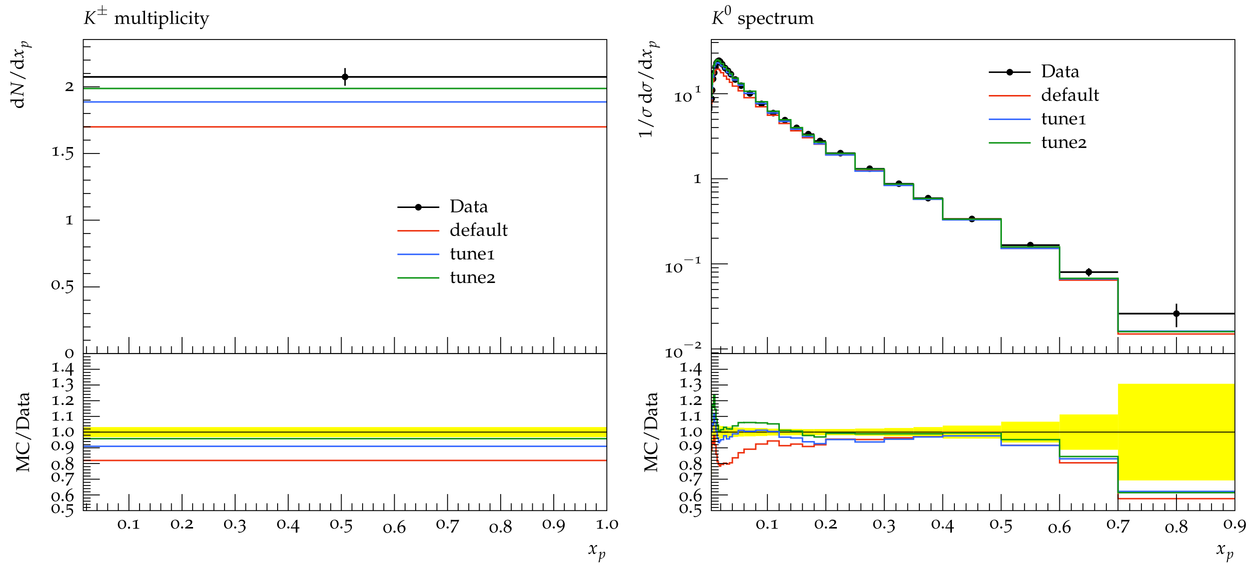

Fig. 2 Measurement of $K^{\pm}$ multiplicities at SLD [23] and K^0 spectrum as measured at ALEPH [20] for $\sqrt{s} = 91.2$ GeV. We show a comparison between the default Herwig model and our two different tunes

3.2 LHC tuning

For the tuning to LHC data, we solely focus on identified particle distributions which were measured at ALICE [25] and CMS [2]. We limit the tuning to a center of mass energy of $\sqrt{s} = 7$ TeV due to the lack of suitable available Rivet analyses at higher energies. The following observables were considered in the tuning procedure with equal weights:

- $K^+ + K^-$ yield in INEL pp collisions at $\sqrt{s} = 7$ TeV in $|y| < 0.5$
- K/π in INEL pp collisions at $\sqrt{s} = 7$ TeV in $|y| < 0.5$
- K^0_S rapidity distribution at $\sqrt{s} = 7$ TeV
- K^0_S transverse momentum distribution at $\sqrt{s} = 7$ TeV

The resulting parameter values are shown in Table 2.

The outcome of the tuning procedure is shown for the p_T distribution of $K^+ + K^-$ yields and the K/π ratio in Fig. 3.

Again the retuning of the default model with the incorporation of an additional independent parameter at the cluster fission stage improves the description of the considered observables significantly.

3.3 Summary

The general approach in tuning a hadronization model is to tune the parameters to LEP data and then assume it is able to describe LHC observables as well since hadronization is assumed to factorize and should not depend on the process involved.

Table 2 Results of the parameter values for strangeness production at the different stages of the event generation (LHC). In both default Herwig and TUNE1, cluster fission and decay have the same parameter, while in TUNE2 they are allowed to be different. In default Herwig, there is no $g \to s\bar{s}$ option

LHC	Default	TUNE1	TUNE2
Gluon Splitting	–	0.95	0.95
Cluster Fission	0.66	0.05	0.02
Cluster Decay	0.66	0.05	0.25

The main difference between LEP and LHC is the denser hadronic environment one encounters due to multiple parton interactions and therefore also the enhanced effect of colour reconnections on the distribution of final state particles. Be that as it may, we believe that the probability to produce strangeness e.g at the stage of non-perturbative gluon splitting should be a universal parameter and be independent of the process in question.

Since the data shows that clearly different parameter values are preferred at LHC and LEP the approach to have a single valued probability is not suited for the description of both LHC and LEP observables. It may capture the average effect but it does not allow for fluctuations on an event-by-event basis. We tackle this problem by assuming that the rate at which strangeness is produced depends on the hadronic density of the immediate environment, which will be discussed in the next section.

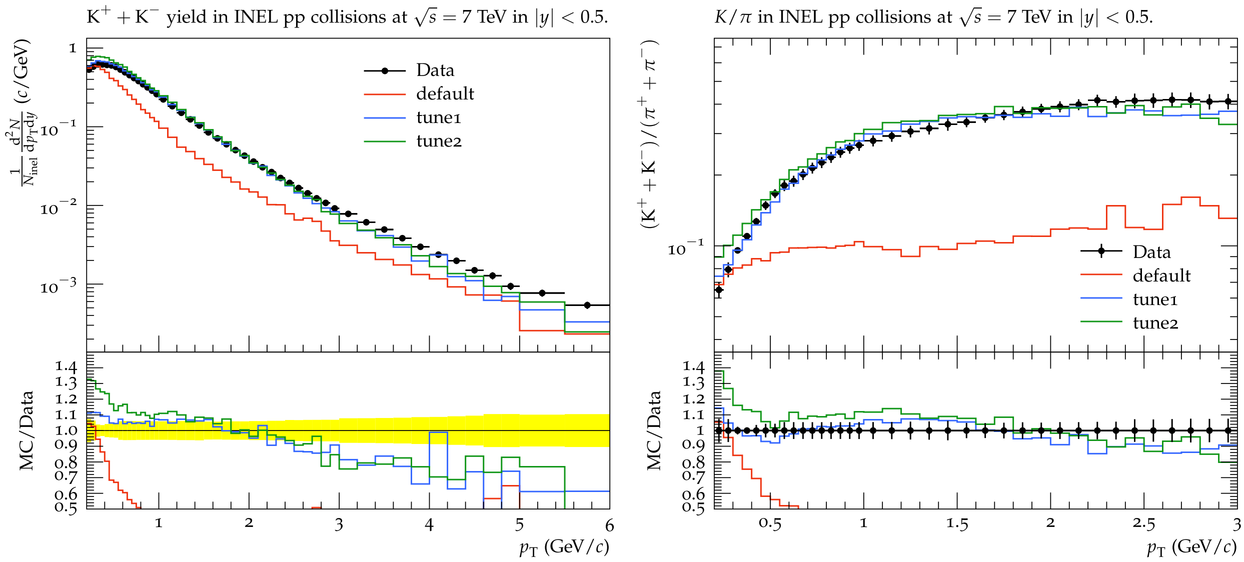

Fig. 3 Transverse momenta spectra for $K^+ + K^-$ and K/π ratio as measured by ALICE[25] at $\sqrt{s} = 7$ TeV in the central rapidity region. We show a comparison between the default Herwig model and our different tunes.

4 Kinematic strangeness production

As mentioned above, the various splitting probabilities and weights are flat numbers tuned to data, without any considerations for the topology of a given event. In order to have a more dynamic picture, where the splitting probabilities depend on the environment, we choose to scale the weights with respect to colour-singlet masses. The mass of a colour-singlet system at a given phase of hadronization scales the probability for strangeness production up or down, depending on a characteristic mass scale for each step.

As a simple starting point for mass-based power scaling, we replace the flat weights in each of the steps mentioned in Sect. 2 with the following functional form:

$$w_s(m)^2 = \exp\left(\frac{-m_0^2}{m^2}\right), \tag{4}$$

where m_0^2 is the characteristic mass scale for each phase, and m^2 is the total invariant mass of the relevant colour-singlet system. In this work, we will introduce another mass-based measure which replaces m^2 in the denominator of Eq. 4: the threshold production measure, λ. We discuss the difference in the two approaches in Sect. 4.3. For now, we will continue to use the total invariant mass as an example in the following sections.

The weights in Eq. 4 are only for strangeness production, and they are relative to the production weights of up and down quarks. In the limit of a very heavy colour-singlet, the rate of producing strangeness will be the same as that of the lighter quarks, while in the low-mass limit, only the lighter quarks will be allowed to be produced. The appeal of an exponential scaling is that this model only introduces one extra parameter to the default model of hadronization in Herwig, and indeed, it does not introduce any extra parameters if one splits the fission and decay parameters. Thus we avoid a proliferation of parameters in our model, and we still have a natural mechanism to allow for event-by-event fluctuations in strangeness production.

The scaling of the production rate in Eq. 4 only applies to $s\bar{s}$ pairs, and not to any diquarks containing strange quarks. Default Herwig does not allow gluons to non-perturbatively split into diquark-diantiquark pairs, nor does it allow these pairs to be produced during cluster fissioning and decay. Diquarks may only be produced as remnants of the incoming baryons, or from baryon-number violating processes [9]. Since diquark species would fundamentally affect the baryon yields, which we are not studying in this work, we leave diquark production considerations to a future rework of baryon production in Herwig.

4.1 Non-perturbative gluon splitting

At the end of the shower, instead of immediately splitting the gluons into $q\bar{q}$ pairs with the species determined by their given weights, we instead collect the various colour-singlet systems in the event, what we call *pre-clusters*. While colour preconfinement dictates that the mass distribution of clusters is independent of the hard energy scale, there are no such constraints on the masses of the colour-singlet pre-clusters. As shown schematically in Fig. 6, a parton shower can produce gluons and quark-antiquark pairs at a perturbative level,

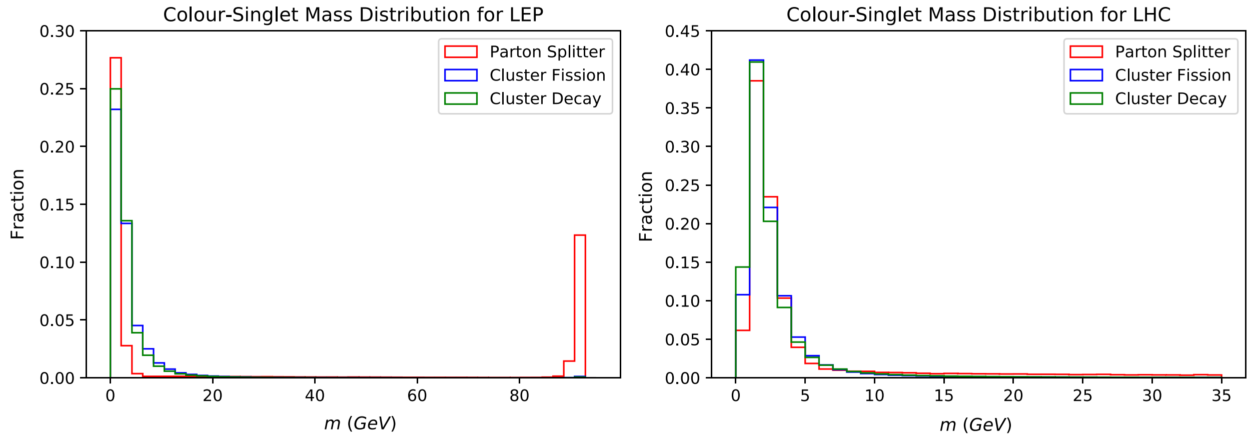

Fig. 4 Mass distributions for colour-singlet systems immediately before the Parton Splitter, Cluster Fissioner, and Cluster Decayer steps in LEP and LHC Minimum Bias events. Note the different mass axis scales

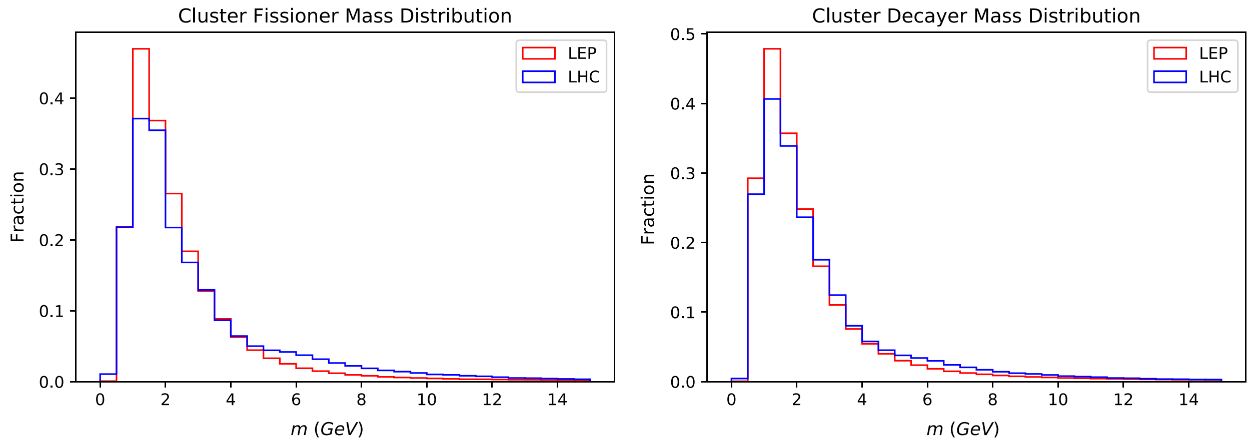

Fig. 5 Comparison of LEP and LHC Minimum Bias mass spectra of clusters immediately before cluster fission and cluster decay

separating the event into a number of different pre-clusters with a variety of masses.

Every gluon in the same pre-cluster will get the same weight, since they belong to the same colour-singlet system, and thus have the same mass measure for strangeness production, but since the species is picked probabilistically, this does not mean that all the gluons will produce strange quark-antiquark pairs. The constraint from default Herwig still applies, namely that even in situations where there is a very heavy pre-cluster, if a gluon cannot access the phase space necessary to split into a $s\bar{s}$ pair, then it will undergo the usual splitting to up or down quarks.

The characteristic mass scale for pre-clusters will unfortunately depend on the type of collider one uses. As shown in Fig. 4, there is a very broad tail for the proton colliders due to the number of pre-clusters that one can produce. This is a by-product of the type of dense and complicated final state environment of high energy hadron colliders. At LEP, there are two peaks for the pre-cluster mass distribution, one at close to 91.2 GeV, corresponding to events where there are only gluon emissions from the outgoing $q\bar{q}$ legs from the hard scattering process, and very few colour-singlets fall between the two peaks, due to the simple fact that perturbative gluon splitting is suppressed compared to perturbative gluon emission.

4.2 Cluster fission and decay

At the cluster fission and cluster decay level, the colour-singlet is the cluster itself. We allow the characteristic mass scale and characteristic production probability to be different for the two phases. As shown in Fig. 5, the typical cluster masses at the cluster fission and cluster decay stages are roughly similar for both LEP and LHC, which we hope to reflect in the characteristic mass scales for the two tunes. We note that Figs. 4 and 5 are plotted without turning on the exponential scaling, which would change the mass

Eur. Phys. J. C (2019) 79:61

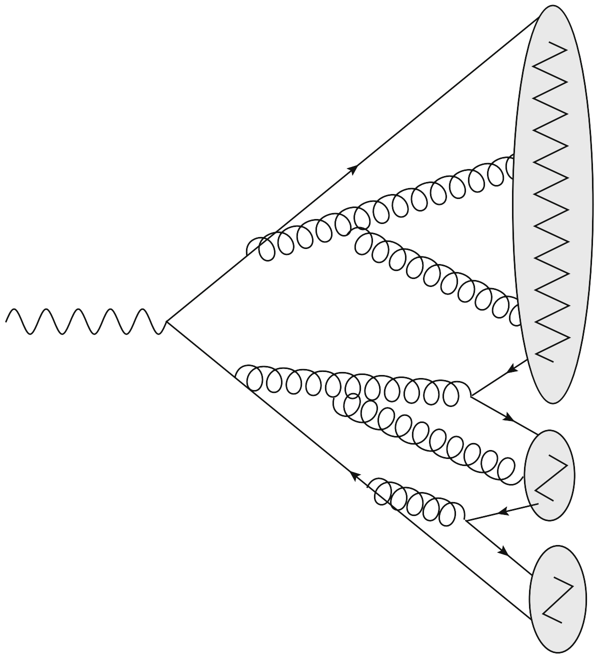

Fig. 6 Schematic topology of colour-singlets that can occur from perturbative gluon and quark shower splitting, before the gluons undergo non-perturbative splitting

distribution slightly, but the figures are benchmarks of the typical colour-singlet total invariant masses.

4.3 Colour-singlet masses

In the previous sections we have used the total invariant mass of the colour-singlet systems as the mass measure in Eq. 4, but there are issues with this approach. In using the total invariant mass of a given colour-singlet to scale the strangeness weight, we have neglected to take into account the massive nature of the partons in the pre-clusters and clusters. We argue that given two colour-singlets of the same total invariant mass, if one cluster has much heavier endpoints or constituents that the other, then the one with lighter endpoints or constituents should more readily produce $s\bar{s}$ pairs from the vacuum (Fig. 6).

Table 3 Results for the tuned characteristic mass scales m_0, in units of GeV, of our new model using the total invariant mass of a colour-singlet object for LEP and LHC tunes respectively

Invariant mass	LEP	LHC
Gluon Splitting	97	48
Cluster Fission	3	22
Cluster Decay	23	4

To remove the biasing effects of massive constituents, we have implemented another mass measure:

$$\lambda = m_{cs}^2 - \left(\sum_i m_i\right)^2, \tag{5}$$

where m_{cs}^2 is the total invariant mass of the colour-singlet system, and m_i are the invariant masses of the endpoints for pre-clusters or the constituent partons in a cluster.

Gluons are massive in Herwig, but because their masses are used to produce the $s\bar{s}$ pair, we do not include them in the subtraction term. The λ measure would replace the mass-based denominator in Eq. 4. We have presented the distributions of the λ measure for each of the stages in Fig. 7, and a comparison between the distributions of the two mass measures in Figs. 9 and 8. The λ measure has the appealing feature that if one produced a $s\bar{s}$ pair at the gluon splitting level, this extra mass wouldn't propagate extra strangeness enhancement further into the hadronization process.

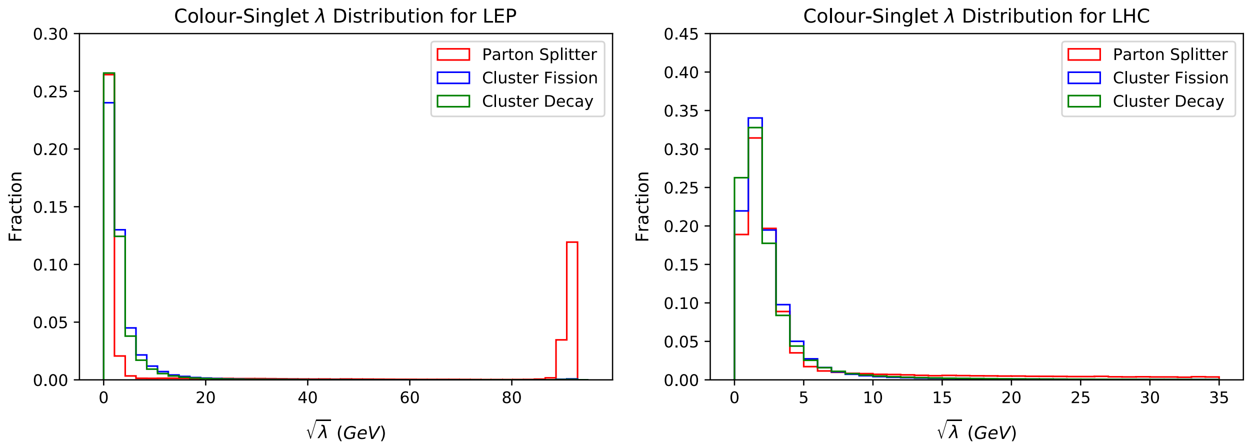

Fig. 7 Threshold mass, λ, distributions for colour-singlet systems immediately before the Parton Splitter, Cluster Fissioner, and Cluster Decayer steps at LEP events at 91.2 GeV and LHC Minimum Bias events at 7 TeV

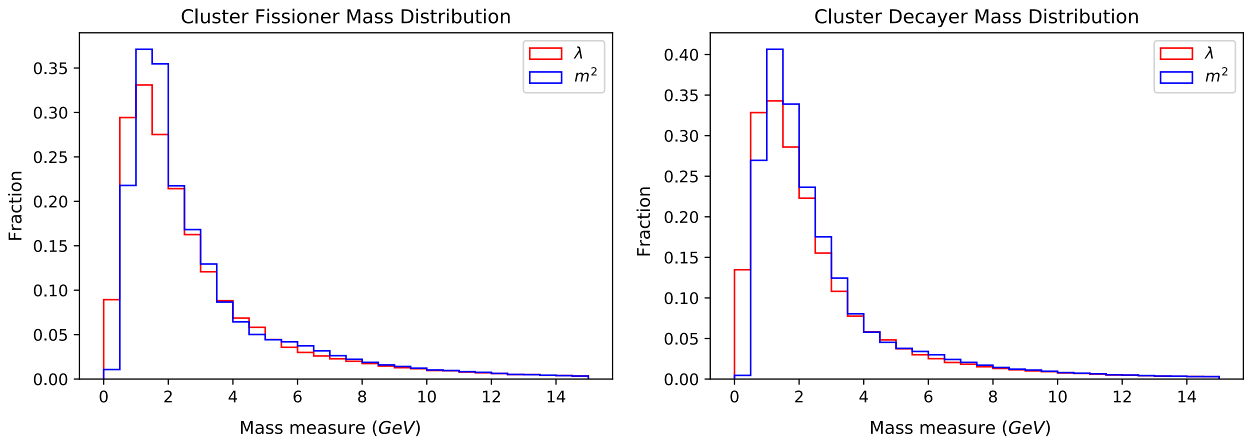

Fig. 8 Comparison of the two different mass measures for the cluster fission and cluster decayer stages respectively for LEP events at 91.2 GeV

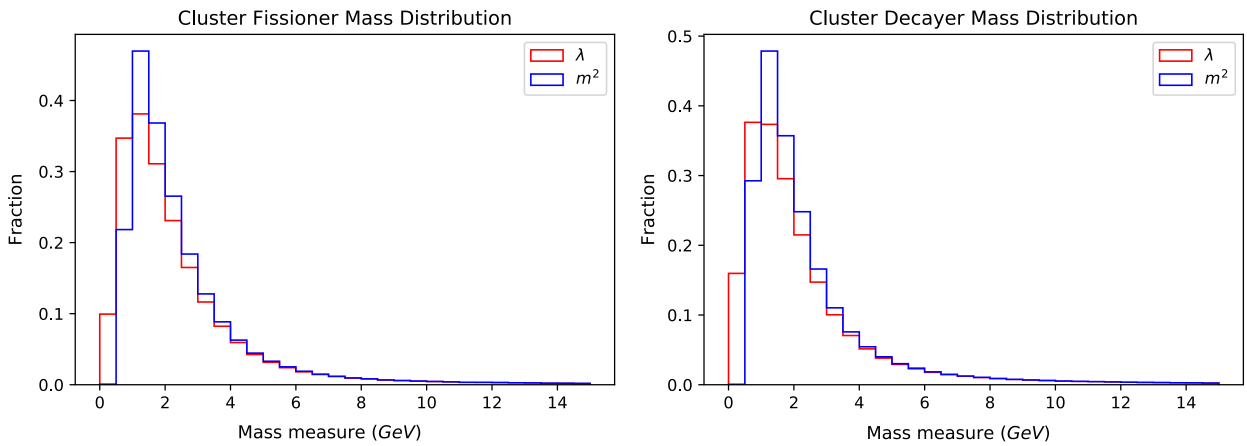

Fig. 9 Comparison of the two different mass measures for the cluster fission and cluster decayer stages respectively for LHC Minimum Bias events at 7 TeV

5 Analysis

We first tune the 3 parameters of our mass-based scaling model to the same identified strange particle yields at LEP and LHC as in Sect. 3. The new tunable parameters are `MassScale` (for gluon splitting), `FissionMassScale`, and `DecayMassScale`, which are defined by Eq. 4. The outcome of the tuning procedure for the relevant parameter values is shown in Tables 3 and 4 for LEP and LHC Minimum Bias, for both the total invariant mass measure and the λ measure.

With the three new characteristic mass scales, we are able to improve the description of all observables considered in the tuning especially for LHC observables as shown in Fig. 10, where we compare the two different mass measures after tuning, as well as the Monash tune [14] for Pythia.

Although the simple tuning recommends different values for the usage at LHC and LEP it is also feasible to use the set of parameters obtained from the tuning to LHC data and still get improved results for LEP observables which was not possible by having a simple flat number as the probability to produce strange quarks as is shown in Fig. 11.

Table 4 Results for the tuned characteristic mass scales m_0, in units of GeV, of our new model using our λ measure (defined in Eq. 5) of a colour-singlet object for LEP and LHC tunes respectively

λ measure	LEP	LHC
Gluon Splitting	72	37
Cluster Fission	4	20
Cluster Decay	16	10

5.1 Discussion

The default version of Herwig did not allow for strange production during the gluon splitting stage. By allowing this process, improvements can be seen in all the considered observables. With our new model, there is a more physically motivated dynamic strangeness production mechanism at all stages of the hadronization.

Eur. Phys. J. C (2019) 79:61 Page 9 of 12 61

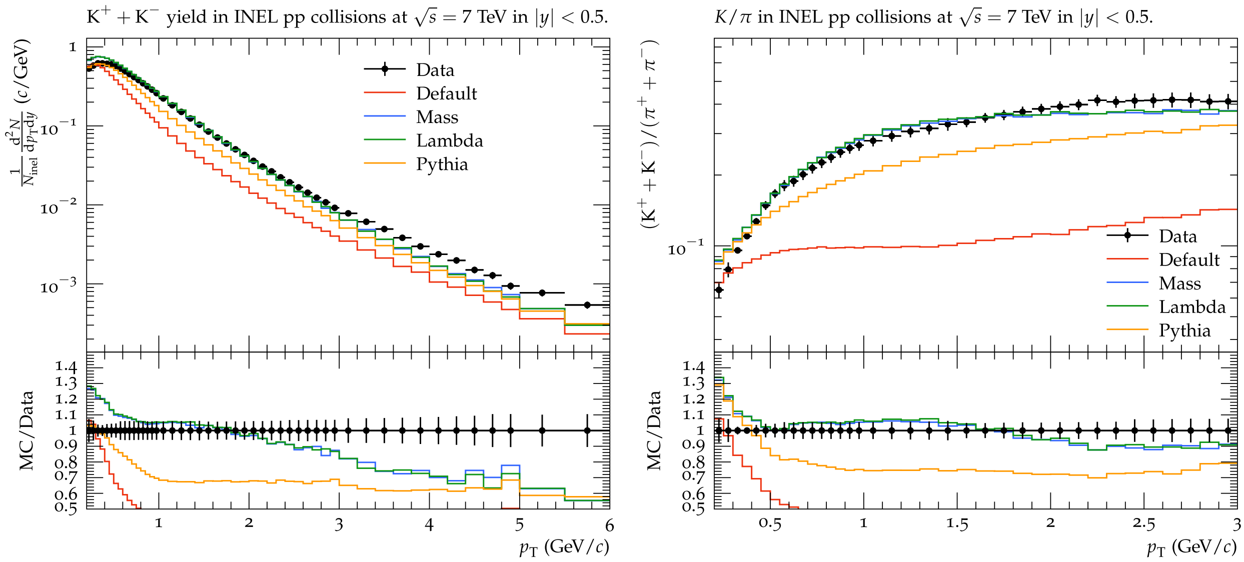

Fig. 10 $K^+ + K^-$ yield and K/π ratio as measured by ALICE [25] at 7 TeV. Shown is a comparison between the default version of Herwig (without baryonic reconnection), i.e. static production of strangeness, the new approach which introduces dynamical strangeness production with the two different measures (Mass and Lambda) and Pythia with the Monash tune

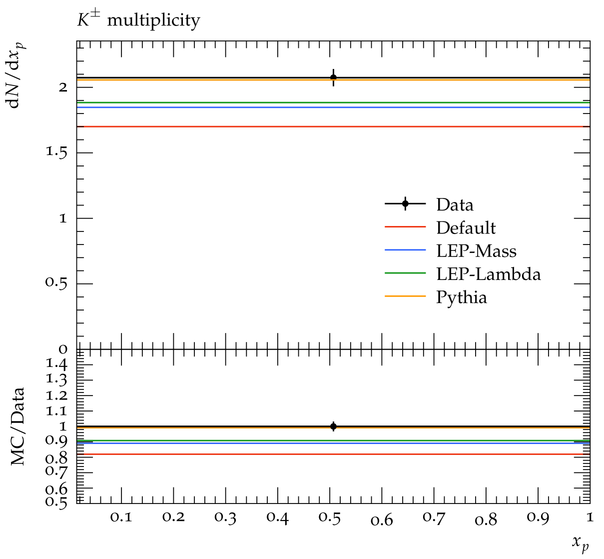

Fig. 11 Measurement of $K^\pm$ multiplicities at SLD [23] $\sqrt{s}$ = 91.2 GeV. We show a comparison between the default Herwig model and the dynamical strangeness production where we used the LHC-tuned parameters (see Tables 3 and 4) and Pythia with the Monash tune

The multiple parton interaction model in Herwig involves two types of subprocesses, hard and soft. Hard processes are allowed to shower and emit quarks and gluons, while soft ones produce only gluons which may not shower. These soft gluons are all colour-connected to each other and the beam remnants, resulting in a single pre-cluster when undergoing non-perturbative gluon splitting. This type of pre-cluster typically has a large invariant mass due to the large number of soft gluons and the isotropic nature of their momentum distribution, resulting in a high strangeness production weight for this subsystem. The resulting produced strange particles coming from these soft interactions are distributed uniformly in rapidity.

There are three key differences between the LEP and LHC environments during hadronization. Firstly, LEP has a much lower energy scale than the LHC, naturally limiting the possible distribution of colour-singlet masses at the stage of non-perturbative gluon splittings. As a result, a direct comparison between LEP and LHC in our model is not straightforward.

Secondly, while LEP and LHC simulations may have very similar cluster mass distributions, the number of clusters is far higher for the latter. Similarly, at the pre-cluster level, LEP prefers colour-singlets that span the entire final state, as shown in Fig. 4, i.e. no perturbative gluon splittings during the parton shower. This results in the majority of events either having enhanced strangeness production or none at all, at the gluon splitting level, meaning that a flat weight at this level in hadronization can be justified for LEP runs.

Finally, and related to the previous two, LEP is a much cleaner environment. For lepton collisions, there are no multiple parton interactions, nor much effect from colour reconnection. However, in proton collisions, these are both vital phases of the simulation that drastically change the mass topology of the event.

Table 5 Expected value of strangeness production weight of our new model in LEP events at 91.2 GeV, comparing the total invariant mass results with the λ measure results

$E(w_s)$ at LEP	Mass	λ
Gluon Splitting	0.096	0.164
Cluster Fission	0.297	0.166
Cluster Decay	0.009	0.016

Table 6 Expected value of strangeness production weight of our new model in LHC Minimum Bias events at 7 TeV, comparing the total invariant mass results with the λ measure results

$E(w_s)$ at LHC	Mass	λ
Gluon Splitting	0.555	0.571
Cluster Fission	0.018	0.020
Cluster Decay	0.153	0.041

Taking the characteristic mass scales from Tables 3 and 4, we have translated these into an effective expected value for the weights for the two mass measures. For LEP events, as shown in Table 5, the total invariant mass approach prefers cluster fissioning, while for the λ measure, non-perturbative gluon splitting and cluster fissioning are approximately the same. It should be noted that aside from the gluon splitting weights, there is no direct translation between the kinematic picture and the old model of strangeness production, but these expected values give an idea of the average weights. For gluon splitting at LEP, the weight simply varies between 0 and the maximal value, since pre-clusters are predominately situated around two peaks, as shown in Fig. 4, and the value shown in Table 5 is simply half the maximal value of 0.192 in the invariant mass case, and 0.328 for the λ measure.

For LHC Minimum Bias events, the expected value for the weights are shown in Table 6. There is very little difference between using the two mass measures at the gluon splitting and cluster fission stages, while cluster decay is significantly suppressed when using the λ measure. The enormous suppression of strangeness production during the later stages of hadronization compared to the gluon splitting is almost certainly a hint that colour reconnection plays a non-trivial role in producing strange hadrons. Our new kinematic model uses a mass-based scaling, but colour reconnection aims to lower the cluster masses to some local minimum, meaning that it is in direct conflict with our considerations. For LEP simulations, colour reconnection has a small effect, while in LHC simulations, colour reconnection is a vital phenomenon. Future work will study the correlations between the role colour reconnection plays and our model, in particular, varying the amount of colour reconnection that takes place in an event, and allowing baryonic clusters to form.

Our studies showed that there is virtually no quantitative difference between using the tuned invariant mass parameters and the tuned λ measure parameters. However, the results in Tables 5 and 6 suggest that the λ measure bridges the divide between the two types of collision better.

We have also compared the results of our new model with Pythia and the Monash tune in Figs. 10 and 11. While the Monash tune aims to describe a number of observables other than the strangeness production rate in Pythia, it is tuned to both LEP and LHC data [14], making it an apt benchmark for this discussion.

We can see that our model performs marginally better than Pythia, and significantly better than default Herwig, when trying to describe the $K^{\pm}$ and drastically better on both counts for the K/π ratio yields, as shown in Fig. 10. However, in the low-$p_{\perp}$ region, both Pythia and our model overestimate the data. When using LHC Minimum Bias tuned parameters for LEP simulations, our model outperforms the default Herwig model, but Pythia describes the data better, as shown in Fig. 11.

We expect that changing non-perturbative strangeness production scaling should not change the overall event-shape observables, such as the Sphericity, and total jet broadening. We have included several of these observables from ALEPH data [20,21] in Fig. 12, to confirm that there are only minor statistical differences between default Herwig 7 and our new scaling when one is concerned with non-species specific observables.

While we have not fully solved the discrepancy between the weights for LEP and LHC strangeness production, we have achieved two results: firstly, we have narrowed the gap between the weights of the two types of collision, and in particular, our model can be used with LHC Minimum Bias tuned parameters to better describe LEP data. Secondly, we have made the first steps to a more sophisticated treatment of hadronization and pair production at the low-energy scale in Herwig.

6 Conclusion and outlook

We have introduced a three-part model that scales the probability for strangeness production during the hadronization phase of event generation in Herwig. The scaling is directly controlled by the mass of the corresponding event colour-singlet subsystem at each step. With this mechanism, we allow for greater fluctuations in the production of strange pairs on an event-by-event basis.

We have studied the mechanism for non-perturbative strangeness production in detail and found that the current flat probability model is irreconcilable with both LEP and LHC data. A hadronization model should be able to have

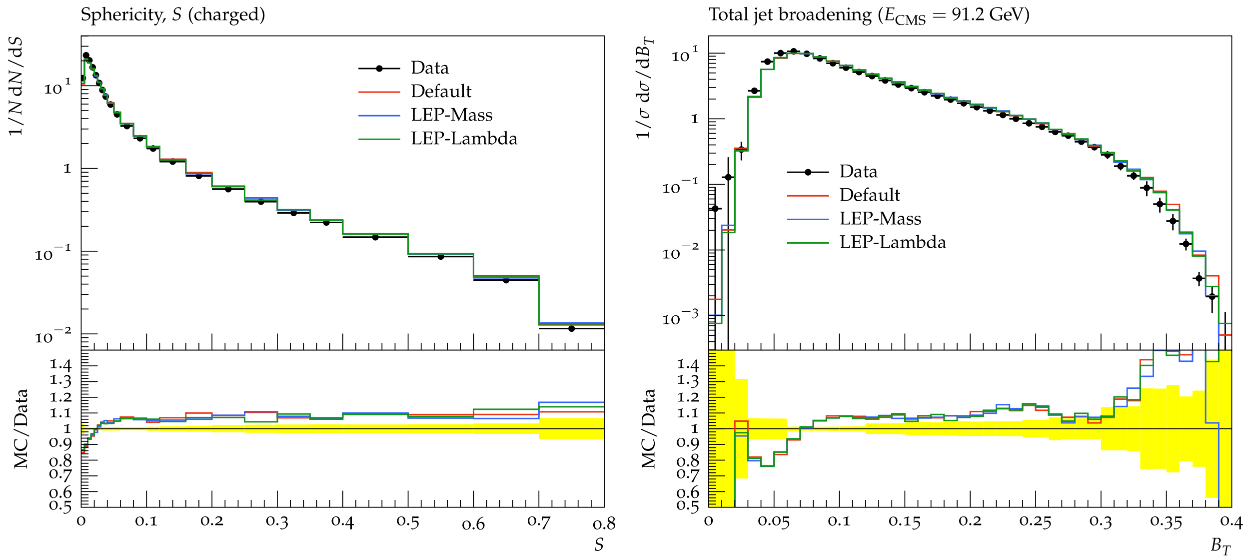

Fig. 12 Event-shape observables from ALEPH [20,21], comparing the results of default Herwig to our new LEP tuned non-perturbative strangeness production scaling, for both mass and λ measures. The new scaling does not impact on event-shape observables

minimal effects on LEP simulations, but produce significant effects for LHC simulations.

After allowing a mass-based scaling, and tuning the parameters to LEP and LHC data, we find that we are able to narrow the gap between the two collider types, and able to describe some observables better than the Lund string model in Pythia with the Monash tune. We also provide expected values for non-perturbative strangeness production, which capture the average values for event-by-event fluctuations.

It should be noted that we have not considered heavier hyperons, the production of which has been shown to be increased by creating baryonic clusters at the colour reconnection stage [8]. Baryonic clusters, which are heavier by nature, would modify our model's strangeness production rates. Understanding the interplay between our new model and colour reconnection will be left for future work.

There is still much left to understand in soft physics, but understanding the correlations created between the various models in hadronization are imperative to having more precise and useful Monte Carlo event generators.

Acknowledgements We would like to thank Stefan Gieseke and Peter Skands for their comments on the manuscript. We would also like to thank Stefan Prestel for his helpful comments on the work and Peter Christiansen for his invaluable help understanding experimental analyses. This work has received funding from the European Union's Horizon 2020 research and innovation programme as part of the Marie Sklodowska-Curie Innovative Training Network MCnetITN3 (grant agreement no. 722104). This work has been supported by the BMBF under Grant number 05H18VKCC1.

Data Availability Statement This manuscript has no associated data or the data will not be deposited. [Authors' comment: The data sets were generated with Herwig 7.1.4, an update to the currently available Herwig 7.1.3. The work presented in this paper will be published in the future release of 7.1.4. However, the code and the data maybe provided on reasonable request from either of the authors.]

References

1. ALICE Collaboration, J. Adam et al. *Nature Phys.***13** 535–539 (2017). arXiv:1606.07424
2. C.M.S. Collaboration, V. Khachatryan, JHEP **05**, 064 (2011). arXiv:1102.4282
3. C. Bierlich, G. Gustafson, L. Lönnblad, A. Tarasov, Tarasov JHEP **03**, 148 (2015). arXiv:1412.6259
4. C. Bierlich, G. Gustafson, L. Lönnblad. arXiv:1612.05132
5. T. Pierog, I. Karpenko, J.M. Katzy, E. Yatsenko, K. Werner. Phys. Rev. C **92**(3), 034906 (2015). arXiv:1306.0121
6. B. Blok, C.D. Jäkel, M. Strikman, U.A. Wiedemann, JHEP **12**, 074 (2017). arXiv:1708.08241
7. J.R. Christiansen, P.Z. Skands, JHEP **08**, 003 (2015). arXiv:1505.01681
8. S. Gieseke, P. Kirchgaeßer, S. Plätzer, Eur. Phys. J. C **78**(2), 99 (2018). arXiv:1710.10906
9. J. Bellm, Eur. Phys. J. C **76**(4), 196 (2016)
10. T. Sjöstrand, S. Ask, J.R. Christiansen, R. Corke, N. Desai, P. Ilten, S. Mrenna, S. Prestel, C.O. Rasmussen, P.Z. Skands, Comput. Phys. Commun. **191**, 159–177 (2015). arXiv:1410.3012
11. T. Gleisberg, S. Hoeche, F. Krauss, M. Schonherr, S. Schumann, F. Siegert, J. Winter, JHEP **02**, 007 (2009). arXiv:0811.4622
12. B. Andersson, G. Gustafson, G. Ingelman, Phys. Rep. **97**(2), 31–145 (1983)

13. N. Fischer, T. Sjöstrand, JHEP **01**, 140 (2017). arXiv:1610.09818
14. P. Skands, S. Carrazza, J. Rojo, Eur. Phys. J. C **74**(8), 3024 (2014). arXiv:1404.5630
15. B. Webber, Nuclear Phys. B **238**(3), 492–528 (1984)
16. D. Amati, G. Veneziano, Phys. Lett. B **83**(1), 87–92 (1979)
17. A. Buckley, H. Hoeth, H. Lacker, H. Schulz, J.E. von Seggern, Eur. Phys. J. C **65**, 331–357 (2010). arXiv:0907.2973
18. A. Buckley, J. Butterworth, L. Lonnblad, D. Grellscheid, H. Hoeth, J. Monk, H. Schulz, F. Siegert, Comput. Phys. Commun. **184**, 2803–2819 (2013). arXiv:1003.0694
19. S. Gieseke, C. Rohr, A. Siodmok, Eur. Phys. J. C **72**, 2225 (2012). arXiv:1206.0041
20. ALEPH Collaboration, R. Barate et al. *Phys. Rept.* **294** 1–165 (1998)
21. The ALEPH Collaboration. Eur. Phys. J. C Particles Fields. **35** 457–486 (2004)
22. DELPHI Collaboration, P. Abreu et al. Z. Phys. C **73** 11–60 (1996)
23. S.L.D. Collaboration, K. Abe et al., Phys. Rev. D **69**, 072003 (2004). arXiv:hep-ex/310017
24. Particle Data Group Collaboration, C. Amsler et al. Phys. Lett. B **667** 1–1340 (2008)
25. ALICE Collaboration, J. Adam et al. Eur. Phys. J. C **75**(5), 226 (2015). arXiv:1504.00024

4.2 Errata for *Kinematic Strangeness Production in Cluster Hadronization*

1. In §2, paragraph three, the statement: *"In Fig. 1, we have omitted colour reconnection since this step simply changes the colour topology of the event, not the content of the clusters."* is misleading. The revised statement should read: *"In Fig. 1, we have omitted colour reconnection since this step simply changes the colour topology of the event, not the* ***quark content of the event.****"* where boldface indicates the change.

2. In §2.1, paragraph two, the sentence: *"After all the gluons in an event have been split, nearest neighbours in momentum space are most likely to be nearest neighbours in colour space [16], and clusters are formed from the momentum-space neighbouring $q\bar{q}$ pairs, with a mass distribution decoupled from the hard scattering process that created them."* has a typographical error. The sentence should read: *"After all the gluons in an event have been split, nearest neighbours in momentum space are most likely to be nearest neighbours in colour space [16], and clusters are formed from the* **colour-space** *neighbouring $q\bar{q}$ pairs, with a mass distribution decoupled from the hard scattering process that created them."* where boldface indicates the change.

3. In Table (1), the second parameter tune values (right most column) are 0.690, and 0.685 for cluster fission and cluster decay respectively. As discussed in the text, the parameters were decoupled, but tuning resulted in similar values.

4. In Figure (11), the labels "LEP-Mass" and "LEP-Lambda" are erroneous. They should read "LHC-Mass" and "LHC-Lambda" since they are the LHC-tuned parameters applied to e^+e^- data.

5. The work compares the new strangeness production model against LHC minimum bias data, and what we call "LEP data". While most e^+e^- plots in the work compare to data from LEP, in Figure (2) left pane, and Figure (11), the work compares of the model to SLD data [238], which was actually an experiment at the SLAC National Accelerator Laboratory. It is more accurate to say "*e^+e^- data*" in the work.

5

Spacetime Coordinates and Hadronization

Multiple parton interactions (MPI) modelling forms a key part of describing proton-proton collisions. Pythia [239] and Sherpa generate MPI ordered in decreasing transverse momentum [17] and extract partons with an on-average decreasing momentum fraction, in such a way that the sum of these fractions never exceeds unity, thereby ensuring energy and momentum conservation. Herwig uses the eikonal model previously implemented in JIMMY [159], which we outline below. A detailed review of the eikonal model can be found in [92].

Generating MPI with perturbative QCD techniques requires knowledge of multi-parton distribution functions, the multi-particle analogues of the parton distribution functions $f_{a/A}$ and $f_{b/B}$ in the factorization theorem of Eq. 2.26. Double- and multi-parton distribution functions have been studied theoretically since the 1970s [80–86, 240–243]. There are, however, very few direct experimental constraints on them, especially beyond the level of double-PDFs. Since proton-proton event generation can involve an arbitrary number of scattering processes, a simple iterative approach can be motivated by noting that the genuine multi-parton correlations tend to be relevant only in small parts of phase space, see e.g. [85, 86] for the case of double-PDFs. The approach used by Herwig is the eikonal model which starts with an ansatz for the average number of partonic interactions in a given event, dependent on the impact parameter b and the centre of mass energy s:

$$\langle n(b,s)\rangle = A(b)\sigma_{\mathrm{hard}}^{\mathrm{inc}}\left(s; p_{\perp}^{\mathrm{min}}\right), \tag{5.1}$$

where $A(b)$ is the so-called overlap function, and $\sigma_{\mathrm{hard}}^{\mathrm{inc}}$ is the inclusive cross section to produce a pair of partons with transverse momentum above the cutoff $p_{\perp}^{\mathrm{min}}$. Since the protons are composite objects with finite size, the overlap function depends on the impact parameter, i.e. the transverse distance between the proton centres, and the effective radius of the proton. In Herwig, the overlap function used is generated by assuming that the matter distribution in transverse space of the proton, $G(b;\mu)$, is of the same form [159] as the electromagnetic form factor for the proton:

$$G(b;\mu) = \int \frac{\mathrm{d}\vec{k}}{(2\pi)^2}\frac{\exp(\vec{k}\cdot\vec{b})}{(1+\vec{k}^2/\mu^2)^2} \tag{5.2}$$

where μ is the inverse proton radius, a free parameter of the model. The overlap function between two protons is then the convolution of two such form factors:

$$A(b;\mu) = \int \mathrm{d}^2b' G(b';\mu)G(b'-b;\mu), \tag{5.3}$$

leading to a Bessel function of the second kind:

$$A(b;\mu) = \frac{\mu^2}{96\pi}(\mu b)^3 K_3(\mu b). \tag{5.4}$$

There are two types of MPI in Herwig, hard and soft, but both follow the same route as described above. The distinction between the two mainly lies in the cross section values, the inverse proton radius which is different between the two types of MPI, and the fact that partons involved in hard scattering processes undergo parton showering, while those in soft scattering processes do not.

Herwig uses the assumption that the MPI are uncorrelated, resulting in a Poissonian distribution for the number of scatters n for a given impact parameter. Once n is generated, Herwig ensures energy and momentum conservation by vetoing any MPI that would violate this. The hard MPI also undergo independent parton showers in Herwig, meaning that there is no interference between these subcollisions during the radiative part of event generation. Colour reconnection, as described in Sec. 3.4, recovers some of the interference physics. While the MPI generation in Herwig has an explicit spacetime dependence on the impact parameter, b, it is integrated over to generate the unitarized cross section for inelastic collisions, meaning that there is no final explicit impact parameter generated for a given event.

Since the overlap function in Eq. 5.4 is formulated in transverse space, one might then ask how the MPI are distributed in this space, and what effects spatial separation might have on the later stages of physical modelling. In order to answer these questions, a framework for generating spacetime coordinates must first be built.

5.1 Spacetime in Event Generators

Monte Carlo event generators are almost universally formulated in the energy-momentum framework, meaning that there is no information, nor indeed any notion at all, of spacetime coordinates and causal separation between particles in an event. Once the event reaches the later stages of the simulation, the physical span of the event has reached distances on the order of several fermis, meaning that an exclusively energy-momentum framework is no longer appropriate. It will not offer realistic information about the distances between partons, nor whether or not they should be allowed to be aware of one another, let alone interact.

As the high-energy and the heavy-ion phenomenology communities begin to study and test one another's frameworks, high-energy event generators are beginning to build in spacetime coordinates, a vital part of modelling in heavy-ions since the collision systems are much larger than those of proton-proton collisions. Recent work has begun to study spacetime coordinates in proton-proton collisions and the distribution of hadrons in an event [244], investigating hadronization-level spacetime coordinates and hadron density. The shoving model [230, 233], implemented in Pythia, Dipsy [226], and Angantyr [225], builds a simple framework for spacetime coordinates to push strings apart during hadronization, using a repulsive force that depends on the transverse-spatial separation between the strings. However, in order to rigorously test high-energy event generators in a heavy-ion setting, we need to build spacetime coordinates into each individual proton-proton scattering to test its validity. From there, one can then embed individual nucleon-nucleon scatters into the larger collision system. This is particularly important for hadronization models developed in the proton-proton collision environment, such as the Lund string and cluster models, since these are all formulated in momentum space.

In the publication presented in Sec. 5.2, we develop a framework for introducing spacetime coordinates during the event simulation. We argue that spacetime coordinates are predominately produced by two stages of the simulation, namely the initial transverse separation due to multiple parton interactions, and the distance propagated by the end of the parton shower. After introducing spacetime coordinates, we then use this new information to help inform and assist the baryonic colour reconnection algorithm [213], as described in Sec. 3.4.2. Comparing our model to data shows reasonable agreement, though diffractive events are still poorly understood and modelled in Herwig. The quantitative success of the spacetime framework encourages future work to embed Herwig's hadronic collision modelling into heavy-ion environments to test the capabilities of the cluster hadronization model.

5.2 Published Material

Spacetime Colour Reconnection in Herwig

Johannes Bellm, **Cody B Duncan**, Stefan Gieseke, Miroslav Myska, and Andrzej Siódmok

Published in The European Physical Journal C 79 no. 12 (2019) 1003

DOI: 10.1140/epjc/s10052-019-7533-6

e-Print: arXiv:1909.08850 [hep-ph]

CoEPP-MN-19-04, MCNET-19-21, KA-TP-08-2019, HERWIG-2019-01, LU-TP 19-41

Paper begins overleaf

Eur. Phys. J. C (2019) 79:1003
https://doi.org/10.1140/epjc/s10052-019-7533-6

THE EUROPEAN PHYSICAL JOURNAL C

Regular Article - Theoretical Physics

Spacetime colour reconnection in Herwig 7

Johannes Bellm[1], **Cody B Duncan**[2,3,a], **Stefan Gieseke**[3], **Miroslav Myska**[4], **Andrzej Siódmok**[4,5]

[1] Theoretical Particle Physics, Department of Astronomy and Theoretical Physics, Lund University, Lund, Sweden
[2] School of Physics and Astronomy, Monash University, Clayton, VIC 3800, Australia
[3] Institute for Theoretical Physics, Karlsruhe Institute of Technology, 76128 Karlsruhe, Germany
[4] Czech Technical University in Prague, Brehova 7, 115 19 Prague, Czech Republic
[5] The Henryk Niewodniczanski Institute of Nuclear Physics, Kraków, Poland

Received: 29 September 2019 / Accepted: 2 December 2019

Abstract We present a model for generating spacetime coordinates in the Monte Carlo event generator Herwig 7, and perform colour reconnection by minimizing a boost-invariant distance measure of the system. We compare the model to a series of soft physics observables. We find reasonable agreement with the data, suggesting that pp-collider colour reconnection may be able to be applied in larger systems.

1 Introduction

As the LHC reaches unprecedented levels of precision and data collection, the playground for studying QCD effects has increased manifold. In particular, Monte Carlo event generators [1–5] provide an ideal arena for testing novel ideas in the low-energy regime, i.e. the mechanisms of hadronization, where non-perturbative effects have to be phenomenologically modelled, and the underlying event. One aspect of proton-proton collisions that is poorly understood is exactly how multiple parton-parton interactions from the initial scattering process interfere and interact with one another during the hadronization stage.

Multiple parton interactions were first introduced in [6], and implemented in Pythia [4], where its importance in hadronic collisions was highlighted beyond a doubt. A similar physical notion was introduced in [7] and later implemented in Herwig++ [1,8,9], with some recent improvements to soft and diffractive scatterings in [2,10] to Herwig 7.

One such model of this interference between subcollisions in an event is colour reconnection [11–15], whereby a Monte Carlo event generator reduces some kinematic, momentum-based measure of the event. The physical intuition for such a mechanism is twofold: to correct for errors in the leading-colour approximation of the parton shower, and to allow multiple parton interactions, which may have been colour-connected, to have cross-talk. A summary of the history of colour reconnection and the effects of such a mechanism on precise measurements is given in [16]. Colour reconnection in Herwig 7 first focused on reconnecting excited $q\bar{q}$ pairs called clusters, minimizing the sum of the invariant masses. Later work [14] expanded upon this model to introduce the possibility of forming so-called baryonic clusters qqq and $\bar{q}\bar{q}\bar{q}$ from three ordinary/mesonic clusters. Other methods have investigated colour reconnection at the perturbative stages of event simulation or taken inspiration from perturbative techniques [17–19].

Most pp event generators are developed in the energy-momentum framework for the various stages of event simulation, meaning that none of the physics modelled involves any notion of spacetime separation. While the energy-momentum framework has been very successful, there are still several issues at hand. In particular, it does not have an adequate answer to what parts of the event are allowed to undergo colour reconnection within a given slice of phase space, if one thinks that colour reconnection needs to be a causal effect. Collisions of heavy ions have shown that spacetime structure is important in modelling where interactions start, since a jet starting at the edge of the quark-gluon plasma will lose far less energy to one travelling through the centre of dense medium, a phenomenon known as jet quenching [20–22]. As a result, pp-oriented event generators have also started to include more spacetime information, using these coordinates for various aspects of the simulation, such as collective hadronization effects [23,24], and a spacetime evolution of the parton shower [25]. Pythia recently introduced a framework for generating spacetime coordinates [26] for quantitative studies of Lund string fragmentation [27]. The effects of introducing spacetime coordinates have been recently studied in dipole evolution in $\gamma^* A$ collisions [28].

[a] e-mail: cody.duncan@monash.edu

Published online: 12 December 2019

As high energy and heavy ion phenomenology begin to have more interaction with each other, an immediate question one should ask is if the models developed in each field can be applied to the other successfully. Without spacetime information, high energy event generators cannot hope to be able to describe hadronization of large systems well. This work aims to be the first steps of introducing spacetime coordinates and using them to aid the baryonic colour reconnection model [14]. We intend this to be a proof of concept that will allow us to apply this hadronization model to heavy ions in later work.

The format of the article is as follows: we start by recalling elements of modelling high energy collisions, such as the underlying event, cluster hadronization, and colour reconnection models in Herwig 7, in Sect. 2. In Sect. 3, we describe our method of systematically assigning coordinates to the multiple parton interactions and the partons at the end of the shower. We then present our model of using this spacetime information to perform colour reconnection in Sect. 4. We briefly describe additional modifications that have been applied in the making of this and related works in Sect. 5. We tune our new model in Sect. 6 and present the results of the procedure in Sect. 7. Lastly, with Sect. 8, we summarize our model and future work.

2 Event simulation in Herwig 7

We briefly summarize the pertinent points of modelling the underlying event and hadronization in Herwig 7.

2.1 Multiple parton interactions (MPI)

Since the proton is a composite particle, when two protons collide, there may be several parton-parton interactions, which fall into two classes in Herwig 7: hard and soft. Partons from hard scatters undergo parton showering, while soft scatters do not.

For a given event, Herwig 7 generates a number of each type of these scatters. The average number of interactions for a given impact parameter b and centre of mass energy s is schematically given by:

$$\langle n_{\text{int}}\rangle = A(b;\mu)\sigma^{\text{inc}}(s; p_{\perp}^{\text{min}}), \tag{1}$$

where σ^{inc} is the inclusive cross section to produce a pair of partons above a defined minimum transverse momentum, $A(b;\mu)$ is the overlap function between the two protons, and μ^2 is commonly referred to as the inverse hadron length. In Herwig 7, both the hard and soft MPI scatters have the same form for Eq. 1, and indeed it is assumed that they both have the same functional form for the overlap function, but with different values for μ^2. Similarly, the inclusive cross sections are different values for hard and soft scatters.

Herwig 7 assumes the MPI to be independent of one another (including energy-momentum conservation), leading to a Poissonian probability distribution. Using the notation of [3], we can write the joint probability distribution to produce h hard and k soft scatters at a given b[1] as:

$$\mathcal{P}_{h,k}(b) = \frac{(2\chi_h)^h}{h!}\frac{(2\chi_k)^k}{k!}e^{-2(\chi_h+\chi_k)}, \tag{2}$$

where $2\chi_{h,k} = A(b;\mu_{h,k})\sigma^{\text{inc}}_{h,k}$ is the so-called eikonal factor. This formalism was developed in [29] and Herwig's implementation is built on the JIMMY framework [7].

Equation 2 is then integrated over b space to produce an exact probability to produce the corresponding number of hard and soft scatters in an event:

$$P_{h,k} = \frac{\int \mathrm{d}^2 b \mathcal{P}_{h,k}(b,s)}{\int \mathrm{d}^2 b \sum_{h\geq 1,k=0}^{\infty} \mathcal{P}_{h,k}(b,s)}. \tag{3}$$

Herwig 7 samples the distribution in Eq. 3 probabilistically, to obtain a number h of hard scatters, and k of soft scatters. The primary hard subprocess in Minimum Bias event generation in Herwig 7 is an interaction between two valence (antiquarks) [12], while subsequent MPI collisions are initiated by regular $2 \to 2$ QCD processes. The incoming legs are evolved backwards to pairs of gluons extracted from the beam remnant, with the colour topology defined in the $N_C \to \infty$ limit. The colour topology is motivated by the leading-colour approximation used in the shower, though as discussed in [12], this is a phenomenological choice rather than an approximation.

As Herwig 7 produces each scatter, it checks the available energy and momentum in the protons. If the protons cannot produce another scatter, the MPI production algorithm terminates. As a result, Herwig 7 typically generates a subset of the total number of scatters sampled from Eq. 3. More details of the technicalities involved in the implementation of MPI algorithm can be found in [1].

2.2 Cluster model

Partons from a scattering process are showered down to the parton shower cutoff scale, and the resulting colour topology has triplets connected to anti-triplets via gluon connections. At the hadronization scale and below, Herwig 7 uses the cluster hadronization model [30], based on the pre-confinement property of angular-ordered showers [31].

The first step in the cluster model is to non-perturbatively split the gluons into quark-antiquark pairs. To split the gluons, Herwig 7 uses a kinematic map at the end of the shower to put the gluons on-constituent-mass-shell and performs an

[1] We have suppressed the functional dependence on centre of mass energy s.

isotropic decay. The constituent-mass of the gluon is a non-perturbative parameter of Herwig 7 hadronization model.

Nearest quark-antiquark neighbours in colour space, which are typically nearest neighbours in momentum space due to pre-confinement, are then collected into colourless, excited quark-antiquark pairs, i.e. clusters. From there, the clusters undergo colour reconnection.

2.3 Colour reconnection

Clusters typically connect partons from the same multiple parton interaction scattering. Colour reconnection alters the colour topology of the event, and allows the different MPI to interact with one another at the hadronization level.

As mentioned in Sect. 2.1, Herwig 7 chooses the leading-colour topology for the additional scatters, thus they are colour-connected to the beam remnant and other subprocesses. As noted in [12], colour reconnection is a required part of hadronization modelling in hadron collisions since the leading-colour approximation performs significantly worse in non-perturbative parts of the event generation.

Colour reconnection aims to minimize a given measure of the event, typically momentum-based. Herwig 7 has a variety of colour reconnection algorithms [12,14], namely:

- Plain,
- Statistical/metropolis,
- Baryonic.

The plain colour reconnection model locally minimizes pairwise cluster invariant masses:

$$m_{q\bar{q}}^2 = \left(p_q + p_{\bar{q}}\right)^2 . \qquad (4)$$

The criteria for two clusters to undergo colour reconnection and swap partners is:

$$m_{q\bar{q}'} + m_{q'\bar{q}} < m_{q\bar{q}} + m_{q'\bar{q}'} . \qquad (5)$$

If a pairing reduces the invariant mass, it is allowed to reconnect with a flat probabilistic weight, typically tuned to LHC data, while ensuring that the model doesn't adversely affect LEP simulations. Baryonic colour reconnection was recently implemented in Herwig 7 [14], and it uses a more sophisticated algorithm. For each cluster in the event, the algorithm searches for other clusters which occupy the same neighbourhood in rapidity-space. It searches for two types of candidate clusters for reconnection: baryonic, and (ordinary) mesonic.

In the baryonic case, given a cluster A, transform the momenta of all other clusters to the rest frame of A, and search for two other clusters that have the same orientation of quark axis in rapidity space. It then chooses the pair of candidate clusters which have the largest rapidity span in this frame. If the reconnection is accepted, the quarks are then collected into a three-component cluster, called a baryonic cluster, and similarly the antiquarks are collected into an anti-baryonic cluster.

In the mesonic case, if the candidate cluster B with the largest rapidity span has a quark axis oriented in the opposite direction to cluster A, reconnect $q_A \bar{q}_B$ and $q_B \bar{q}_A$, in much the same manner as the plain colour reconnection model. For both types of cases in baryonic colour reconnection, the probabilities for reconnection are given by two different flat weights, $p_{\mathrm{M,reco}}$ and $p_{\mathrm{B,reco}}$.

While the statistical colour reconnection model is outside the scope of this paper, we mention that it aims to minimize mass, much like the plain model, but it allows reconnection to increase the mass of the system with a suppressed probability, and is based on the simulated annealing optimization algorithm [32].

In all cases, colour reconnection qualitatively aligns colours between partons that move into the same direction such that the multiplicity of particles produced in between them is reduced and the produced particles carry more momentum on average.

3 Spacetime coordinate generation

We present the two parts of how our model systematically generates coordinates for the multiple parton interaction scattering centres and the hadronization stage. We argue that these are the two stages of event generation that are most impactful on spacetime coordinates.

3.1 MPI coordinate generation algorithm

To obtain an intelligent and relevant value for the impact parameter, the MPI coordinate generator takes the produced values for h, k in Eq. 3 and stochastically samples the distribution of Eq. 2, vis-a-vis a veto algorithm. Thus, the produced b, when the number of events tends to infinity, will be the correct distribution for a given set of h and k.

As shown in Fig. 1, the joint Poissonian behaves as we expect. The more scatters that Herwig 7 produces, the more likely it is that the sampled b will be central, while having more soft scatters for a fixed number of total scatters makes the distribution have a broader tail. In this work we will be using the Bessel proton profile, meaning that the overlap function is a Bessel function of the third kind:

$$A(b;\mu) = \frac{\mu^2}{96\pi}(\mu b)^3 K_3(\mu b). \qquad (6)$$

It should be noted that the results of the sampling should not be surprising. At large numbers of interactions, the sampled impact parameters tend to be closer to 0, since a larger than average number of interactions requires a more central

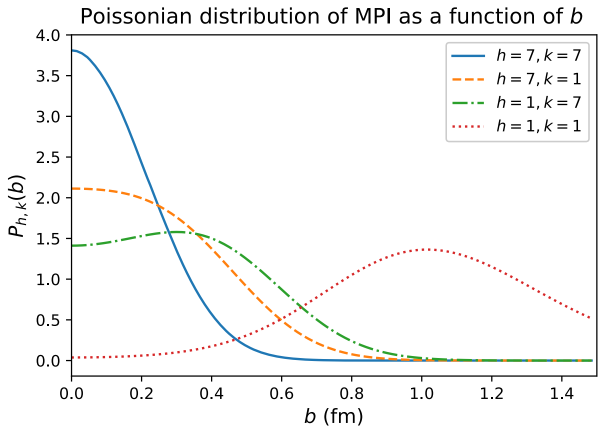

Fig. 1 Joint Poissonian distribution $\mathcal{P}_{h,k}(b)$, as a function of impact parameter b, for a number of h hard scatters and k soft scatters. We have picked one large (7) and one small (1) value, and show the various combinations. The more collisions that occur, the more likely the collision is to be central. Keeping the number of interactions fixed but having more soft interactions makes the distribution have a broader tail. We have used the following fixed values for the normalized distributions: $\sigma^{\text{inc}}_{\text{hard}} = 83$ mb, $\sigma^{\text{inc}}_{\text{soft}} = 127$ mb, $\mu^2_{\text{hard}} = 0.71$ GeV^2, and $\mu^2_{\text{soft}} = 0.52$ GeV^2. These distributions are normalized independently to unit area

collision. Once b is determined for a given event, we set the incoming beam positions to be at $(\pm b/2, 0, 0, 0)$, i.e. aligned along the x-axis, for simplicity.

The overlap function $A(b; \mu)$ in Eq. 6 is generated by the convolution of the two protons' form factors, $G(b; \mu)$:

$$A(b) = \int \mathrm{d}^2 b' G(b') G(b - b'), \tag{7}$$

where we have suppressed the dependence on μ for clarity. The overlap function governs the density of MPI scattering centres in the transverse plane for a given offset between the protons.

To obtain the MPI centre positions, we sample the integrand of Eq. 7. We generate h hard scatters, and k soft scatters, using two different μ^2 values for the hard and soft interactions. As a result, hard scatters are slightly more concentrated in the centre of the transverse plane, while soft scatters have a longer tail.

Once these points have been generated, all coordinates including the proton positions get the same random global rotation in the transverse plane. The beam remnants receive the sampled proton positions. A schematic diagram of the results of the MPI coordinate generation algorithm is shown in Fig. 2. The overlap need not necessarily be a Bessel function, and we have included the results of the MPI coordinate generation for a uniform proton profile in Fig. 2. For this type of proton profile, MPI centres can only be situated in the overlap. However, for the rest of the paper, we will work with the Bessel function profile.

3.2 Tracing spacetime during parton showers

The spacetime structure of the parton-shower evolution was already considered in the early paper on QCD cascades by Fox and Wolfram (see Fig. 1 of [33]). Later the spacetime evolution of the parton shower was introduced, for example, to study jets in hadronic e^+e^- events at LEP [34] and in deep-inelastic ep scattering [35]. Very recently in a publication on the space–time structure of hadronization in the Lund Model [26] the authors mention that a sensible spacetime picture of parton-shower evolution would introduce some spacetime offsets to their model. However, the authors assumed that the offsets are most likely small in their case and therefore neglected them in their studies.

In the following section, we will investigate in more detail how the parton shower affects the spacetime structure of an event as implemented in the family of Herwig 7 generators. Referring to [36, Section 3.8] for details, we briefly recall the essential concepts of the Herwig 7 spacetime model. It should be noted that there are two major parton shower options in Herwig, namely the angular-ordered shower [37] and the dipole shower [38]. For this work, we will focus on the angular-ordered shower, and its use of virtuality as an evolution variable.

The mean lifetime τ of a parton in its own rest frame, during the parton shower evolution, is calculated in a similar manner as for particles decays, i.e. taking into account its natural width Γ and virtuality q^2:

$$\tau(q^2) = \frac{\hbar\sqrt{q^2}}{\sqrt{\left(q^2 - M^2\right)^2 + \left(\frac{\Gamma q^2}{M}\right)^2}}. \tag{8}$$

Equation 8 interpolates between the lifetime for an on-mass shell parton $\tau(q^2 = M^2) = \hbar/\Gamma$, and for a highly virtual (i.e. off-mass shell) parton $\tau(q^2 \gg M^2) = \hbar/\sqrt{q^2}$. We note that the mean lifetime in Eq. 8 is equivalent to the standard notion of formation time used in heavy ion phenomenology as well as in general jet quenching research [39–42]. We show the equivalence in Appendix.[2]

Once a lifetime is calculated according to Eq. 8, the parton decays according to an exponential decay law, with a rest-frame decay time t^*:

$$P_{\text{decay}}(t < t^*) = 1 - \exp\left(-\frac{t^*}{\tau}\right). \tag{9}$$

After sampling a rest-frame decay time, this time can be converted to the lab-frame decay time t, and a distance travelled in the lab-frame, $\mathbf{d}$:

$$t = \gamma t^*, \quad \mathbf{d} = \boldsymbol{\beta}\gamma t^*, \tag{10}$$

[2] The authors are grateful for Gavin Salam's notes on the notion of formation time for massless soft and collinear gluons.

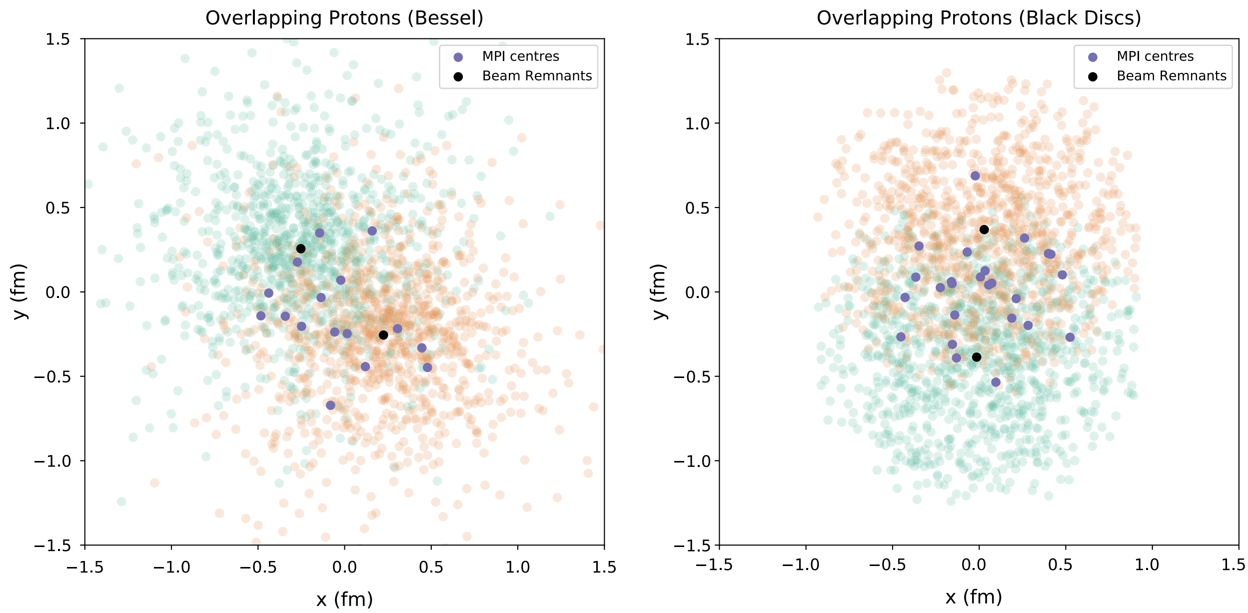

Fig. 2 Result of MPI Coordinate Generator algorithm with the Bessel proton profile (left), and an example for a uniform (black disc) proton profile (right). Green and orange points are partons sampled in a given proton, mauve points are accepted MPI collision centres, and black are the beam remnants

where γ and $\boldsymbol{\beta}$ are the usual Lorentz factors.

Very light quarks and gluons with a small natural width may travel unphysically large distances according to Eq. 8 in the final steps of the parton shower. Similarly, there are issues with assigning particles with no well-defined width spacetime coordinates in the above manner. In order to counter this issue, a minimum width $\Gamma = \nu^2/M$ is introduced, where ν^2 (GeV^2) is a free parameter of the order of lower limit of parton's virtuality. This is essentially the spacetime equivalent of a shower $Q^2 \approx \Lambda^2_{\mathrm{QCD}}$ cutoff scale. The daughters of the parton splitting are then given the starting coordinates defined by Eq. 10. We note that the above considerations are, in our model, a phenomenological model of the spacetime structure of an event, which arise during the initial collision of the protons, and the subsequent perturbative evolution of the event.

In order to study the size of the parton-shower spacetime effects, we will first consider the distance that each parton propagates during the shower. The distance that we are interested in is the difference between a given parton's production and decay vertex, L:

$$L = \sqrt{\left(d_{\mathrm{decay}} - d_{\mathrm{prod}}\right)^2}, \tag{11}$$

where $d \equiv d^{\mu} = (t, x, y, z)$ is the position of a parton relative to the centre of the collision, i.e. the origin. However, since the MPI smearing discussed in the previous section affects only the transverse plane we will also consider transverse distance, constructed from the transverse components of the above vertices, $r = \sqrt{\Delta x^2 + \Delta y^2}$.

In Fig. 3 we show the Lorentz-invariant distance L (left panel) and transverse distance (right panel) traveled by the gluons at the last step of the parton shower evolution for three different processes: minimum bias, Drell–Yan and Higgs-boson production at the LHC at the collision energy 7 TeV. The simulation was performed using default version of Herwig 7 with three different values of ν^2: 1, 2 and 5 GeV^2. We see that most of the partons reach fermi-scale distances which are comparable to the size of the MPI coordinate generation, as shown in Fig. 2. Therefore, it is important to take the parton shower effects into account. We also see that in soft Minimum Bias processes the partons travel shorter distances, as expected since there is less parton-shower activity in these types of events than in the two other processes. Finally we see that the results, and especially the long distance tails of the distributions, are strongly dependent on the scale ν^2. This indicates that the furthest distances are traveled by partons in the final step of the evolution.

This is also visible in Fig. 4 where we show the spacetime structure of a parton shower of a sample Minimum Bias event, with $\nu^2 = 1\ \mathrm{GeV}^2$, neglecting the spacetime structure of the MPI positions. The final step distances are denoted by red dotted lines, while the intermediate steps are black solid lines. In order to quantify this effect in Fig. 5 we show the ratio of distance traveled by partons in the last step of their evolution to the total distance (distance traveled during the entire evolution).

We see that in the case of both minimum bias and Drell–Yan processes for ν^2 values similar to a typical parton-shower

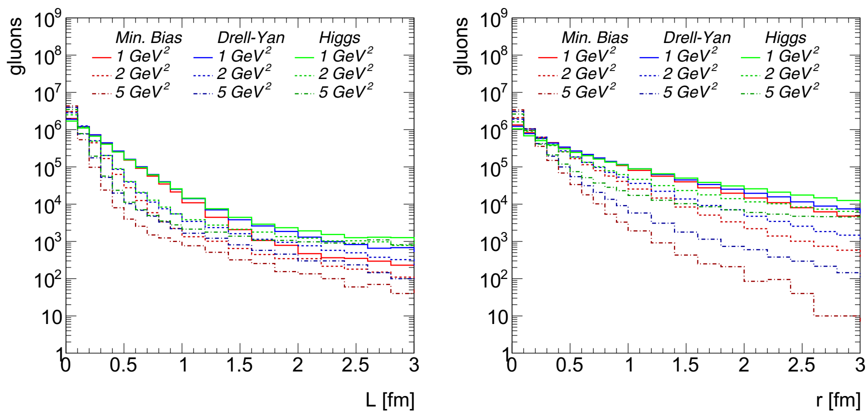

Fig. 3 The total Lorentz-invariant distance L (left panel) and transverse distance r (right panel) traveled by the gluons at the last step of the parton shower evolution for three different processes: minimum bias, Drell–Yan and Higgs-boson production at the LHC at the centre-of-mass energy 7 TeV. The simulation was performed using default version of Herwig 7 using three different values of ν^2: 1, 2 and 5 GeV^2

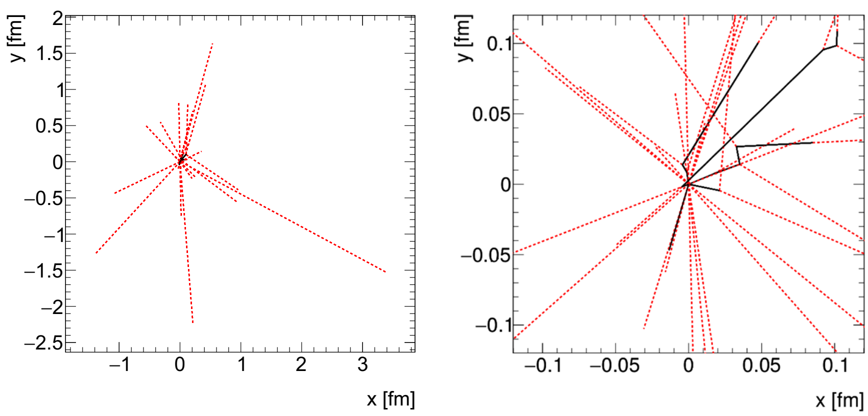

Fig. 4 An example of a parton shower spacetime structure (i.e. neglecting spacetime structure of MPI) of a Minimum Bias event in the transverse plane generated with the minimum virtuality $\nu^2 = 1$ GeV^2. The red dotted lines represent the evolution of the last particle in the parton shower while the rest of the evolution is denoted by the black lines. Both panels show the same event with the right panel magnifying the center of the event

cutoff scale, i.e. below 2 GeV^2, 90% of the total distance is indeed due to the final step of the parton shower. In the case of the Higgs boson production, the distributions look very different. It is because in the simulation we took into account the decay lifetime of the Higgs boson, however when we neglect it, the distributions look very similar to the two other processes.

To summarize, we can expect the fermi-scale parton shower and even further intermediate particle decay distances. As such, these effects have to be included in spacetime colour reconnection model. We also showed that tracing out the microscopic detail of the parton shower spacetime evolution is somewhat unnecessary, since only the low-energy scale of emissions (final steps) have any major impact on the spacetime position of partons, i.e. soft emissions close to the hadronization scale. Finally, it is important to stress that the Heisenberg uncertainty relations impose limits on how much simultaneous energy-momentum and spacetime information one can have on an individual parton.

These results should not be considered as physical, but give us a benchmark of roughly what part of the event simulation drives the creation of large separations in distance between partons.

Instead, we propose a simpler model that assigns coordinates only to the very last partons of the parton shower, just before the hadronization. This is in line with the uncertainty principle as the smearing is only visible for particles at a very soft scale. We may understand the partons' positions then as being smeared out around the scattering centres. This idea represents us taking the semi-classical limit of the parton shower, and generating coordinates in a similarly semi-classical manner.

3.3 Parton shower coordinates

As the partons propagate during the shower, we may assign a spacetime propagation to their motion, but as we have shown above, these distances are only significant at energy levels close to the hadronization scale. As a consequence, we will only give spacetime coordinates to the partons that remain at the end of the shower. In our model of spacetime coordinates, we will not consider z, t coordinates and keep our discussion to the transverse plane. We note that we have chosen the centre of mass frame in order to construct our model, and to extend this to any given frame, one need only transform the

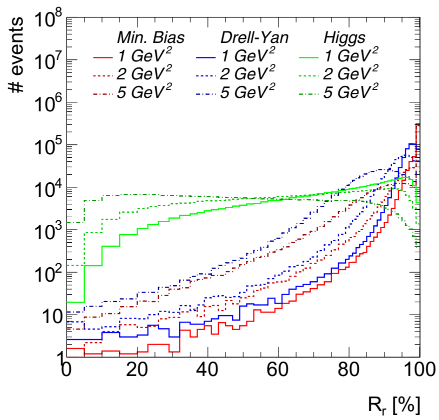

Fig. 5 The ratio of the distance traveled by partons in the last step of evolution to the total distance (distance traveled during entire evolution)

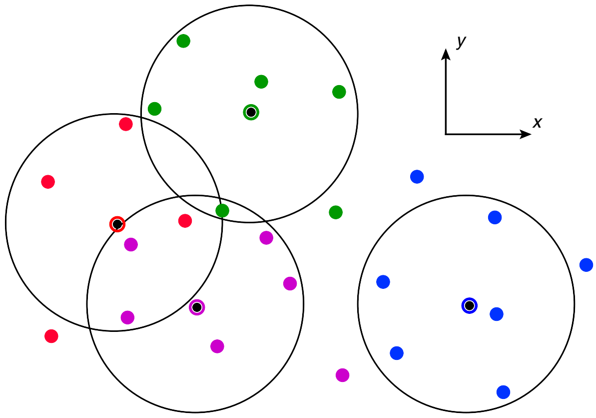

Fig. 6 A schematic diagram for how our model introduces transverse spacetime coordinates for the multiple parton interactions (black points), and for the end of the parton shower. Different coloured points are partons from different, respectively ring-coloured MPI centres. The thin black circles represent a characteristic scale for parton propagation about the MPI centre

variables correspondingly. All considerations below will be invariant to any boosts along the z-axis.

Before the clusters are formed, each surviving parton from a given MPI scattering centre receives an extra transverse propagation distance from the scattering centre coordinates. Instead of tracing out the positional history of each parton during the shower, we take all partons at the end of the shower and propagate them according to Eq. 9. As argued above, this resembles a smearing of each partons' coordinate around the scattering centre within its intrinsic uncertainty.

As discussed in Sect. 3.2, at the end of the perturbative shower, partons will have very small virtualities, meaning that using the precise form of Eq. 8 performs poorly. We instead approximate the mean lifetime by considering the width term in the denominator. Each parton of species p will automatically receive a minimum virtuality, ν^2, for their mean lifetime in their rest-frame:

$$\tau_{0,p} = \frac{\hbar m_p}{\nu^2}. \tag{12}$$

This mean lifetime is derived from Eq. 8, by taking the on-mass shell limit $-\tau(q^2 = M^2) = \hbar/\Gamma$ and using the following form for the width of the on-mass shell partons:

$$\Gamma = \frac{\nu^2}{m_p}. \tag{13}$$

With the mean lifetime from Eq. 12, we proceed as explained in Sect. 3.2, using Eqs. 9 and 10 to set each parton's position relative to the MPI scattering centre that they originated from, adding only the transverse coordinates of the propagation distance.

Equation 12 corresponds to a lab-frame mean lifetime of:

$$\tau'_{0,p} = \gamma\tau_{0,p} = \frac{\hbar E_p}{\nu^2}, \tag{14}$$

where E_p is the lab-frame energy of the given parton. The main motivation for the mass dependence of the mean lifetime in Eq. (12) is that the decay distance of external light quarks is proportional to their energy (and independent of their mass) which is in agreement with expectations from the linear confining potential of QCD, see e.g. [43] and references therein, as well as other hadronization models such as the Lund string model [27].

As a result of this construction, quark-antiquark pairs produced during the non-perturbative gluon splitting will receive the same spacetime position. One may believe this leads to issues where colour reconnection wants to pair these partons together, but Herwig 7 does not allow them to since they would be in a colour-octet state [12,44]. These partons will also have slightly different rapidities, due to kinematics from the gluon splitting.

Once all the partons have their new coordinates with respect to their MPI scattering centre, we then shift these coordinates using the points produced from the MPI coordinate generator, as shown schematically in Fig. 6. The black points are the MPI centres, and partons from those systems are spread by Eq. 10, around their respective centre. Different coloured partons refer to partons originating from different MPI systems.

4 Spacetime colour reconnection

With the transverse coordinates in place, we use this information to perform and inform colour reconnection. We present the outline for plain spacetime colour reconnection model, but we will use the baryonic spacetime model for tuning and in the discussion in the rest of the paper.

4.1 Plain spacetime colour reconnection

As mentioned in Sect. 2.3, the measure for allowing plain colour reconnection is the sum of invariant cluster masses before and after, and the reconnection is given by a flat tuned weight. However, there is at least one major issue with this construction: this measure aims to reconnect cluster constituents so that they are closer in momentum space, but without any input from spacetime which would perhaps prohibit a causally-disconnected colour reconnection.

Using the coordinates we have introduced in Sect. 3, we now define the following spacetime-inspired measure for a single cluster with constituents i, j:

$$R_{ij}^2 = \frac{\Delta r_{ij}^2}{d_0^2} + \Delta y_{ij}^2, \tag{15}$$

where d_0 is the characteristic length scale for colour reconnection in our spacetime model, which is a tunable parameter. $\Delta r_{ij}^2 = (\mathbf{x}_{\perp,i} - \mathbf{x}_{\perp,j})^2$ is the transverse spacetime separation squared between the constituent quarks. We include rapidity differences in Eq. 15. This is inspired by conventional jet algorithms, where we replace the azimuthal separation $\Delta\phi_{ij}^2$ with transverse separation. The parameter d_0 effectively acts as a measure to increase the importance of transverse to longitudinal components. The measure in Eq. 15 captures the transverse separation between the constituents and their longitudinal separation.

Using the measure from Eq. 15, we proceed in the same fashion as Eq. 5, by minimizing the sum of the pairing of cluster constituents. For a given cluster, we pick the candidate cluster that minimizes the measure the most. If the sum of the cluster separations is smaller after a possible reconnection:

$$R_{q\bar{q}'} + R_{q'\bar{q}} < R_{q\bar{q}} + R_{q'\bar{q}'}, \tag{16}$$

then we accept the reconnection with a flat probability, $p_{\mathrm{M,reco}}$. A similar model was studied earlier in [45].

4.2 Baryonic spacetime colour reconnection

Baryonic spacetime colour reconnection uses the algorithm from [14], and outlined in Sect. 2.3. The partners for mesonic and baryonic colour reconnection are found by using the projection onto a given cluster's quark axis.

If instead we find a baryonic reconnection, we cannot directly compare the sum of Eq. 15 for the constituents of the clusters before and after colour reconnection, since we would be starting with 3 clusters – each with 2 partons – and ending with 2 clusters with 3 partons, and the distance measure is an ill-defined quantity in the latter situation.

In the ordinary baryonic colour reconnection algorithm, 3-component clusters, once formed, are reduced to a quark-diquark system, where the diquark system is chosen as the pair of quarks with the lowest total invariant mass. In keeping with our spacetime paradigm, we choose the pair as the closest in spacetime. Given 3 mesonic clusters, we look at the set of triplets $\{q_1, q_2, q_3\}$ and select the pair that are closest – calculated via Eq. 15, and similarly for the set of antitriplets. We choose these partons to become a diquark system, with their constituents' mean spacetime position and rapidity.

We allow baryonic reconnection if the following criterion is true:

$$R_{q,qq} + R_{\bar{q},\bar{q}\bar{q}} < R_{q,\bar{q}} + R_{qq,\bar{q}\bar{q}}, \tag{17}$$

which is analogous to Eq. 16, and we accept this reconnection with probability $p_{\mathrm{B,reco}} = w_b$. If the reconnection is rejected, all three candidate clusters remain ordinary mesonic clusters.

We note that the baryonic spacetime colour reconnection has a bias for using rapidity as its first discriminating factor when searching for potential partners. However, we hope that, by using the extra information provided by the transverse separation between constituents, we will be able to improve upon the original baryonic colour reconnection model, especially in larger systems like heavy ion collisions.

To see the spacetime picture of an event, we have produced Fig. 7, which highlights the spacetime coordinate generation procedure outlined in Sect. 3. In the upper panel of Fig. 7, we have plotted all the clusters formed from the non-perturbative gluon splitting at the end of the shower, before any colour reconnection. The points in the plots represent cluster constituents, and the connecting lines represent the clusters.

Performing baryonic spacetime colour reconnection, using $\nu^2 = 1\ \mathrm{GeV}^2$, $d_0 = 0.5$ fm, and $w_b = 0.5$, on this event then produces the lower panel in Fig. 7, where we have highlighted the different types of clusters. Red lines correspond to rearranged clusters: (dotted) baryonic, and (solid) mesonic, while black lines are untouched clusters.

5 Modifications to the existing model

While incorporating spacetime coordinates into the Herwig 7 MPI model, we have had to modify parts of the original implementation. These changes are of a more general nature than the specifics of our model. As we wish to focus on the changes that our model has, we will report the changes in a separate contribution [46]. We summarize the most relevant modifications below:

- The kinematics is improved and produces the wanted inclusive spectrum.

Eur. Phys. J. C (2019) 79:1003 Page 9 of 15 1003

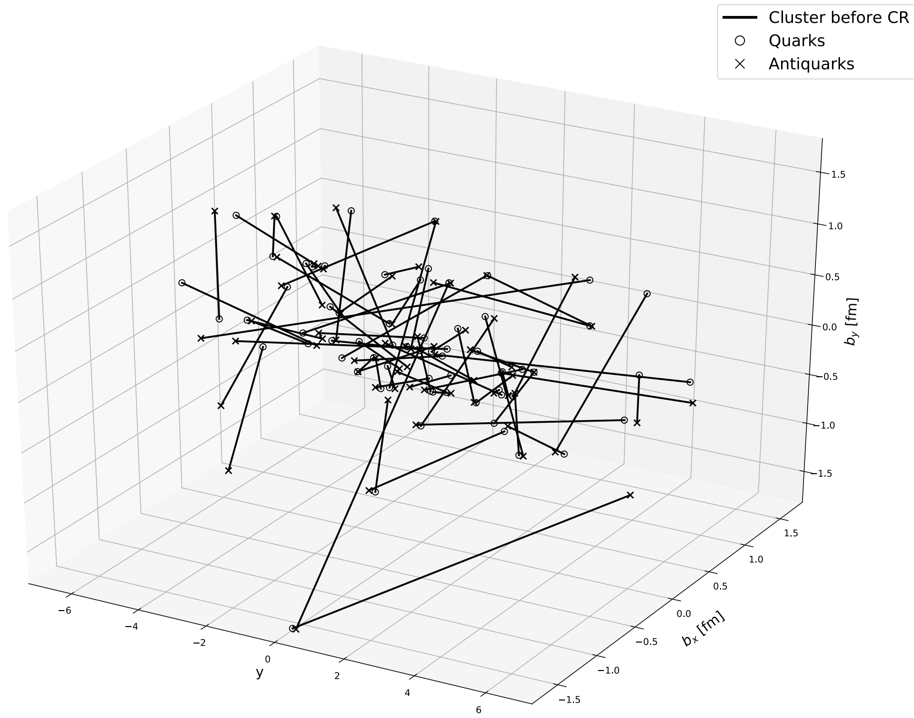

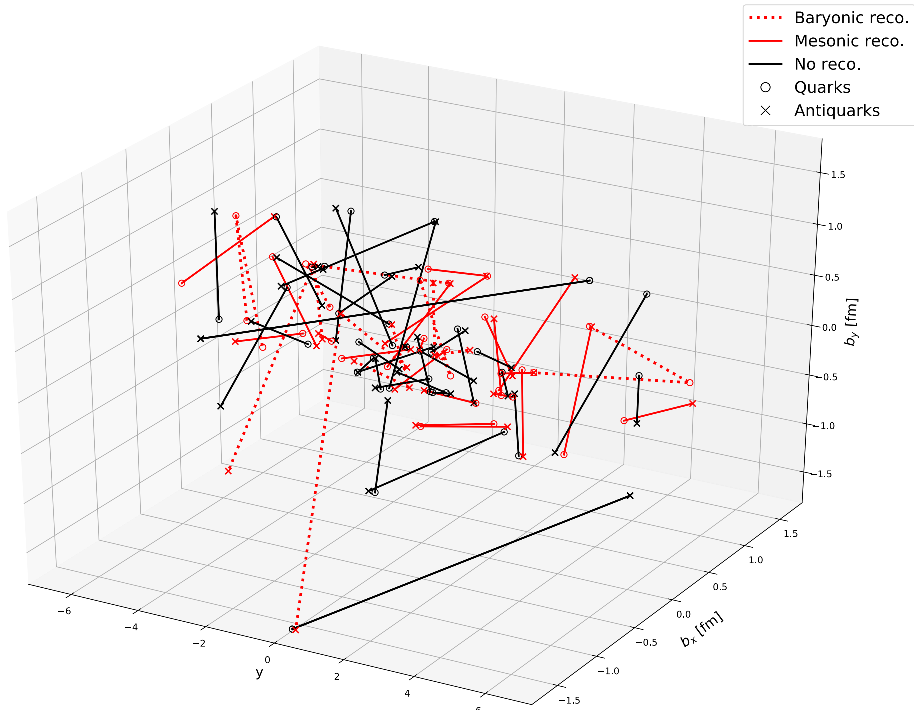

Fig. 7 The colour-topology of a sample Minimum Bias event in rapidity and transverse spacetime coordinates, before (top) and after (bottom) colour reconnection. The parameters used for reconnection here are $v^2 = 1$ GeV^2, $d_0 = 0.5$ fm, and baryonic reconnection weight $w_b = 0.5$. Black lines correspond to clusters which are automatically produced from the parton shower and which have not undergone any colour reconnection, while red lines are the newly rearranged (dotted lines) baryonic and (solid lines) mesonic clusters

- Introduction of diffraction ratio R_{Diff} parameter for better tuning performance.
- Cross-section handling takes into account the diffractive cross section to calculate the eikonalised cross sections.
- The dummy process used by Herwig 7 in Minimum Bias events is replaced to contain only initial state quarks.
- The partner finding process and scale setting are modified with respect to the standard Herwig 7 mode.

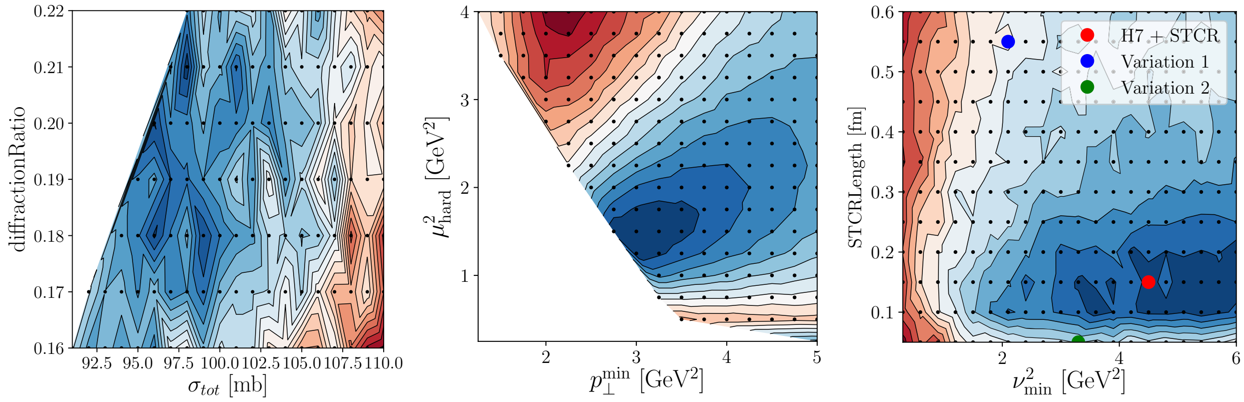

Fig. 8 χ^2-planes for parameter sets ($R_{\rm Diff}$, $\sigma_{\rm tot}$), ($\mu^2_{\rm hard}$, $p_\perp^{\rm min}$) and (ν^2, d_0). Bluer areas in the χ^2 contour plots correspond to smaller χ^2 values. In the right plot we pick three parameter pairs to define variations to be shown in the data comparison, see Figs. 9, 10, 11 and 12

The effects of these changes and their discussion are postponed to [46].

6 Tuning

We started the tuning process within the Autotunes [47] framework that internally makes use of the Rivet and Professor frameworks [48,49] for Monte Carlo event generators. To elucidate the effects of parameter variations, we illustrate the modifications in χ^2-values in Fig. 8. Here, we show by variation of strongly correlated parameter pairs where the minimum of the parameters are located. The white spaces in the planes for the parameter sets ($R_{\rm Diff}$, $\sigma_{\rm tot}$) and ($\mu^2_{\rm hard}$, $p_\perp^{\rm min}$) are regions in parameter space where the model fails to fit the soft and hard cross-sections without violating the total cross-section. In the left χ^2-plane, we added lines to mark the total cross sections that are predicted by the Donnachie and Landshoff model, where DLMode 1 refers to [50], DLMode2 refers to [50] but normalized to [51].[3]

In the (ν^2, d_0)-plane, we define three parameter points to be used in the later data comparisons. The red point, corresponding to the best fit value ($\nu^2 = 4.5$ GeV^2, $d_0 = 0.15$ fm) will be referred to as “H7 + STCR”. To show variations in the spacetime model, we choose two other points: blue – ($\nu^2 = 2.1$ GeV^2, $d_0 = 0.55$ fm), and green – ($\nu^2 = 3.3$ GeV^2, $d_0 = 0.05$ fm). These two points will be referred to as “Variation 1” and “Variation 2” in the following.

We compared the model in the tuning procedure to data from [53–57] and the red parameter point in Fig. 8 corresponds to the parameters that are reflected in Table 1.

[3] A third mode that is implemented in Herwig 7 that would refer to [52] would predict a total cross section of $\sigma_{\rm tot} = 120.496$ mb and is not acceptable with our tuning.

Table 1 The newly tuned parameters for minimum bias simulation and our baryonic spacetime colour reconnection model. The top row is the re-tuned parameters of the old Herwig 7 minimum bias model. The bottom row is the three new parameters of the spacetime components of our model, and a determined parameter of the old model

$\sigma_{\rm tot}$ [mb]	$R_{\rm Diff}$	$p_\perp^{\rm min}$ [GeV]	$\mu^2_{\rm hard}$ [GeV^2]
96.0	0.2	3.0	1.5
ν^2 [GeV^2]	d_0 [fm]	w_b	($\mu^2_{\rm soft}$ $[GeV^2]$)
4.5	0.15	0.98	0.254

The parameters in the first row have been previously included in the Herwig 7 minimum bias model. $R_{\rm Diff}$ was not explicitly part of the regular model in Herwig 7 but was effectively tuned as the amplitude of the non-diffractive cross section. $p_\perp^{\rm min}$ is the cut on the transverse momentum where the hard MPI component, described by perturbative QCD $2 \to 2$ process is taken over by the soft, multi-peripheral MPI model [9,10]. The parameter for the inverse proton radius is $\mu^2_{\rm hard}$ and is communicated together with the determined (not tuned) parameter for the soft inverse radius $\mu^2_{\rm soft}$ to the MPI coordinate generator.

The parameters in the second row are the three new parameters introduced for our spacetime model. First, the minimum virtuality ν^2, which dictates the traveling of the final partons after the shower step, takes a rather large value 4.5 GeV^2 in comparison to the parton shower Q^2 cutoff.

Second, the colour reconnection distance scale d_0 in Eq. 15 has a tuned value of 0.15 fm. This length scale is the strength of the transverse component of the spacetime measure relative to the rapidity component. It can also be considered the characteristic length scale of colour reconnection in the transverse plane in our model.

Finally, the baryonic colour reconnection probability weight w_b, after tuning, has a value of 0.98. This seems to be

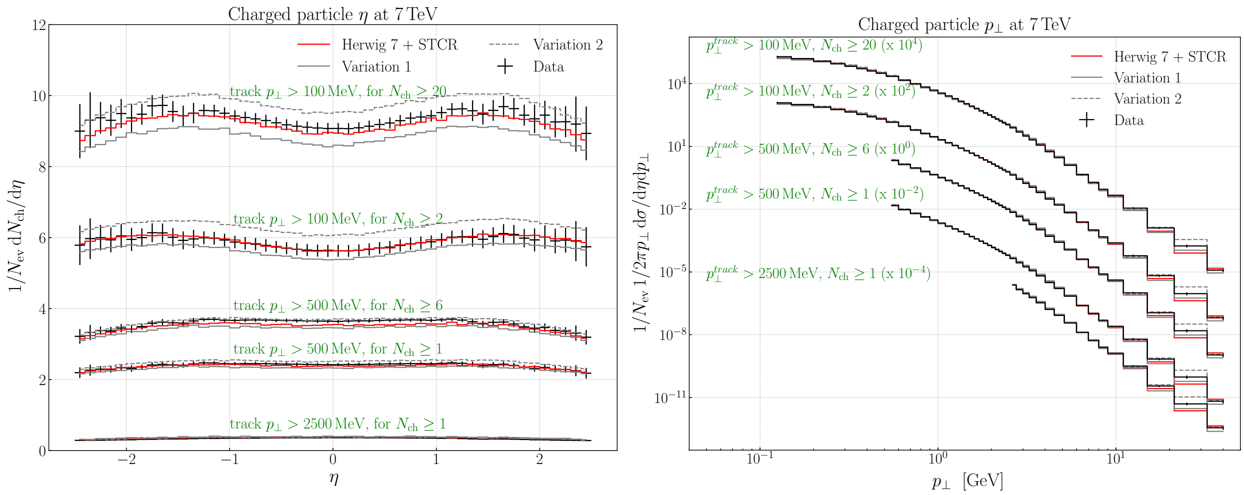

Fig. 9 Charged particle spectrum against rapidity and transverse momentum for various leading track $p_\perp$ and number of charged particle N_{ch} slices. An overall good agreement with data is found. The variation is purely in the spacetime length and minimum virtuality parameters of our model as defined in Fig. 8 and in the corresponding text

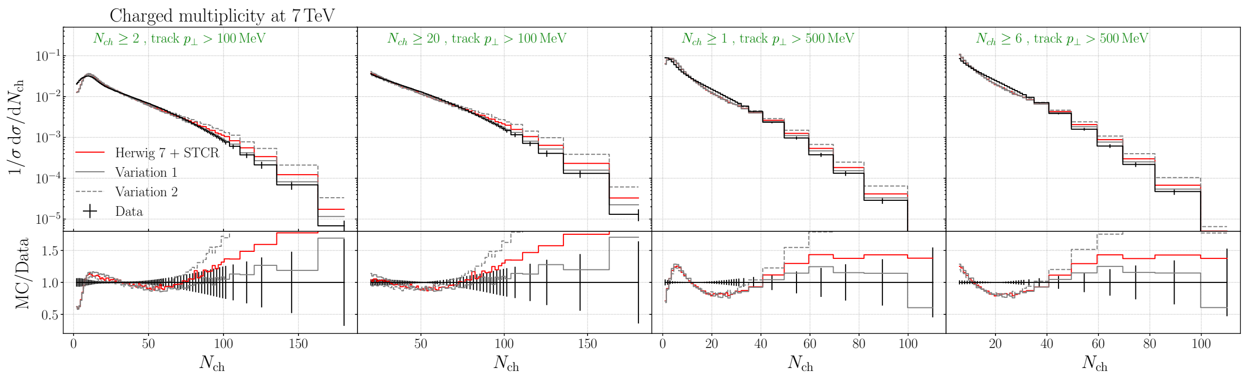

Fig. 10 Differential cross-section with respect to the number of charged particles as measured by [55]

very large but the model, as described in [14], already makes strong restrictions on the possible cluster configurations such that the cluster triplets that are potential candidates for the baryonic reconnection are strongly favoured.

We have kept the probability for strangeness production during the non-perturbative gluon splitting as the tuned value from [14], although there have been recent developments in the description of non-perturbative strangeness production in cluster hadronization [58]. We leave a full retune of all the hadronization parameters to future work.

7 Results

In this section, we describe the data comparison of the tuned parameter set. In Fig. 9, we have collated various cuts on the track momentum, and similarly on the minimum number of charged particles for the rapidity and transverse momentum distributions as measured in [55]. Beside the central parameter set (red), we also show the results of the variations as gray lines (solid and dashed). These are crucial observables for the description of Minimum Bias and soft physics, and we find that the model is perfectly capable at describing the distributions.

In Fig. 10, we compare the differential cross-section with respect to the number of charged particles as measured by [55] with our model's results. We observe that for high charged particle multiplicity the central line overshoots the data and that "Variation 1" is closer to the central data line. With the increased d_0 in "Variation 1", the colour reconnection probability is increased. For a high number of additional scatters, the probability is increased to produce smaller clusters and therefore less particle production in the cluster fission and decay processes.

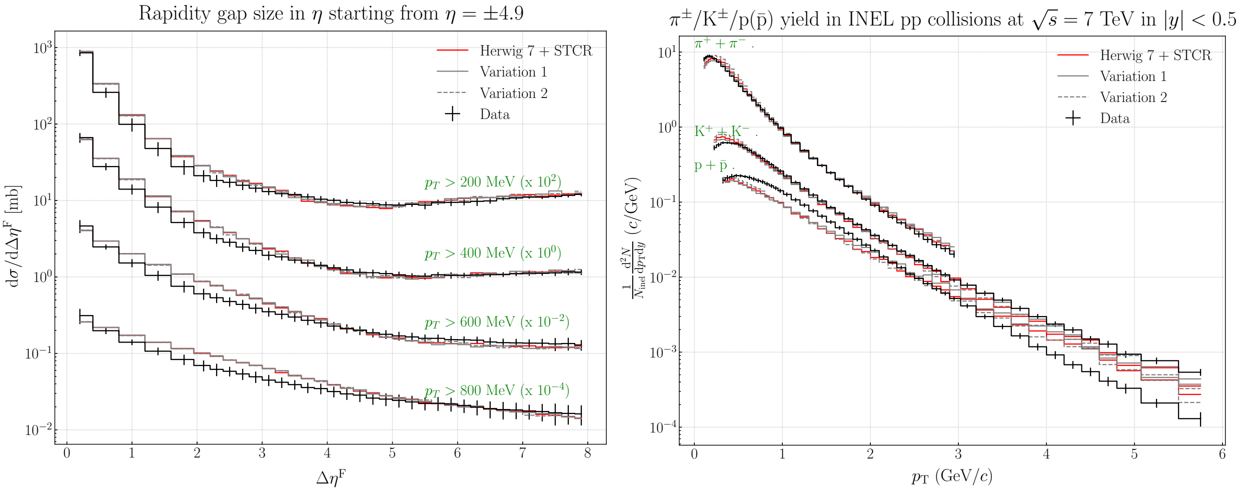

Fig. 11 Predictions for the rapidity gap fraction and the pion, kaon, and proton yields as measured by [53,59]. Variations in the spacetime components of the model show very little impact on the results

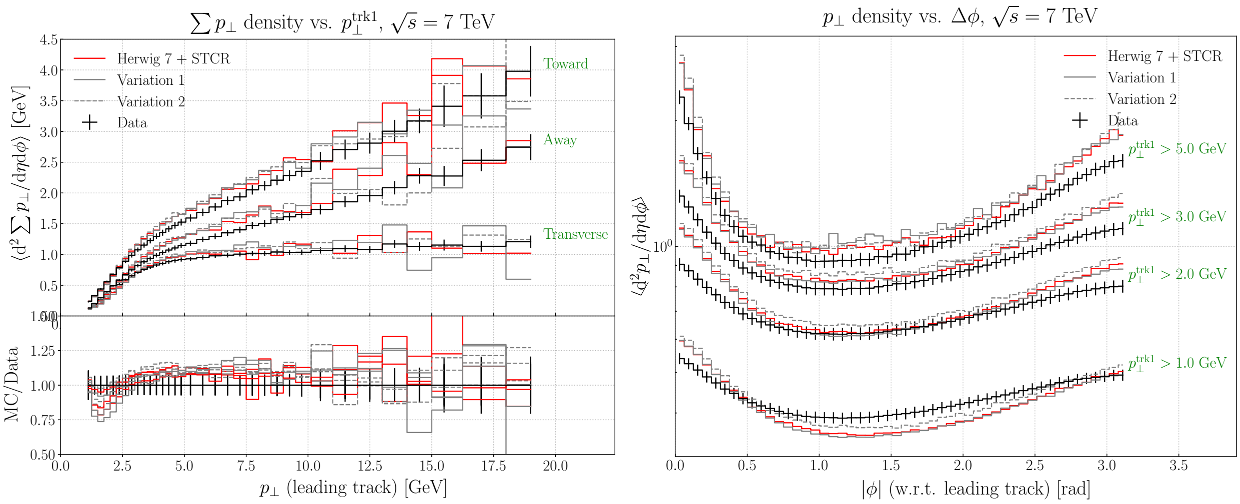

Fig. 12 Predictions for the average sum of particle transverse momenta as a function of the leading track's transverse momentum, and the average transverse momentum as a function of the azimuthal angle of the leading track [56]

To illustrate examples of observables that are hardly modified by the variations in the spacetime components of the model, we show in Fig. 11 the measured rapidity gap fraction and the pion, kaon, and proton yields as measured by [53,59]. Variations in the spacetime components of the model have very little impact on these observables. The rapidity gap for small values is mostly driven by the hard and soft MPI that could potentially be modified but is known to be relatively invariant to colour reconnection effects. The tail of the rapidity gap cross section is mainly filled by double and single diffraction, which are not modified by the smearing of the MPI collision centers. The fairly poorly described proton yield will be the subject of further studies.

Typical observables that are used to verify the description of MPI models in underlying event measurements are the angle of the particle production with respect to the leading track as well as the average sum of transverse momenta in the region towards, away, and transverse to the leading track. Comparing our model to data measured at the ATLAS collaboration [56], we find that the turn on behaviour, $p_\perp < 2.5$ GeV for the leading track, is slightly too low. This has also been seen in the previous Herwig models. For leading tracks above 2.5 GeV, the average transverse momentum sum is about 10% too large. This can also be seen in the radial dependence with respect to the leading track. In the Herwig MPI model, there is no azimuthal correlation between the additional scatters. Herwig's only mechanism to correlate the additional scatters is the colour reconnection. Introducing methods to correlate these scatters, as well as correlate them angularly, is left to future work (Fig. 12).

8 Conclusion and outlook

We have implemented spacetime coordinate generation for two stages of event simulation: the positions of MPI scattering centres, and the propagation distance in the transverse plane of partons at the end of the parton shower. We then used these transverse coordinates and the rapidity of the cluster constituents to define a measure that we minimize when performing baryonic colour reconnection, creating a model we call baryonic spacetime colour reconnection.

Overall we find that the proposed algorithm for baryonic spacetime colour reconnection gives meaningful results for many observables in Minimum Bias interactions at the LHC. This is an important step as with this prescription at hand we may explore larger systems, where spacetime structure will play an important role, as is the case in heavy ion collisions. However, we deliberately leave these new areas of study to future work after establishing the algorithm in pp collisions in the first place.

There is plenty of room for future work based on the prescription we present here. One avenue might be to look at only allowing certain MPI subsystems to reconnect with each other based on closeness in spacetime [60]. Alternatively, one may try to use the ideas of [18] but limit the computation complexity of the problem by only performing the soft-gluon-evolution inspired colour reconnection in a small neighbourhood of spacetime.

One may also look to study the final state of the event in more detail using spacetime coordinates, an avenue started by [26]. One interesting idea is the interplay between Bose–Einstein correlations, and hadron position and extent [61]. Studying these effects could help one develop a more sophisticated and systematic model for generating spacetime coordinates.

As perturbative calculations become more precise, improving hadronization phenomenological models remains a key part of Monte Carlo event generator development. Overall, we have shown that it is possible to introduce spacetime coordinates and then use this information to help assist colour reconnection and potentially other soft physics phenomena.

Acknowledgements The authors would like to thank Peter Skands and Mike Seymour for helpful comments on the manuscript, and Boris Blok for discussions about MPI. We thank the other members of the Herwig collaboration for input to discussions. This work has received funding from the European Union's Horizon 2020 research and innovation programme as part of the Marie Sklodowska-Curie Innovative Training Network MCnetITN3 (Grant Agreement No. 722104). JB acknowledges funding by the European Research Council (ERC) under the European Union's Horizon 2020 research and innovation programme, Grant Agreement No. 668679. This work has been supported by the BMBF under Grant Number 05H18VKCC1. CBD is supported by the Australian Government Research Training Program Scholarship and the J. L. William Scholarship. CBD would like to thank Lund University for their hospitality, where a portion of this work was undertaken. AS acknowledges support from the National Science Centre, Poland Grant No. 2016/23/D/ST2/02605. MM has been supported by the grant 18-07846Y of the Czech Science Foundation (GACR).

Data Availability Statement This manuscript has no associated data or the data will not be deposited. [Authors' comment: Data generated with Herwig-7.1.4. Spacetime colour reconnection will be available in a future release of Herwig. Upon reasonable request from interested parties, authors can provide the relevant code and data.]

Appendix: Formation time and mean lifetime

The discussion below is adapted from [62]. For a branching of the kind $i \to jk$ where j is the produced soft, collinear gluon, we start with the definition of q_i and expand in terms of the products of the branching:

$$\begin{aligned} q_i^2 &= \left(p_j + p_k\right)^2 \\ &= 2p_j \cdot p_k \\ &= 2E_j E_k \left(1 - \cos\theta\right) \\ &\sim E_j E_k \theta^2 \\ &= \frac{E_k}{E_j} k_\perp^2 \end{aligned} \tag{18}$$

$$\text{where } \; k_\perp := E_j \theta \tag{19}$$

where in the second line we have assumed the products are massless, and the fourth line is the small angle approximation.

Using Eq. 8 for a virtual splitting parton, and ignoring the natural width term, one obtains:

$$\tau \sim \frac{1}{\sqrt{q_i^2}}. \tag{20}$$

Since Eq. 20 is defined in the rest frame of the decaying parton, the boost factor is:

$$\gamma = \frac{E_i}{\sqrt{q_i^2}} = \frac{E_j + E_k}{\sqrt{q_i^2}} \tag{21}$$

The lifetime in the lab frame is then:

$$\begin{aligned}\tau' = \gamma\tau &\sim \frac{E_j + E_k}{\sqrt{q_i^2}} \frac{1}{\sqrt{q_i^2}} \\ &= (E_j + E_k) \frac{E_j}{E_k} \frac{1}{k_\perp^2} \\ &= \frac{E_j}{k_\perp^2}\end{aligned} \tag{22}$$

where we have used the result of Eq. 19 in the second line, and in the last line we have used the soft approximation: $E_j \ll E_k$, i.e. a very soft gluon produced from a splitting where the quark takes most of the energy and momentum.

The final expression in Eq. 22 is the standard expression for the formation time of a massless soft, collinear gluon (see [39–42] for more details).

References

1. M. Bähr et al., Eur. Phys. J. C **58**, 639–707 (2008). arXiv:0803.0883
2. J. Bellm et al., arXiv:1705.06919
3. J. Bellm et al., Eur. Phys. J. C **76**(4), 196 (2016). arXiv:1512.01178
4. T. Sjöstrand, S. Ask, J.R. Christiansen, R. Corke, N. Desai, P. Ilten, S. Mrenna, S. Prestel, C.O. Rasmussen, P.Z. Skands, Comput. Phys. Commun. **191**, 159–177 (2015). arXiv:1410.3012
5. T. Gleisberg, S. Hoeche, F. Krauss, M. Schönherr, S. Schumann, F. Siegert, J. Winter, JHEP **02**, 007 (2009). arXiv:0811.4622
6. T. Sjöstrand, M. van Zijl, Phys. Rev. D **36**, 2019 (1987)
7. J.M. Butterworth, J.R. Forshaw, M.H. Seymour, Z. Phys. C **72**, 637–646 (1996). arXiv:hep-ph/9601371
8. M. Bahr, S. Gieseke, M.H. Seymour, JHEP **07**, 076 (2008). arXiv:0803.3633
9. M. Bähr, J.M. Butterworth, S. Gieseke, M.H. Seymour, in *Proceedings, 1st International Workshop on Multiple Partonic Interactions at the LHC (MPI08): Perugia, Italy, October 27–31*, 2008, pp. 239–248 (2009). arXiv:0905.4671
10. S. Gieseke, F. Loshaj, P. Kirchgaeßer, Eur. Phys. J. C **77**(3), 156 (2017). arXiv:1612.04701
11. T. Sjöstrand, V.A. Khoze, Z. Phys. C **62**, 281–310 (1994). arXiv:hep-ph/9310242
12. S. Gieseke, C. Röhr, A. Siodmok, Eur. Phys. J. C **72**, 2225 (2012). arXiv:1206.0041
13. C. Bierlich, J.R. Christiansen, Phys. Rev. D **92**(9), 094010 (2015). arXiv:1507.02091
14. S. Gieseke, P. Kirchgaeßer, S. Plätzer, Eur. Phys. J. C **78**(2), 99 (2018). arXiv:1710.10906
15. J.R. Christiansen, P.Z. Skands, JHEP **08**, 003 (2015). arXiv:1505.01681
16. T. Sjöstrand, (2013). arXiv:1310.8073
17. L. Lönnblad, Z. Phys. C **70**, 107–114 (1996)
18. S. Gieseke, P. Kirchgaeßer, S. Plätzer, A. Siodmok, JHEP **11**, 149 (2018). arXiv:1808.06770
19. J. Bellm, Eur. Phys. J. C **78**(7), 601 (2018). arXiv:1801.06113
20. J.D. Bjorken, FERMILAB-PUB-82-059-THY
21. M. Gyulassy, M. Plumer, Phys. Lett. B **243**, 432–438 (1990)
22. G.-Y. Qin, X.-N. Wang, Int. J. Mod. Phys. E **24**(11), 1530014 (2015). arXiv:1511.00790. [309 (2016)]
23. C. Bierlich, G. Gustafson, L. Lönnblad, A. Tarasov, JHEP **03**, 148 (2015). arXiv:1412.6259
24. C. Bierlich, G. Gustafson, L. Lönnblad, arXiv:1612.05132
25. J.R. Ellis, K. Geiger, Nucl. Phys. A **590**, 609C–612C (1995). arXiv:hep-ph/9503212
26. S. Ferreres-Solé, T. Sjöstrand, Eur. Phys. J. C **78**(11), 983 (2018). arXiv:1808.04619
27. B. Andersson, G. Gustafson, G. Ingelman, T. Sjöstrand, Phys. Rep. **97**, 31–145 (1983)
28. C. Bierlich, C.O. Rasmussen, arXiv:1907.12871
29. P. Aurenche, F.W. Bopp, A. Capella, J. Kwiecinski, M. Maire, J. Ranft, J. Van Tran Thanh, Phys. Rev. D **45**, 92–105 (1992)
30. B. Webber, Nucl. Phys. B **238**(3), 492–528 (1984)
31. D. Amati, G. Veneziano, Phys. Lett. B **83**(1), 87–92 (1979)
32. S. Kirkpatrick, C.D. Gelatt, M.P. Vecchi, Science **220**(4598), 671–680 (1983)
33. G.C. Fox, S. Wolfram, Nucl. Phys. B **168**, 285–295 (1980)
34. J.R. Ellis, K. Geiger, Phys. Rev. D **54**, 1967–1990 (1996). arXiv:hep-ph/9511321
35. J.R. Ellis, K. Geiger, H. Kowalski, Phys. Rev. D **54**, 5443–5462 (1996). arXiv:hep-ph/9605425
36. G. Corcella, I.G. Knowles, G. Marchesini, S. Moretti, K. Odagiri, P. Richardson, M.H. Seymour, B.R. Webber, JHEP **01**, 010 (2001). arXiv:hep-ph/0011363
37. S. Gieseke, P. Stephens, B. Webber, JHEP **12**, 045 (2003). arXiv:hep-ph/0310083
38. S. Platzer, S. Gieseke, JHEP **01**, 024 (2011). arXiv:0909.5593
39. R. Baier, D. Schiff, B.G. Zakharov, Annu. Rev. Nucl. Part. Sci. **50**, 37–69 (2000). arXiv:hep-ph/0002198
40. J. Casalderrey-Solana, D. Pablos, K. Tywoniuk, J. High Energy Phys. **2016**, 174 (2016)
41. J.-P. Blaizot, F. Dominguez, Phys. Rev. D **99**(5), 054005 (2019). arXiv:1901.01448
42. F. Domínguez, J.G. Milhano, C.A. Salgado, K. Tywoniuk, V. Vila, arXiv:1907.03653
43. G.S. Bali, Phys. Rev. D **62**, 114503 (2000). arXiv:hep-lat/0006022
44. D. Reichelt, P. Richardson, A. Siodmok, Eur. Phys. J. C **77**(12), 876 (2017). arXiv:1708.01491
45. C. Röhr, *Colour Charge Effects in Hadronization* (Diplomarbeit, Karlsruhe Institute of Technology, 2010)
46. J. Bellm, S. Gieseke, P. Kirchgaeßer, (2019). arXiv:1911.13149
47. J. Bellm, L. Gellersen, arXiv:1908.10811
48. A. Buckley, J. Butterworth, L. Lönnblad, D. Grellscheid, H. Hoeth, J. Monk, H. Schulz, Comput. Phys. Commun. **184**, 2803–2819 (2013). arXiv:1003.0694
49. A. Buckley, H. Hoeth, H. Lacker, H. Schulz, J.E. von Seggern, Eur. Phys. J. C **65**, 331–357 (2010). arXiv:0907.2973
50. A. Donnachie, P.V. Landshoff, Phys. Lett. B **296**, 227–232 (1992). arXiv:hep-ph/9209205
51. CDF Collaboration, F. Abe et al., Phys. Rev. D **50**, 5550–5561 (1994)
52. A. Donnachie, P.V. Landshoff, Phys. Lett. B **595**, 393–399 (2004). arXiv:hep-ph/0402081
53. ALICE Collaboration, J. Adam et al., Eur. Phys. J. C **75**(5), 226 (2015). arXiv:1504.00024
54. ALICE Collaboration, B. Abelev et al., Eur. Phys. J. C **73**(6), 2456 (2013). arXiv:1208.4968
55. ATLAS Collaboration, G. Aad et al., New J. Phys. **13**, 053033 (2011). arXiv:1012.5104
56. ATLAS Collaboration, G. Aad et al., Phys. Rev. D **83**, 112001 (2011). arXiv:1012.0791
57. CMS Collaboration, V. Khachatryan et al., Phys. Rev. D **92**(1), 012003 (2015). arXiv:1503.08689

58. C.B. Duncan, P. Kirchgaeßer, Eur. Phys. J. C **79**(1), 61 (2019). arXiv:1811.10336
59. ATLAS Collaboration, G. Aad et al., Eur. Phys. J. C **72**, 1926 (2012). arXiv:1201.2808
60. B. Blok, C.D. Jäkel, M. Strikman, U.A. Wiedemann, JHEP **12**, 074 (2017). arXiv:1708.08241
61. A. Bialas, K. Zalewski, Phys. Lett. B **727**, 182–184 (2013). arXiv:1309.6169
62. G. Dissertori, I.G. Knowles, M. Schmelling, High energy experiments and theory (2003)

5.3 Errata for *Spacetime Colour Reconnection in Herwig*

1. In Figure (8), there are missing labels for DLMode1 and DLMode2, which constrain the available parameter space. The cut in the left most pane is caused by DLMode1 constraints. In the centre pane, DLMode1 causes the cut-line from (0,4) to (3.4,0.3), and DLMode2 causes the cut-line from (3.4,0.3) to (5,0).

2. In §2.1 - Multiple Parton Interactions (MPI), the sentence: *"The primary hard subprocess in Minimum Bias event generation in Herwig 7 is an interaction between two valence (antiquarks) [12], while ...* " has a typographical error. The sentence should read: *"The primary hard subprocess in Minimum Bias event generation in Herwig 7 is an interaction between two valence* ***(anti)-quarks*** *[12], while ...* " where the boldface type indicates the change.

3. In §2.2 - Cluster model, the sentence: *"It then chooses the pair of candidate clusters which have the largest rapidity span in this frame."* has a typographical error. The sentence should read: *"It then chooses the pair of candidate clusters which* ***has*** *the largest rapidity span in this frame."* where the boldface type indicates the change.

4. In the opening paragraph of §3.1 - MPI coordinate generation algorithm, the sentence: *"To obtain an intelligent and relevant value for the impact parameter, the MPI ..."* has a typographical error. The sentence should read: *"To obtain an* ***intelligible*** *and relevant value for the impact parameter, the MPI ..."* where the boldface type indicates the change.

6

Repulsive Strings

The Lund string model has been remarkably successful, agreeing very well with a large range of data from LEP and LHC. However, as discussed in Sec. 3.5, more experimental data and more rigorous tests of the model have highlighted some shortcomings. In particular, the CMS near-side ridge effect has brought into question the Lund string model's assumption that each string hadronizes independently.

The shoving model [233, 234] has shown some success at describing the near-side ridge effect, in which nearby overlapping strings push on each other with a microscopically described force, inspired by earlier analytical results [245]. To do this, the shoving model builds a set of coordinates in transverse space, then adds very soft gluon kicks to the string-segment spanning a pair of dipoles in small steps in rapidity. One issue with the shoving model is that in order to add the very soft gluons, they must be given a finite mass in order to avoid being absorbed into nearby harder gluon kicks, since the string model has a finite resolution [246].

The goal of the work presented in Sec. 6.1 is to modify the string fragmentation procedure described in Sec. 3.2.2 by introducing repulsion, without the need for a large number of very soft gluon kicks. To this end, we present a toy model for producing collective effects which works as follows: strings have a rapidity span, defined by the difference in rapidity between its endpoints. A particle's rapidity y is given by:

$$y = \frac{1}{2} \ln \left(\frac{E + p_L}{E - p_L} \right) . \tag{6.1}$$

Pseudo-rapidity (see Eq. 3.14 is the experimentally accessible analogous quantity, but for this work we will use rapidity throughout. Whenever a string break occurs, a previous endpoint is carried away by the produced hadron (see Sec. 3.2.2), and the string's new endpoint will necessarily have a smaller absolute rapidity. We can associate the change (i.e. loss) in the string's rapidity span with the produced hadron. Strings that overlap in rapidity space have an increased potential energy between them, causing them to push each other apart transversely. To generate the repulsive transverse momentum, the strings are compressed longitudinally, and the hadrons produced during the string fragmentation receive some transverse momentum. The fraction of repulsive transverse momentum that is donated to each hadron is proportional to the associated rapidity span of the hadron.

We apply this framework to pairs of simple $q\bar{q}$ string configurations, starting with the symmetric parallel case. We then generalize to more complicated string-end momenta topologies, such as strings with transversely moving endpoints, and partially overlapping strings. We show that with our model we can introduce significant two-particle azimuthal correlations that highly depend on the strength of repulsion.

In comparison to the more comprehensive shoving model, our model cannot yet be extended to arbitrary string topologies such as strings with gluon kinks, gluon loops, or junctions. However, as we show in the paper, our model circumvents the issues that Pythia has with handling very soft gluons, as well as having a much larger impact on azimuthal correlations in comparison to the effects from the shoving model.

6.1 Published Material

Since the submission of this thesis, the paper has been accepted by SciPost Physics Journal, under an amended title: *Fragmentation of Two Repelling Lund Strings*, SciPost Phys. 8, 080 (2020), DOI: 10.21468/SciPostPhys.8.5.080.

Fragmentation of Two Repelling QCD Strings

Cody B Duncan and Peter Skands

Submitted to SciPost Physics Journal

DOI:

e-Print: arXiv:1912.09639 [hep-ph]

CoEPP-MN-19-5, MCNET-19-30

Paper begins overleaf

SciPost Physics Submission

Fragmentation of Two Repelling QCD Strings

Cody B Duncan[1*] and Peter Skands[1]

1 School of Physics & Astronomy, Monash University, Clayton, VIC 3800, Australia

* cody.duncan@monash.edu

Motivated by recent discoveries of flow-like effects in pp collisions, and noting that multiple string systems can form and hadronize simultaneously in such collisions, we develop a simple model for the repulsive interaction between two QCD strings with a positive (colour-oriented) overlap in rapidity. The model is formulated in momentum space and is based on a postulate of a constant net transverse momentum being acquired per unit of overlap along a common rapidity direction. To conserve energy, the strings shrink in the longitudinal direction, essentially converting m^2 to $p_\perp^2$ for constant $m_\perp^2 = m^2 + p_\perp^2$ for each string. The reduction in m^2 implies a reduced overall multiplicity of produced hadrons; the increase in $p_\perp^2$ is local and only affects hadrons in the overlapping region. Starting from the simplest case of two symmetric and parallel strings with massless endpoints, we generalize to progressively more complicated configurations. We present an implementation of this model in the Pythia event generator and use it to illustrate the effects on hadron $p_\perp$ distributions and dihadron azimuthal correlations, contrasting it with the current version of the "shoving" model implemented in the same generator.

Contents

1 Introduction

Hadronization models play an essential role in the description of hadronic events in high-energy collisions, connecting the short-distance physics of quarks and gluons with the observable world of colourless (long-lived) hadrons via a dynamical process that enforces confinement. The two major models of hadronization used in proton-proton event generation are the Lund string model [1–4] and the cluster model [5–7], with the former implemented in Pythia [8–10] and Epos [11, 12], and the latter in Herwig [13–15] and Sherpa [16, 17].

While the Lund string model has been able to qualitatively describe a large number of hadron-level observables from e^+e^- to proton-proton collisions across a wide range of CM energies (see e.g. MCPLOTS [18]), recent data in particular from the LHC experiments have highlighted some shortcomings. ALICE has shown unequivocally that strangeness production increases as a function of event multiplicity in minimum-bias event samples [19, 20], while CMS discovered the near-side ridge in high-multiplicity events [21, 22]. The latter has been elaborated upon in a number of studies by both ATLAS and CMS [23–27], and there are also several additional indications of strangeness enhancement e.g. in the underlying event [28–30]. Both of these phenomena are widely believed to have their roots in collective effects, but in the baseline Lund string model, each string hadronizes independently of the others (modulo effects of colour reconnections, see, e.g. [31]).

Several proposals have been made that can potentially explain these phenomena. Rope hadronization [32, 33] takes aligned strings in rapidity and enhances their string tensions based on a Casimir scaling argument [34, 35], leading to increased strangeness production and higher average $p_\perp$ values in string breaks. Shoving, a mechanism for microscopic string-string interactions which generates transverse momentum pressure between overlapping strings, was proposed in [36, 37] and showed long-range azimuthal correlations. Both the Rope and shoving model have been implemented in Pythia, Dipsy [38], and Angantyr [39]. Alternatively, the approach taken by Epos [12] invokes the notion of a critical string density beyond which a heavy-ion inspired hydrodynamic modelling takes over, which includes collective flow and thermally enhanced strangeness production. Yet a third line of argument is that colour reconnections (CR) can produce flow-like effects [40], essentially by creating net boosted hadronising systems. Baryon-to-meson ratios may also be altered by CR effects [41] but would have to be supplemented by something like Rope hadronisation to significantly alter net strangeness fractions. Other models proposed include thermodynamic string fragmentation [42], which used an exponential transverse mass spectrum instead of the usual Gaussian form. Recent work on the cluster model has also tried to capture some of the collective-like effects seen by introducing baryonic clusters and strangeness enhancement in Herwig [43, 44].

We here take the same basic starting point as the shoving model [36, 37], namely that nearby QCD strings should exert a force upon one another. We focus on repulsive forces since we assume that colour-reconnection models such as [41] (based on colour algebra and string-length minimisation) provide a first approximation to any attractive effects. We further assume that all of the hadronizing colour charges emanate from a region that is small compared with the typical width of a string. This restricts the applicability of our model to small systems but allows us the simplification of working entirely in momentum space. By contrast, the shoving model adopts an explicit picture of the spatial distribution and time evolution of the strings. (The space-time structure of hadronization in the Lund model was also recently further explored in [45].) Furthermore, the effect of the interaction is in our model represented via a global rescaling of the 4-momenta of the string endpoints combined with a local addition of $p_\perp$ to hadrons formed in regions of string overlap, while the shoving model imparts transverse momentum by adding a number of low-energy slightly massive gluons to each string. Despite similar physical starting points, we therefore do expect some qualitative differences to arise between the shoving model [36,37] and our momentum-space realization of repelling strings.

The article is organized as follows. Sec. 2 presents a short review of the Lund string model with emphasis on those features that are most relevant to our toy extension model. Sec. 3 introduces our string-string interaction model in the context of the simplest two-string configuration, and presents how the repulsion is implemented during string fragmentation, and the effects on primary hadron transverse momentum. We then extend this formalism to a more general parallel two-string configuration in Sec. 4 and then to strings with endpoints with both longitudinal and transverse momentum in Sec. 5. To make a connection with the phenomenological characterisations of collective flow used in heavy-ion inspired studies, we illustrate the effects on two-particle cumulants, $c_2\{2\}$, for selected two-string configurations in Sec. 6. In Sec. 7, we discuss the effects of decays of short-lived primary hadrons. Modifications for strings with massive endpoints are briefly discussed in Sec. 8 before we conclude and give an outlook for future work in Sec. 9.

2 Lund String Model

The Lund string model [1–4] is based on the linear nature of the confinement potential $V(r) = \kappa r$ between static quark-antiquark pairs separated by distances greater than about a femtometre (see e.g. [35]). Strings are implemented in Pythia at the end of the perturbative shower, where long colour-chains produced by the shower are collected into colour singlets, the so-called Lund strings.

A Lund string represents a confined gluonic flux tube or vortex line. In the simplest case it runs between a quark endpoint via any number of intermediate gluons (which generate transverse kinks in the structure) to an antiquark endpoint. Other colour topologies are possible as well, such as junctions and gluon loops. In this work, we restrict our attention to simple $q\bar{q}$ strings without any transverse gluon excitations.

As the endpoints propagate outward in opposite directions from the production point, their energy and momentum gets transferred to the Lund string that stretches between them. When sufficient energy is available, new $q'\bar{q}'$ pairs can be produced in the string field (typically by invoking a Schwinger-type tunneling mechanism [46]); the string thereby breaks into successively shorter pieces each of which ultimately becomes an on-shell hadron, in a process called fragmentation. In the ordinary Lund string model, each string fragments independently, and each string break is independent of any others.

Fragmentation proceeds by successively splitting off one hadron from either endpoint (chosen at random), with the created hadron at each step taking a fraction z of the string's available lightcone momentum distributed according to the Lund symmetric fragmentation function:

$$f(z) = N\frac{(1-z)^a}{z}\exp\left(\frac{-bm_\perp^2}{z}\right) \ , \tag{1}$$

with the leftover string retaining the remainder $1-z$. N is a normalisation constant and a and b are phenomenological parameters to be determined from fits to data, see e.g. [47,48]. $m_\perp^2 = m^2 + p_\perp^2$ is the transverse mass of the produced hadron; its $p_\perp$ is obtained as the (vector) sum of the $p_\perp$ values of each of its constituent quarks. In the absence of collective effects each string break is assumed to impart an equal and oppositely oriented $p_\perp$ to the produced quark and antiquark, which by default is given a Gaussian distribution, by analogy with the Schwinger mechanism in QED [46]. In the Rope model [32], the coherent fragmentation of multiple nearby colour charges can cause the width of this $p_\perp$ distribution (as well as strangeness and baryon production probabilities) to increase. While we believe those arguments to be fundamentally correct, for simplicity we focus in this work solely on the collective repulsion aspect, keeping other string-breaking aspects unmodified.

2.1 Fragmentation and rapidity

In the context of interacting strings, we will be interested in the effective overlap in rapidity between a produced hadron and a nearby string piece. To start with, we need an expression for the rapidity span taken by each hadron along an axis defined by its own string system.

Letting m_0 denote a generic hadron mass, the rapidity span of a simple $q\bar{q}$ string with massless endpoints traveling in opposite directions along the z-axis is:

$$\begin{aligned}\Delta y_0 &= \ln\left(\frac{W_{+q}}{m_0}\right) - \left[-\ln\left(\frac{W_{-\bar{q}}}{m_0}\right)\right] , \\ &= \ln\left(\frac{W^2}{m_0^2}\right) ,\end{aligned} \tag{2}$$

where $W_\pm = E \pm p_z$ are their lightcone momenta, and $W^2 = W_+W_-$ is the squared invariant mass of the string. Throughout this work, we will use the z axis as the (common) rapidity axis, and our example configurations will be defined so that this is reasonable, but there is obviously nothing special about this choice; the formalism we develop can be applied for any choice of axis.

After a hadron, h, is split off from one of the endpoints, let the invariant mass of the leftover string be W'^2. The size of the rapidity interval associated with the produced hadron can then be identified with the difference:

$$\Delta y_h = \ln\left(\frac{W^2}{m_0^2}\right) - \ln\left(\frac{W'^2}{m_0^2}\right) = \ln\left(\frac{W^2}{W'^2}\right) \ , \tag{3}$$

which is independent of m_0. App. A elaborates on how Eq. (3) relates to the sequence of z fractions and hadron mass values for arbitrary (sequences of) string breaks, using the notation from [4, 45] which also matches the code implementation. Below, we shall use these expressions to quantify the total rapidity overlap that a given hadron has with a nearby string piece.

3 Repulsion Between Two Parallel Identical Strings

We start by considering the simplest possible configuration: two straight and parallel strings of the same squared invariant mass, W^2.

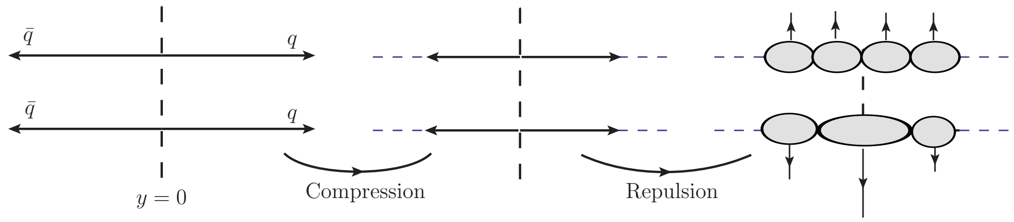

Figure 1: Schematic diagram of the simplest two-string configuration and the two steps in our model: compressing the strings (black solid lines) and repulsion during the string's fragmentation. The hadrons (grey ovals) receive $p_\perp$ proportional to the string length they take. We have ignored the Gaussian transverse momentum generation in the Lund string model for the purposes of this figure. The transverse separation between the strings in the diagram is for clarity.

Viewed in space-time, the repulsion between two such strings should depend on their (time-dependent) transverse separation distance [49, 50]. However, in the context of hadronization in high-energy particle collisions, the preceding perturbative stages of event generation are normally treated in momentum space, i.e. in terms of plane-wave approximations that are not well localized in space-time. Thus, one faces a problem of mapping partons represented in momentum space onto string systems represented in space-time. In the framework of classical string theory, on which the Lund model is based, one may simply use the string tension κ to convert between the two pictures. But when multiple string systems are involved, any interactions between them will depend on the space-time separation between the production points of each system, which the momentum-space perturbative boundary conditions only serve to fix up to an ambiguity $\propto 1/\Lambda_{\mathrm{QCD}}$. Moreover, while a strict classical interpretation would in principle allow for arbitrarily small separations, string descriptions are only appropriate for long-distance QCD. Interesting work has been done recently to bridge the two pictures [45, 51], but for the purpose of this study we would like to explore how far we can get if we stay in momentum space.

Our underlying assumption will be that our colliding systems are of order a hadronic size (hence we do not address heavy ions) and that, by the time strings are formed, they are already at least some "typical" transverse distance apart, again of order hadronic sizes even if the directions of motion of the endpoints were originally completely parallel. We make the boost-invariant ansatz that parallel strings impart a constant amount of net transverse momentum to each other per unit of overlap in rapidity,

$$\frac{\mathrm{d}p_{\perp R}}{dy} = c_R \,, \tag{4}$$

where the constant c_R, which has dimensions of GeV per unit rapidity, represents the main tuneable parameter in our model. It controls the strength of the repulsion, or alternatively, the conversion strength of longitudinal momentum into transverse momentum.[1] Non-parallel configurations will be discussed below. We further make the ansatz that each hadron produced in the overlap region receives a fraction of the total repulsion $p_\perp$ in proportion to (the overlapping portion of) its rapidity span according to Eq. 3.

A schematic diagram of how our model works is shown in Fig. 1. In a first step, we remove an amount of longitudinal momentum from the original endpoints ("compression"), in proportion to the size of the total rapidity overlap between the two strings. In the second

[1] In a future extension we shall relate this to an increase in the tension of the individual strings as well, in a manner similar to what is done in Rope hadronization, but this is outside the scope of this work.

step, the energy that was removed in the compression step is imparted back to the hadrons formed in the region(s) of overlap, as transverse momentum ("repulsion").

3.1 String Compression

Each string is defined by its two endpoints, which for simplicity we take to be massless for now and travelling in opposite directions along the z axis. Right-moving endpoints thus start out with lightcone momenta $W_+ = 2E$ and $W_- = 0$ and vice versa for the left-moving ones. In the fully symmetric setup we consider here, both strings will undergo the same transformations described below. We focus on just one of them.

Since the strings have equal invariant masses, the overlap is simply the full rapidity span of each string, i.e. $\Delta y_{\mathrm{ov}} = \Delta y_{\mathrm{string}}$, which is given by Eq. (2). For this work, we found that using too small an m_0 can lead to pathological results since this presumes that every hadron you can create has an invariant mass of that order. Instead, we will choose to work with $m_0 = m_\rho = 0.77$ GeV. Thus, by integration of Eq. (4) the $p_\perp$ gained by each string will be:

$$p_{\perp R} = \pm c_R \cdot \Delta y_{\mathrm{ov}}, \tag{5}$$

where the $\pm$ sign symbolically represents that the kicks will act in opposite directions, so that no net $p_\perp$ is gained by the string-string system as a whole.

To conserve energy, this $p_\perp$ must be acquired at the expense of some amount of longitudinal momentum. We start by defining a set of intermediate rescaled lightcone momenta $W'_\pm = f_\pm W_\pm$ with

$$f_+ f_- = 1 - \frac{p^2_{\perp,R}}{W^2} \leq 1, \tag{6}$$

which corresponds to a W' string system with a lower invariant mass,

$$W'_- W'_+ = W'^2 = W^2 - p^2_{\perp R} \ . \tag{7}$$

This first step of the model is illustrated by the left-hand part of Fig. 1, labelled "Compression". In the simple case studied in this section the compression factors f_+ and f_- must be equal for symmetry reasons. (More general cases, with $f_+ \neq f_-$, will be considered in the next section.)

A particularly simple way of representing the repulsion effect would be to boost the W' system transversely by a factor $\vec{\beta}_\perp = \vec{p}_{\perp R}/W'$. However, as G. Gustafson demonstrated during enjoyable discussions in Lund, such a boost would assign relatively more of the repulsion $p_\perp$ to high-rapidity hadrons than to central ones, in contrast with the manifestly longitudinally invariant form of Eq. (4). Instead, we therefore modify the fragmentation of the W' system in a more local way, by allowing each produced hadron to receive an additional amount of $p_\perp$ in a manner designed to reproduce Eq. (4).

Writing the 4-vectors as $(p_+, p_-, \vec{p}_\perp)$, the W' system is defined by:

$$\begin{aligned} p'_q &= f W_+ \left(1, 0, \vec{0}_\perp\right), \\ p'_{\bar{q}} &= f W_- \left(0, 1, \vec{0}_\perp\right) \ . \end{aligned} \tag{8}$$

As remarked above, this has a lower total energy, W', than that of the original system. The "missing energy" will gradually be added back during the fragmentation process, in the form of additional $p_\perp$ given to the hadrons that are formed in the region(s) of overlap. Unlike the standard fragmentation $p_\perp$ in string breaks, which is randomly and independently distributed in azimuth for each breakup, a single global ϕ choice characterises the $p_\perp$ component from repulsion (with $\pi + \phi$ used for the hadrons in the recoiling string system). We will now discuss the details of this second step, illustrated by the right-hand part of Fig. 1, labelled "Repulsion".

3.2 Repulsion

As mentioned in Sec. 2.1, we can assign a rapidity span to each hadron as it gets produced by the rapidity span lost by the string when producing the hadron. Using Eq. (36), a hadron receives a corresponding fraction of $p_{\perp R}$, calculated in the same manner as Eq. (5):

$$p_{\perp h} \;=\; c_R \Delta y_h \;=\; p_{\perp R} \frac{\Delta y_h}{\Delta y_{\mathrm{string}}}, \tag{9}$$

where Δy_h is the rapidity span of the string taken by the hadron, such that $\sum \Delta y_h = \Delta y_{\mathrm{string}}$, and consequently the summed repulsion momentum given to hadrons is equal to the total repulsion momentum. Generalising to cases in which the two strings do not fully overlap, the numerator and denominator of the rapidity-span ratio in the last expression can simply be changed to refer to the overlapping portions of the hadron and total rapidity spans, respectively. After the hadron receives the repulsion $p_\perp$, its energy is then adjusted by the amount required to put it back on shell. In this way, the “missing energy” discussed above is gradually added back to the system.

Note that, if there were no other sources of transverse momentum, putting a hadron on-shell after the repulsion would always increase its energy. However, since each string break is associated with a randomly distributed fragmentation $p_\perp$ (with each hadron in general receiving contributions from two such breaks), which must be added vectorially to the repulsion $p_\perp$, some hadrons may have lower total $p_\perp$ after adding the repulsion effect. In our modeling setup, such hadrons are regarded as donating some energy back to the string system's reservoir of “missing energy”, with the sum over all hadrons still respecting eq. (5).

With this modification, we follow the same iterative fragmentation procedure as in ordinary Pythia, splitting off hadrons from either end, allowing them to receive additional repulsion $p_\perp$ and putting them back on shell, until the invariant mass of the remaining string system drops below a cutoff value:

$$W_{\mathrm{rem}}^2 < W_{\mathrm{stop}}^2. \tag{10}$$

At this point, we add any remaining repulsion $p_\perp$ to the remnant object, as well as any energy that is still missing from the compression process. This makes total energy and momentum conservation explicit. Pythia then produces two final hadrons from this modified remnant string.

3.3 Results

In the rest of this section, we study the consequences of our model for an explicit example configuration defined by:

$$\begin{aligned} p_{+1} = p_{+2} &= 400 \left(1, 0, \vec{0}_\perp\right) \text{ GeV} , \\ p_{-1} = p_{-2} &= 400 \left(0, 1, \vec{0}_\perp\right) \text{ GeV} . \end{aligned} \tag{11}$$

To highlight the effects of the fragmentation repulsion, we have chosen endpoint energies of 200 GeV (corresponding to rather long strings), and, at this stage, consider only primary hadrons (hadrons that are produced directly from the fragmenting string). The smearing caused by decays of (short-lived) primary hadrons into secondaries will be discussed in Sec. 7.

The left pane of Fig. 2 shows the average $p_\perp$ of primary hadrons as a function of Δy_h, as defined by Eq. (3). The red dashed histogram shows the results of using the

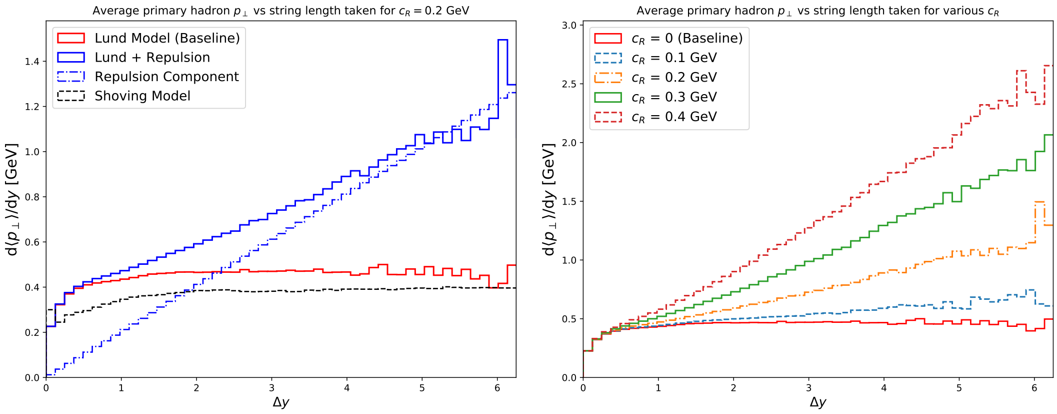

Figure 2: Distribution of average primary-hadron $p_\perp$ as a function of Δy_h. *Left:* comparison of baseline Lund model (red solid line) to our model for $c_R = 0.2$ GeV (blue solid line), our model with only the repulsion $p_\perp$ component (blue dot-dashed line) and the shoving model (black dashed line). The shoving model exhibits a lower average $p_\perp$ since the soft gluons it adds make the strings longer causing the multiplicity of produced hadrons to increase faster than the total $p_\perp$. *Right:* the effect of varying the repulsion strength c_R.

ordinary Lund model, which — since the Gaussian transverse momentum generation in the baseline Lund model is independent of the rapidity span — is a flat distribution modulo endpoint effects, The two blue histograms illustrate the effects of our compression and fragmentation repulsion model, for a representative value of $c_R = 0.2$ GeV. The dot-dashed histogram shows the repulsion component by itself (obtained by turning off the Gaussian fragmentation $p_\perp$ component via `StringPT:sigma = 0`). The solid blue histogram shows the combination of the fragmentation and repulsion $p_\perp$ components, for the same reference value of c_R. For small Δy, this mimics the baseline string model, while for large Δy, the repulsion $p_\perp$ takes over as the dominant source of transverse momentum.

We also include a comparison to the shoving model as implemented in Pythia 8.2 [36, 37]. For the shoving parameters used in our study (see App. B for details), the average transverse momentum per unit rapidity span taken actually decreases relative to the baseline (solid red) model. We interpret this as a result of the physical mechanism by which the shoving model pushes the two strings apart, which is implemented as a number of very soft transverse gluon excitations. While this does increase the total $p_\perp$, it also increases the total string length. The latter in turn increases the hadron multiplicity, with the result that the average $p_\perp$ per hadron can decrease. In our model, by contrast, the compression step ensures that the total multiplicity decreases; the repulsion step then adds $p_\perp$, implying that both the total and the average $p_\perp$ per hadron must increase.

The results of varying c_R from 0 GeV (equivalent to the no-repulsion baseline case) to 0.4 GeV per unit of rapidity overlap are shown in the right panel of Fig. 2. As c_R increases, the slope of the average hadron $p_\perp$ increases with the rapidity span of the string taken, as expected from the ansatz in Eq. (9).

In Fig. 3, we show the same model examples but now as a function of the more directly observable rapidity of the hadrons, instead of the rapidity span they take. For the normal Lund string model, this produces a variant of the famous rapidity plateau (red solid line). For the parameters we studied, the shoving model (dashed black line) does not change the average $p_\perp$ appreciably (while the average multiplicity of the event is increased [37]). In contrast, for our reference value of $c = 0.2$ GeV, our repulsion model (blue solid line, with the repulsion component illustrated by the blue dashed line) does increase the average

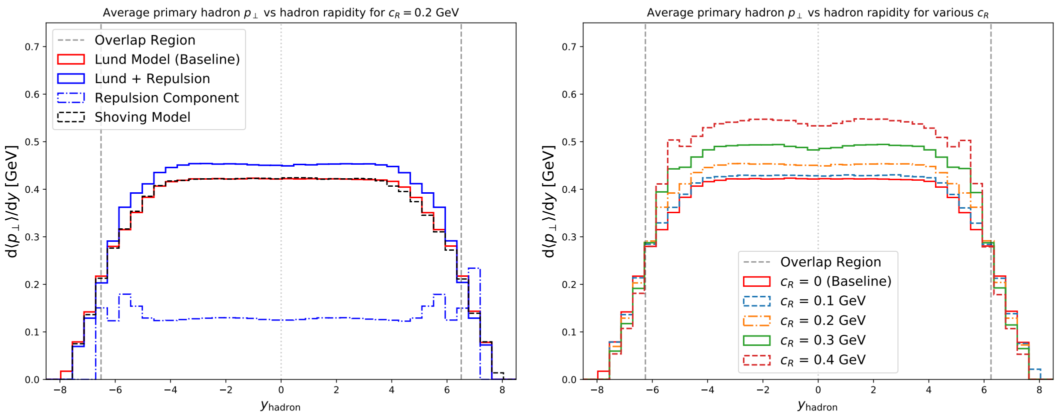

Figure 3: Distributions for the average $p_\perp$ of primary hadrons as a function of the hadron's rapidity for the symmetric parallel strings configuration. *Left*: comparison of the baseline Lund model (red solid line), with our fragmentation repulsion model (blue solid line), which has a higher $\langle p_\perp \rangle$ in the plateau region. The component which is due to the repulsion effect is illustrated by the blue dot-dashed line. Also shown is the result of using the shoving model (black dashed line) [37], for the same string configuration. The shoving model does not have significant deviation from the baseline Lund model for this observable (see text). *Right*: the effect that varying the repulsion strength c_R.

primary hadron $p_\perp$. The net increase is less than linear since the ordinary (Gaussian) fragmentation $p_\perp$ is oriented randomly with respect to the repulsion $p_\perp$, and the two components add vectorially.

As in the previous figure, the right panel of Fig. 3 illustrates the effect of varying c_R in the range 0 to 0.4 GeV per unit of rapidity overlap. For larger values of c_R, the rapidity plateau begins to lose some of its flat structure, particularly in the middle of the string, near $y_{\mathrm{hadron}} = 0$. To fix the flatness, one may adjust the stopping mass parameter W^2_{stop} in Pythia's implementation of the string model, though this is outside the scope of this work.

4 General Parallel Two-String Configuration

We now extend the considerations in Sec. 3 to a more general configuration, by letting the strings have an arbitrary parallel configuration. Without loss of generality, we assume that the two strings do still overlap, either partially, or one string's rapidity span is fully contained inside the rapidity span of the other. Relabeling as needed, we require in the former case that the left-moving (W_-) end of string 1 is contained within the rapidity span of string 2, and the right-moving (W_+) end of string 2 is contained within the rapidity span of string 1.

In the context of the momentum-space representation of the Lund model that our repulsion framework is based on, the full space-time evolution of a string is determined solely by the starting values of the 4-momenta of its endpoints. By initially reducing these momenta, the "compression" step of our model expresses the physical expectation that, as two nearby strings expand simultaneously and repel each other, it will not be possible to convert *all* of the kinetic energy of their endpoints into potential energy stored in the corresponding strings; instead, some fraction of the original kinetic energy is "held in reserve", to be converted into transverse momentum during the fragmentation process.

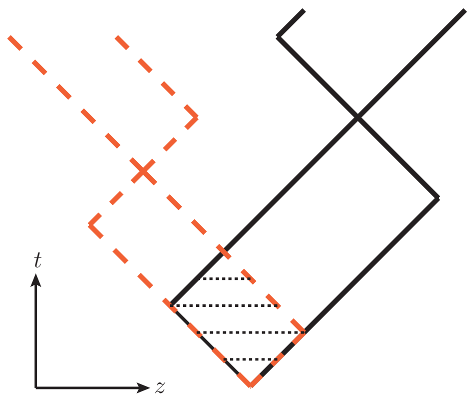

Figure 4: Schematic (1+1)-D spacetime diagram of the general parallel two-string configuration, where the two strings have a region of overlap (dotted parallel lines). The two endpoints in the region of overlap will be subjected to more compression and repulsion.

When we now turn to consider asymmetric configurations, we must answer not only how much of the total kinetic energy must be held in reserve in this way, but also which fraction of it to take from each of the reservoirs represented by the two endpoints.

In our fragmentation repulsion model, we will use the ansatz that endpoints "inside" a region of overlap should undergo more compression than ones "outside", since the corresponding string regions experience more of the accumulated interaction. In Fig. 4, we show a (1+1)-D diagram of a general string configuration, with an overlapping region centred around a slightly negative rapidity (in the given frame). The right-moving endpoint of the dashed-orange string piece overlaps with the solid-black string system during the entire time over which its original kinetic energy is converted to potential energy. By contrast, the left-moving endpoint of the same dashed-orange string piece only overlaps with the black system during half of the time that it takes to convert all of its kinetic energy to potential energy. In this sense, the right-moving endpoint can be considered to be "inside" the region of overlap while the left-moving one ultimately travels "outside" of that region. Alternatively, the portion of the black-solid string system that is represented by its left-moving endpoint has a bigger fraction of total overlapping area than the portion that is represented by its right-moving endpoint.

4.1 String Compression

In the general case that the strings are not symmetric in the longitudinal direction, one must make a choice whether to allow them to exchange p_L or not. For simplicity and since we wish to focus on the transverse repulsion effects here, we choose to ignore the possibility of p_L exchange in this first version version of our model. Thus, the only change with respect to the symmetric case is that the rescaling factors for each of the four endpoint momenta will no longer be equal.

Regardless of longitudinal recoil, the compression factors for each string system $i \in [1, 2]$ must satisfy:

$$\begin{aligned} f_{+1}f_{-1} = f_1^2 = 1 - \frac{p_{\perp,R}^2}{W_1^2} \ , \\ f_{+2}f_{-2} = f_2^2 = 1 - \frac{p_{\perp,R}^2}{W_2^2} \ , \end{aligned} , \tag{12}$$

where $p_{\perp,R}$ is the total $p_\perp \propto \Delta y_{\mathrm{ov}}$ from repulsion to be assigned (equally and oppositely) to the two systems, see eq. (5), and longitudinal momentum conservation, $\Delta p_{L,1} = -\Delta p_{L,2}$, implies:

$$\begin{aligned}(1-f_{+1})W_{+1} - (1-f_{-1})\,W_{-1}& \\ = (1-f_{-2})\,W_{-2} - (1-f_{+2})\,W_{+2}\ .&\end{aligned} \tag{13}$$

This gives three constraints for four unknowns. Imposing the further condition of no longitudinal momentum exchange, $\Delta p_{L,1} = \Delta p_{L,2} = 0$, eq. (13) separates into:

$$\begin{aligned}(1-f_{+1})\,W_{+1} - (1-f_{-1})\,W_{-1} = 0,\\ (1-f_{-2})\,W_{-2} - (1-f_{+2})\,W_{+2} = 0.\end{aligned} \tag{14}$$

The problem can then be solved with a unique set of solutions for each compression factor $f_{\pm i}$. Inserting the first two constraints Eq. (12) into Eq. (14), we obtain a quadratic equation for f_{-i}:

$$W_{-i}f_{-i}^2 + (W_{+i} - W_{-i})\,f_{-i} - f_i^2 W_{+i} = 0. \tag{15}$$

Since the compression factors must be positive, there is only one solution to this equation:

$$f_{-i} = \frac{(W_{-i} - W_{+i}) + \sqrt{(W_{-i} - W_{+i})^2 + 4W_i^2 f_i^2}}{2W_{-i}}, \tag{16}$$

or equivalently using the longitudinal momentum component $W_{Li} = (W_{+i} - W_{-i})/2$,

$$\begin{aligned}W'_{-i} = f_{-i}W_{-i} = \sqrt{W_{Li}^2 + W_i^2 f_i^2} - W_{Li}\ ,\\ W'_{+i} = f_{+i}W_{+i} = \sqrt{W_{Li}^2 + W_i^2 f_i^2} + W_{Li}\ .\end{aligned} \tag{17}$$

In the limit of $W_{+i} = W_{-i}$, i.e. $W_{Li} = 0$, we reproduce the symmetric case for the given string i, i.e. $f_{\pm i} = \sqrt{f_i^2}$. By construction, longitudinal momentum is conserved, $W'_{+i} - W'_{-i} = W_{+i} - W_{-i}$. However, energy is not:

$$E'_i = \frac{W'_{+i} + W'_{-i}}{2} = E_i\sqrt{1 - \frac{p_{\perp,R}^2}{E_i^2}}\ . \tag{18}$$

When we perform the fragmentation repulsion, we regain the "lost" energy by giving the primary hadrons the repulsion $p_\perp$ and putting them on-shell again, with the string remnant absorbing the remaining energy. Thus, we conserve energy and momentum after compression *and* fragmentation of the strings.

It should be mentioned that our choice of no p_L exchange does introduce a dependence on the frame in which the system is considered. This is due to the fact that while the light-cone momenta $W_\pm$ follow a simple rescaling under longitudinal boosts, the compression factors $f_{\pm i}$ depend non-linearly on $W_{\pm i}$ as seen in Eq. (16), complicating their transformations under such boosts. Specifically, compressing the strings then boosting the entire system results in a (marginally) different momentum topology than boosting the strings with the same boost factor and then compressing them. In this work unless otherwise stated, we compute compression factors in the overall CM frame of the two-string system. (A possible alternative, not pursued here, would be to boost the system longitudinally such that the centre of the overlap region is at $y = 0$.)

SciPost Physics Submission

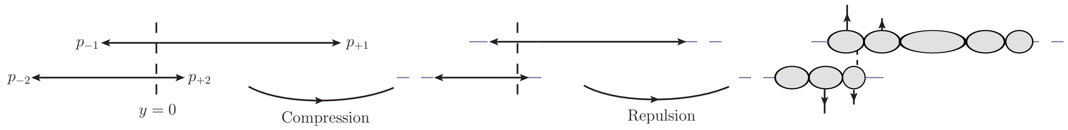

Figure 5: Schematic diagram of the general two-string configuration and how we perform the string compression using Eq. (16), and then the fragmentation repulsion. Only primary hadrons in the region of overlap will receive $p_\perp$ proportional to the string length taken. We have ignored the Gaussian transverse momentum generation in the Lund string model for the purposes of this figure.

4.2 Repulsion

The repulsion effect we seek to model is local; additional $p_\perp$ should be imparted to hadrons formed within regions of string overlap, and not to those outside. Fragmenting the (compressed) string from the outside in as usual, and using Eq. (3) to compute rapidity spans, we distinguish three cases for each produced hadron:

1. The span is completely outside the overlap region;
2. The span is completely inside the overlap region;
3. The span straddles the boundary of the overlap region.

In the first case, the hadron receives no repulsion $p_\perp$, while in the second, it is computed according to Eq. (9) and assigned repulsion $p_\perp$ following the same procedures as described in Sec. 3. In the last case, only the portion of the rapidity span inside the overlap region contributes to Eq. (9).

To illustrate the repulsion effect we consider a two-string scenario defined by the following endpoints (using the same lightcone notation as previously),

$$\begin{aligned} p_{+1} &= 1200\left(1, 0, \vec{0}_\perp\right)\ \text{GeV}, \\ p_{-1} &= \ \ 300\left(0, 1, \vec{0}_\perp\right)\ \text{GeV}, \\ p_{+2} &= \ \ 100\left(1, 0, \vec{0}_\perp\right)\ \text{GeV}, \\ p_{-2} &= 1000\left(0, 1, \vec{0}_\perp\right)\ \text{GeV}, \end{aligned} \tag{19}$$

This configuration is then boosted back to the overall CM frame. An illustration of the compression and repulsion steps for this type of configuration is given in Fig. 5.

4.3 Results

In Fig. 6, we show the average primary hadron $p_\perp$ distribution as a function of the string rapidity span taken by the hadron.

In the left panel of Fig. 6, the red histogram is the ordinary Lund model, which is agnostic to the the rapidity span taken by a hadron. The blue histograms are the result of our implemented model for $c_R = 0.2$ GeV, for both the repulsion component (dot-dashed), which matches the ansatz in Eq. (9), and the full fragmentation (solid), which matches the baseline Lund model and the repulsion component in the limits of small and large Δy respectively. Lastly, we have also included the results of using the shoving model for this configuration. These results are largely similar to the results for the symmetric, parallel configuration in Sec. 3.3.

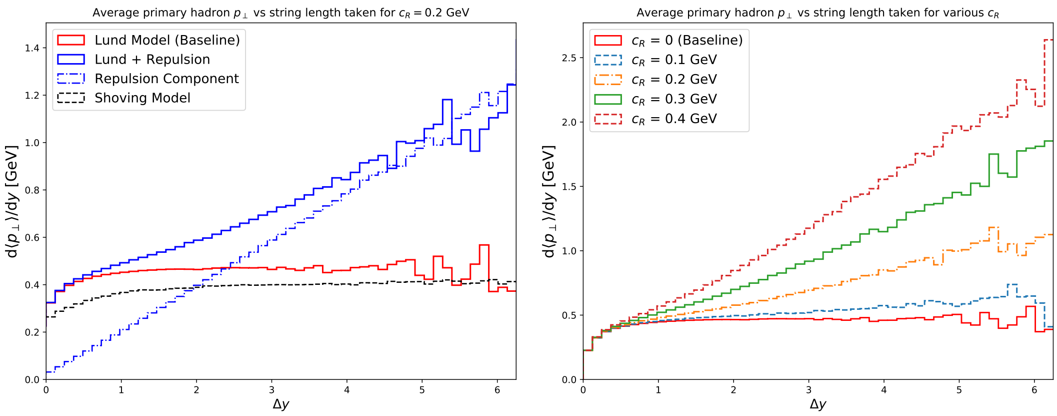

Figure 6: Distribution of average hadron $p_\perp$ for primary hadrons as a function of the rapidity span that they take, for the asymmetric two-string configuration discussed in the text. *Left*: the baseline Lund model (red solid) compared to our model of fragmentation repulsion (blue solid line). For the latter, the blue dot-dashed histogram illustrates the component which is due to repulsion. Also shown is the result of using the shoving model, which, like the baseline Lund model, is agnostic to the amount of string length taken. *Right*: the effect of varying c_R in Eq. (9).

The right panel of Fig. 6 highlights the effects of varying c_R on the average primary hadron $p_\perp$ distribution as a function of the string's rapidity span taken by the hadron for the full fragmentation repulsion. For $c_R = 0$ GeV, we reproduce the ordinary Lund model. As the repulsion factor increases, the slope of the average $p_\perp$ increases, since the two are proportional via Eq. (9).

In Fig. 7, we present the average primary hadron $p_\perp$ distribution as a function of the hadron's rapidity (as measured in the overall CM frame of the two strings). Since the configuration is asymmetric with respect to the endpoints of the two strings, the resultant compression and fragmentation repulsion will also reflect this asymmetry. The red histogram is the ordinary Lund string model, and again we reproduce the rapidity plateau, with a small asymmetry due to the configuration of strings. The blue histograms are our fragmentation repulsion for $c_R = 0.2$ GeV where we have shown only the repulsion component (dot-dashed), and the full fragmentation repulsion (solid). We have also included the results of the shoving model (black dashed).

Fig. 7 also showcases the considerations from Sec. 4.2. In comparison to Fig. 3 where the repulsion component has a sharp cut-off at the edges of the rapidity overlap region, in the general case we have longer tails that extend beyond the overlap region due to hadrons taking rapidity spans that are only partially in the overlap region.

Comparing Figs. 3 and 7, we see the same structures for each respective model. Our fragmentation repulsion exhibits an increased average $p_\perp$ for hadrons inside the rapidity overlap region, while hadrons outside that region have a diminished $p_\perp$ contribution from the repulsion. As in the previous section, we see that the shoving model considered in this study does not change the distribution, apart from minor deviations near the endpoints.

5 Two-String Systems with Relative Rotations and Boosts

We now consider string systems with endpoints that have non-vanishing transverse momenta. The examples we consider in this section will still be defined so that the z axis

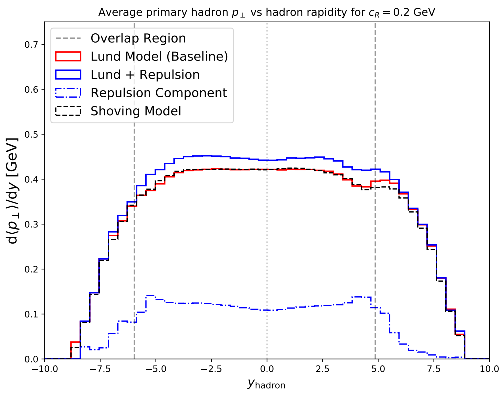

Figure 7: Distribution of average hadron $p_\perp$ for primary hadrons as a function of y_{hadron}, for the asymmetric two-string example described in the text. The repulsion component of our fragmentation repulsion increases the $\langle p_\perp \rangle$ in the region of overlap (indicated by the grey dashed lines, using $m_0 = 0.5$ GeV in the rapidity calculation).

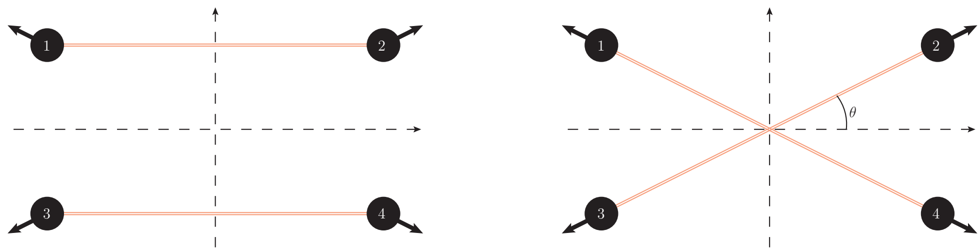

Figure 8: Schematic diagram of two string systems defined by the endpoint momenta given in Eq. (20), corresponding to (left) a relative boost and (right) a relative rotation.

remains a sensible choice of common rapidity axis. Specifically, we will consider systems like those illustrated in Fig. 8, with endpoint momenta (in conventional 4-momentum notation):

$$\begin{aligned}
p_1 &= E(\,1, \quad \sin\theta, \quad 0, \quad -\cos\theta\,)\,, \\
p_2 &= E(\,1, \quad \sin\theta, \quad 0, \quad \cos\theta\,)\,, \\
p_3 &= E(\,1, \quad -\sin\theta, \quad 0, \quad -\cos\theta\,)\,, \\
p_4 &= E(\,1, \quad -\sin\theta, \quad 0, \quad \cos\theta\,)\,,
\end{aligned} \tag{20}$$

so that the string systems defined by the (1,2) and (3,4) pairings are still parallel but each are transversely boosted relative to the overall CM, by $\beta = \pm \sin\theta$, while the systems defined by the pairings (1,4) and (2,3) are at rest relative to the overall CM but are rotated with respect to each other, with a relative opening angle of 2θ. In all cases, the CM energy is $E_{\mathrm{CM}} = 4E$. For definiteness we take $\sin\theta = 0.1$ in the examples below unless otherwise stated.

5.1 Symmetric configuration with relative boost

Taking the simplest symmetric two-string configuration, we ask what happens in the situation depicted in the left-hand panel of Fig. 8 in which both strings have some (equal and opposite) transverse momentum before compression.

Using the same arguments as above, we wish to convert a fraction of the original longitudinal momenta of the endpoints (defined along the common rapidity axis, here the

z axis) into transverse momentum instead of into potential energy of the string(s).

As before, the total amount of repulsion $p_\perp$ is determined from the effective rapidity overlap, which we compute from the longitudinal momentum components (along the chosen common axis) of the endpoints,

$$\Delta y_{\mathrm{ov}} = \min(y_{1+}, y_{2+}) - \max(y_{1-}, y_{2-}) \;, \tag{21}$$

where y_{i+} and y_{i-} refer to the rapidities of the right- and left-moving endpoints of string i respectively and we regulate the rapidity values of massless endpoints in the $p_\perp \to 0$ limit by imposing $m \geq m_0$ in the denominator of our rapidity definition:

$$y = \ln \frac{E + p_L}{\sqrt{m^2 + p_\perp^2}} \;. \tag{22}$$

Using lightcone coordinates as before, the longitudinal component of a general string-end momentum is $p_L = (W_+ - W_-)/2$, and the energy is $E = (W_+ + W_-)/2$.

The string-ends will be rescaled in a similar manner to the parallel strings in Sec. 3. Since the rescaling is done on the full 4-vectors, the string endpoints will lose some $p_\perp$. We use the ansatz of giving this extra transverse momentum reservoir, denoted $p_{\perp,\mathrm{res}}$ to the fragmenting hadrons as a fraction of the rapidity span they take from the string:

$$p_{\perp,\mathrm{h}} = \left(c_R + \frac{p_{\perp,\mathrm{res}}}{\Delta y_{\mathrm{ov}}} \right) \Delta y_h, \tag{23}$$

where Δy_{ov} is string-string overlap defined via Eq. (21, and Δy_h is the amount of rapidity span taken by the hadron inside of the overlap region, as discussed in Sec. 4. (Alternatively, and probably more correctly, one could distribute $p_{\perp,\mathrm{res}}$ among all the hadrons, not just those in the overlap region; or boosting the compressed string transversely so that it regains its original total $p_\perp$; but since since $p_{\perp,\mathrm{res}}$ is typically very small it is a minor effect.)

As in the previous section we assume no longitudinal momentum exchange, $\Delta p_{\mathrm{L}} = 0$. Writing the total longitudinal momentum of string $i \in [1, 2]$ as

$$p_{L,i} = p_{L,+i} + p_{L,-i} \;, \tag{24}$$

with $p_{L,\pm i}$ the longitudinal momentum of the respective endpoints, we can generalize Eq. (16) to:

$$f_{-i} = \frac{p_{L,i} + \sqrt{p_{L,i}^2 - 4 p_{L,-i} p_{L,+i} f_i^2}}{2 p_{L,-i}}. \tag{25}$$

In the limit of the string ends carrying $p_\perp \to 0$, Eq. (25) exactly reproduces Eq. (16).

The amount of repulsion $\perp$ given to each hadron during the fragmentation process should be proportional to the (overlapping portion of the) rapidity span it takes. The definition, Eq. (36), is given in terms of the quantities used to characterize the fragmentation of each string in its own CM frame, along the axis defined by its endpoints in that frame, whereas we here want to along the chosen common axis in the string-string CM frame. As a very simple way to "project" the rapidity span, we use

$$\Delta y_{\mathrm{eff}} = \frac{\Delta y_{\mathrm{string}}}{\Delta y^*_{\mathrm{string}}} \Delta y^*_{\mathrm{taken}} \;, \tag{26}$$

where the $\Delta y_{\mathrm{string}}$ is the rapidity span of the given string evaluated along the common axis defined in the string-string frame and $\Delta y^*_{\mathrm{string}} = \ln\left(W^2/m_0^2\right)$ is the (larger) span

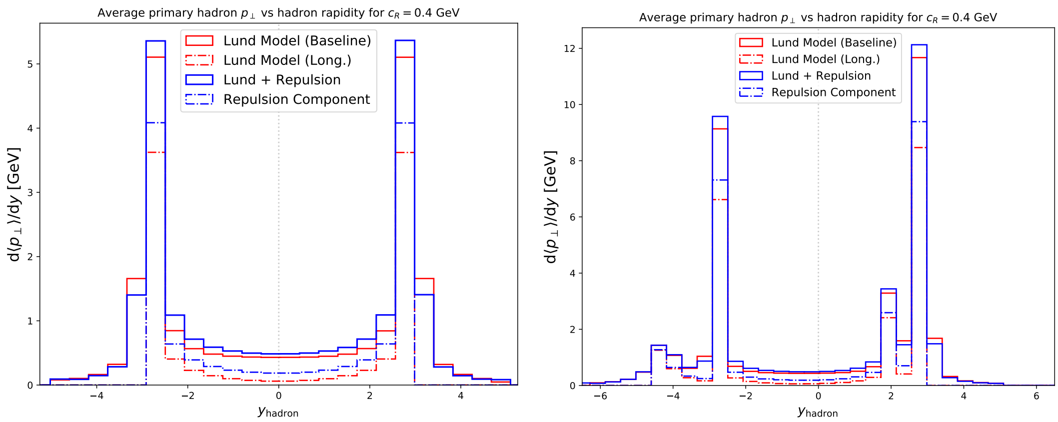

Figure 9: Distribution of average hadron $p_\perp$ of primary hadrons as a function of the hadron's rapidity, for the symmetric configuration (left) and the general configuration (right), where the two strings have an equal and opposite boost in the transverse direction. The latter configuration is boosted back to the two-string rest frame before compression and fragmentation. We have added the repulsion $p_\perp$ in the same direction as the overall motion of each string.

evaluated in the string's own rest frame. $\Delta y^*_{\mathrm{taken}} = \ln\left(W^2/W'^2\right)$ is the rapidity span of the hadron taken in the string's own rest frame.

The effective string length in Eq. (26) taken is invariant under longitudinal boosts, and reproduces the parallel configuration in the limit where each string endpoint carries vanishing $p_\perp$. Eq. (26) also sums to give the correct rapidity span along the z-axis, and is agnostic to the direction of the transverse momentum.

The last point to address is in which direction in azimuth to apply the repulsion. Considering the transverse plane only (in the string-string CM frame), the two systems will have some equal and opposite overall motion, which we denote by $\vec{p}_{\perp,\mathrm{rel}} = \vec{p}_{\perp 1} - \vec{p}_{\perp 2} = 2\vec{p}_{\perp 1}$. Assuming that, by the time strings are formed, the string systems are already separated a bit (on average) along this axis, it seems plausible to us to apply the repulsion $p_\perp$ along the same direction. To provide some variability and in order to have a well-defined repulsion axis also in the $p_{\perp,\mathrm{rel}}\ to 0$ limit, we add a random component as well:

$$\vec{n}_{\perp 1} = N(\vec{p}_{\perp,\mathrm{rel}} + \rho\vec{n}_{\perp,\mathrm{ran}}) \tag{27}$$

where $\vec{n}_{\perp,\mathrm{ran}}$ is a unit-vector in a randomly chosen azimuthal direction, the normalisation factor

$$N = \frac{1}{\sqrt{p^2_{\perp,\mathrm{rel}} + \rho^2 + 2\rho(\vec{p}_{\perp,\mathrm{rel}} \cdot \vec{n}_{\perp,\mathrm{ran}})}} \tag{28}$$

ensures $|n_{\perp 1}| = 1$, and ρ is a free parameter of order 1 GeV which governs the relative importance of the random component. The repulsion for string 1 is oriented *with* $n_{\perp 1}$, and that for string 2 in the opposite direction.

The choice of direction can have a significant effect on two-particle azimuthal correlations, as we will describe in Sec. 6, but it does not have a drastic effect at the level of the distributions for the average hadron transverse momentum versus hadron rapidity and rapidity span taken.

5.2 Results

We present the results in Fig. 9. Both panels show the average primary hadron $p_\perp$ as a function of y_{hadron} (defined along the common string-string axis, here the z axis, in their overall CM frame). In these plots we have chosen to add the repulsion $p_\perp$ in the same direction as each string's overall transverse motion, and chosen a larger value of $c_R = 0.4$ GeV compared to the parallel configurations, to make the effects of the repulsion stand out a bit more clearly against the $p_\perp$ contributed already from the endpoints.

In Fig. 9, our fragmentation repulsion exhibits similar effects as those seen in Figs. 3 and 7, though the enhancement of average primary hadron $p_\perp$ is less drastic than in the parallel configurations. The reason for this is twofold: first, since the strings are no longer parallel, the amount of rapidity overlap between the two strings is reduced, resulting in less total repulsion $p_\perp$. Second, the boosted endpoints show up as peaked structures around the endpoints' rapidity.

While the effects of our fragmentation repulsion are less distinctive in Fig. 9, the framework will still have a distinctive effect on the two-particle azimuthal correlations, as we will discuss in Sec. 6.

5.3 Asymmetric configurations

Generalizing to an arbitrary configuration with strings that have endpoints with transverse momentum follows naturally from combining the frameworks presented in Sec. 4 and Sec. 5.1. The effects are smaller than in the symmetric configuration with opposite boosts, since the overlap in rapidity along the z-axis decreases the more transversely boosted the endpoints are. This results in less compression, and less fragmentation repulsion. We will use the configuration from Eq. (19), with a boost factor of $\beta = 0.1$ in opposite directions for each string.

In the right panel of 9, we show the results of boosting each string in the general configuration given by Eq. (19) in opposite directions, then boosting back to their common rest frame, and then performing our compression and fragmentation repulsion. We have chosen to present the results of using $c_R = 0.4$ GeV since larger values of this parameter are required to have visible results for this observable. The results are in line with our expectations from previous sections, namely that strings with endpoints that have transverse components will compress and repel less than strings that are completely parallel, and similarly with strings that are not completely overlapping.

5.4 Rotated configurations

Configurations such as those depicted in the right-hand pane of Fig. 8 can be treated using the same arguments as for the boosted configurations. The endpoints again have non-vanishing transverse momenta, hence the rapidity spans computed along the common rapidity axis are always smaller than those in the respective string CM frames.

In the specific example shown in 8, $p_{\perp,\text{res}} = 0$ since each of the (1,4) and (2,3) strings have zero net $p_\perp$. Compression factors are computed from the longitudinal momentum components as in Eq. (25, and the effective span taken by each hadron is projected onto the common axis using Eq. (26).

Finally, since each of the strings are at rest the $\vec{p}_{\perp,\text{rel}}$ in Eq. (27) is zero hence the random component will dominate in the choice of azimuth direction. (A more physical choice could potentially be made by using the direction transverse to the plane spanned by the two strings, but since we consider the case of vanishing $\vec{p}_{\perp,\text{rel}}$ to be of limited general interest we do not pursue this further here.)

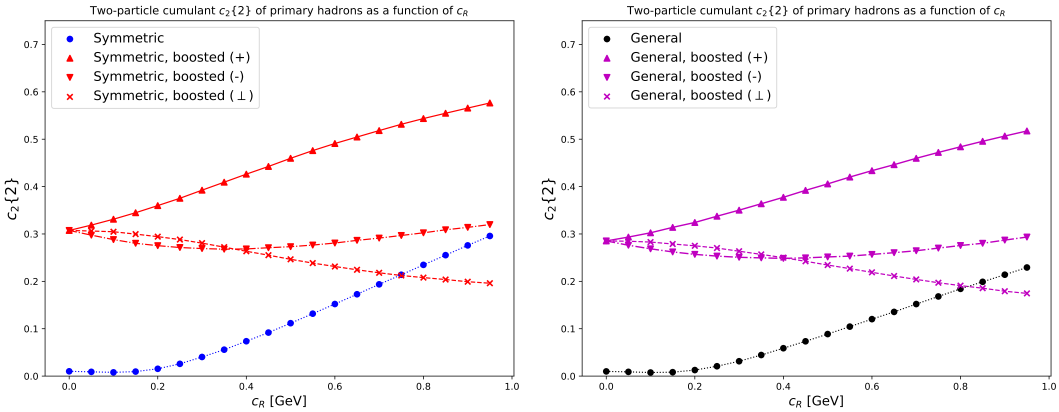

Figure 10: Two-particle cumulant for the symmetric (left panel) and the general (right panel) two-string configurations, at the level of primary hadron production. We show the curves for the simplest parallel two-string case, and three variations on the equal and oppositely boosted two-string case. The variations are: the repulsion $p_\perp$ acts in the same direction as the given string's overall transverse motion ("Boosted, (+)"), the repulsion $p_\perp$ acts in the opposite direction ("Boosted, $(-)$"), and lastly, the repulsion $p_\perp$ acts perpendicularly to the string's boost ("Boosted, $(\perp)$"). For each curve, when $c_R = 0$, we reproduce the baseline Lund string model.

There are many other configurations that one may consider, but with the four configurations discussed in this work, we have presented the overall framework for our model of fragmentation repulsion.

6 Flow and Cumulants for Two-String Configurations

Long-distance correlations in rapidity and azimuth have been used extensively to probe collective aspects of event structure, including flow, in both proton-proton and heavy-ion collisions. (See, e.g., [52] for a succinct review of elliptic flow in heavy-ion phenomenology, and references therein.) Here, we focus on just one such observable, the two-particle cumulant, $c_2\{2\}$, which is designed to suppress non-flow contributions. It is calculated as:

$$\begin{aligned} c_2\{2\} &= \left\langle \langle e^{2i(\phi_i - \phi_j)} \rangle \right\rangle, \\ &= \left\langle \frac{2}{n(n-1)} \sum_{i<j}^{n} \cos\left(2(\phi_i - \phi_j)\right) \right\rangle, \end{aligned} \tag{29}$$

where in the first line the outer angle bracket is the average over all events, and the inner is the average over all n particles in a given event. In the second line of Eq. (29), we have removed the self-correlations $i = j$, and used the fact that the cosine function is an even function.

The two-particle cumulant will depend not only on the repulsion strength c_R, but also on the direction of the repulsion, in particular for cases where the strings have an overall transverse motion such as the transversely boosted strings, where $\vec{v}_{\mathrm{det}} \neq 0$. In this work, we will simply show the three extreme cases of the repulsion directions for the transversely boosted configurations, as discussed in Sec. 5.2

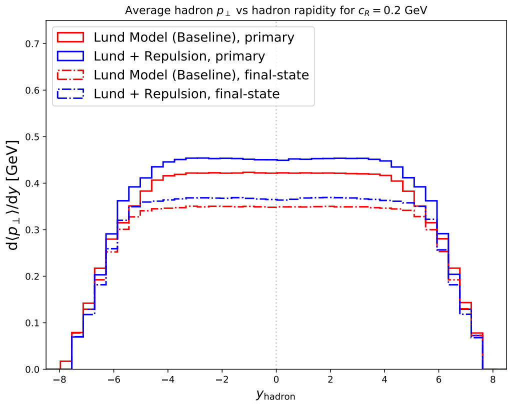

Figure 11: Illustration of the net reduction of average hadron $p_\perp$ caused by allowing excited primary hadrons (solid histograms) to decay (dot-dashed histograms), for the baseline Lund model (red) and our fragmentation repulsion model (blue). The example configuration is the symmetric parallel two-string configuration described in Sec. 3; the primary-hadron spectra are the same as those in Fig. 3.

In Fig. 10, we plot the results for the two-particle cumulant for the symmetric two-string configuration at the level of primary hadrons, as a function of the repulsion constant c_R. There are four curves in the plot. The first curve, labelled 'Symmetric' is the simplest two-string configuration, considered in Sec. 3. In this configuration, there is no preferred ϕ direction, and it takes larger values of the repulsion constant to overcome the Gaussian transverse momentum distribution of the Lund fragmentation model, and to have a significant effect on the cumulant.

The three other curves are variations on the configuration described in Sec. 5.1 where the two strings each have a boost of $\beta = 0.1$ in equal and opposite directions. The variations occur when one adds the repulsion $p_\perp$ to the primary hadrons during fragmentation. The curves are labelled according to the direction in which the repulsion $p_\perp$ is added with respect to the given string's overall boost direction. If we add the repulsion $p_\perp$ in the same direction as the string's motion, we can greatly enhance the two-particle cumulant. If instead we add it in the opposite direction, we at first reduce the two-particle cumulant, but as the repulsion gets larger, the cumulant begins to increase. Lastly, if we add the repulsion $p_\perp$ perpendicularly to the string's motion we greatly reduce the cumulant, but at large values of the repulsion constant, the rate of decrease begins to level out.

We obtain analogous results for the general configuration in the right panel of Fig. 10, though the cumulant for all values of c_R is less than for the symmetric case, due to the smaller overlap in rapidity.

We compared the symmetric parallel configuration in our fragmentation repulsion framework to the analogous configuration in the shoving model, and found that the two-particle cumulant is significantly smaller for the shoving model, at least with the parameter set described in App. B. For the shoving model, we calculated the two-particle cumulant to be $c_2\{2\} = 0.00957$ (averaged over 200,000 events), which is of the order of the baseline Lund model.

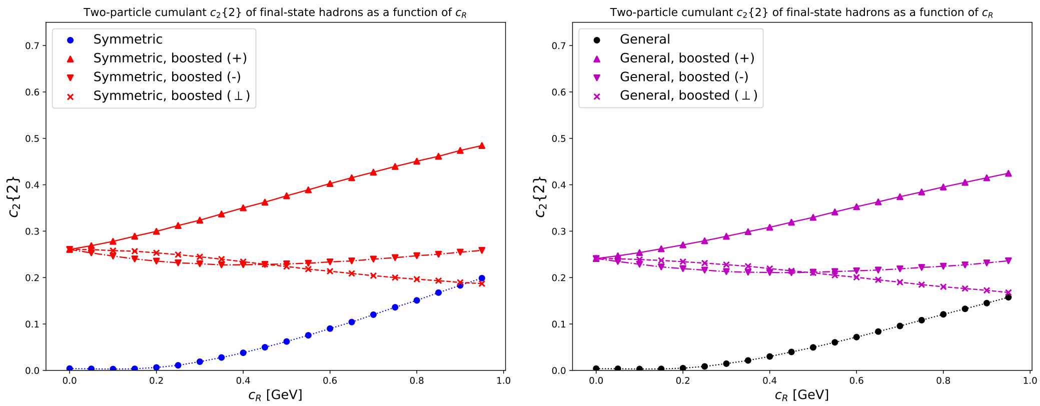

Figure 12: Two-particle cumulant for final-state hadrons in the symmetric configuration (left), and the general configuration (right), as a function of the repulsion constant c_R. Both plots exhibit the same trends as the primary hadron distributions in Fig. 10, though the correlations are slightly reduced, as expected from excited hadrons decaying isotropically into potentially non-hadronic final states.

7 Final-State Hadrons

In the previous sections, we considered the $p_\perp$ and rapidity distributions at the level of the primary hadrons produced in the fragmentation process. Decays of those hadrons into secondaries (via processes like $\rho \to \pi\pi$, $\pi^0 \to \gamma\gamma$, etc.) will smear the distributions in rapidity and dilute the $p_\perp$ enhancement per hadron. In this section, we include decays of all final-state particles with lifetimes shorter than $\tau = 10$ mm$/c$. In Pythia, this is done with the two switches: `ParticleDecays:limitTau0 = on`, and `ParticleDecays:tau0Max = 10`. With this criterion, weakly decaying strange hadrons are treated as stable, while all particles with shorter lifetimes are decayed. This matches the typical definition for stable particles used at LHC.

In Fig. 11, we present the average hadron $p_\perp$ distribution as a function of hadron rapidity, for the symmetric parallel configuration from Sec. 3. We replot the results for the baseline Lund model (red solid) and our fragmentation repulsion (blue solid) for primary hadrons. Allowing excited primary hadrons to decay produces the dot-dashed lines in Fig. 11, for the baseline Lund (red dot-dashed) and our fragmentation repulsion (blue dot-dashed).

As expected, the plateau has been lowered for the baseline Lund model, since excited primary hadrons can decay into non-hadronic final state particles, which remove some of the available $p_\perp$. Similarly, the fragmentation repulsion exhibits a lowering of its peak and general structure. However, the difference between the structure of the fragmentation repulsion and the rapidity plateau of the Lund model remains intact when decays are turned on, meaning our model can still be distinguished from the baseline Lund model.

In Fig. 12, we show the effects of varying the repulsion constant c_R on the two-particle azimuthal cumulant $c_2\{2\}$ of final-state hadrons, for the symmetric configurations (left) and the general configurations (right). As shown, the cumulant exhibits the same trends as the primary hadron counterparts in Fig. 10, though the effects have been somewhat reduced, due to the non-hadronic particles produced during particle decays.

The key result of allowing particle decays is that our fragmentation repulsion model, implemented at the level of the primary hadrons produced during string fragmentation, still retains its key signatures at the level of final-state hadrons, at least at the level of the

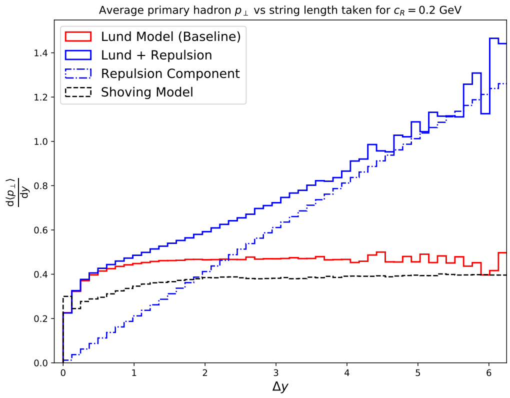

Figure 13: Distribution of average hadron $p_\perp$ for primary hadrons as a function of the rapidity span of the string taken by the hadron, for the symmetric, parallel two-string configuration with massive endpoints.

two-string configurations.

8 Strings With Massive Endpoints

The final generalisation we will consider in this work concerns strings with massive endpoints. The starting point for the compression process is the same as in the massless case, in that we rescale the 4-momenta as if the endpoints were massless:

$$p^\mu_\pm \to p'^\mu_\pm = f_\pm p^\mu_\pm, \tag{30}$$

where the subscript $\pm$ refers to the positively and negatively z-aligned endpoints respectively. The compression factors are, however, slightly modified relative to those in Eq. (12). Using the conservation of invariant mass:

$$\begin{aligned} W'^2 &= W^2 - p^2_{\perp,R}, \\ \text{thus} \quad (f_+p_+ + f_-p_-)^2 &= (p_+ + p_-)^2 - p^2_{\perp,R}, \end{aligned} \tag{31}$$

where we have inserted the original and rescaled endpoint momenta in the second line.

Expanding Eq. (31) and rearranging gives:

$$(1 - f^2_+)m^2_+ + (1 - f^2_-)m^2_- + 2p_+ \cdot p_- - p^2_{\perp,R} = 2f_+f_-p_+ \cdot p_-. \tag{32}$$

Using the longitudinal momentum conservation to remove, e.g., f_+ produces a quadratic in f_- which can be simply solved to calculate the two compression factors.

After calculating the new momenta for the endpoints in the manner described above, we put the endpoints back on shell:

$$E'_\pm = \sqrt{m^2_\pm + \vec{p}'^2_\pm} = \sqrt{m^2_\pm + f^2_\pm \vec{p}^2_\pm} \le E_\pm, \tag{33}$$

where the last inequality of Eq. (33) emphasises the fact that $f_\pm$ are indeed compression factors. With Eqs. (32, 33), we now have a prescription for compressing strings with massive endpoints. The repulsion part is the same as that described in Secs. 3.2 and 5.3.

In Fig. 13, we present the results of our fragmentation repulsion model for the symmetric, parallel two-string configuration with massive endpoints. As expected, Fig. 13

reproduces the same characteristics as Fig. 2, and in particular, the significant difference between the shoving model and the Lund model with our fragmentation repulsion remains.

Lastly, with the above prescription for handling symmetric, parallel strings with massive endpoints, we can extend this formalism to the general two-string configuration using the frameworks of this section and Sec. 5.3. A full presentation of this and an extension to strings with gluon kinks will be discussed in future work.

9 Conclusion and Outlook

We have presented a framework to compress two simple $q\bar{q}$ strings and repel them at the level of string fragmentation, a model we call fragmentation repulsion. We have shown that this induces an increased average $p_\perp$ per hadron in regions of string overlaps and that this in turn generates non-trivial two-particle azimuthal correlations.

With the configurations presented, one may begin to build up the more complicated string topologies from the smaller pieces we have considered. Future work will look first at strings with gluon kinks, then at configurations with more than two overlapping strings. More complicated string topologies such as junctions and closed gluon loops will also need to be addressed to turn the model into a full-fledged description of LHC events.

A shortcoming of our work is that it does not provide a microscopic description of the string-string interactions, unlike the shoving model. That is, we describe the effect simply in terms of an effective average $p_\perp$ density that we postulate is accumulated by strings that overlap in rapidity, and which is transferred to the hadrons that are produced in the overlapping regions. Despite its relative simplicity, the model exhibits distinctive signatures in both average hadron transverse momentum and two-particle azimuthal correlations which are easy to understand intuitively. The amount of repulsion generated via Eq. (5) is longitudinally boost invariant, but there remains some frame dependence — and associated ambiguities — in our choices of rapidity and repulsion axes, and in the definition of the compression procedure. We aim to study these aspects further in future work.

We round off by noting that, since the cluster hadronization model is based on simple $q\bar{q}$ systems not unlike those considered here, it might be possible to apply our model also in the context of the cluster model, to let clusters repel off one another while losing some longitudinal momentum. However, since a cluster undergoes fissioning and decay, the repulsion would need to be split between the two products in the respective processes.

Acknowledgements

We thank Gösta Gustafson for his valuable comments on the work, Christian Bierlich for his helpful comments about the current implementation of the shoving model in Pythia 8.2, and Helen Brooks & Johannes Bellm for discussions of our work. CBD is supported by the Australian Government Research Training Program Scholarship and the J. L. William Scholarship. This work was funded in part by the Australian Research Council via Discovery Project DP170100708 – “Emergent Phenomena in Quantum Chromodynamics” – and in part by the European Union’s Horizon 2020 research and innovation programme under the Marie Skłodowska-Curie grant agreement No 722105 – MCnetITN3.

References

[1] B. Andersson, G. Gustafson, G. Ingelman and T. Sjöstrand, *Parton Fragmentation and String Dynamics*, Phys. Rept. **97**, 31 (1983), doi:10.1016/0370-1573(83)90080-7.

[2] B. Andersson, G. Gustafson and B. Soderberg, *A General Model for Jet Fragmentation*, Z. Phys. **C20**, 317 (1983), doi:10.1007/BF01407824.

[3] B. Andersson, *The Lund model*, Camb. Monogr. Part. Phys. Nucl. Phys. Cosmol. **7**, 1 (1997).

[4] T. Sjöstrand, *Jet fragmentation of multiparton configurations in a string framework*, Nuclear Physics B **248**(2), 469 (1984), doi:https://doi.org/10.1016/0550-3213(84)90607-2.

[5] R. D. Field and S. Wolfram, *A QCD model for e^+e^- annihilation*, Nuclear Physics B **213**(1), 65 (1983), doi:https://doi.org/10.1016/0550-3213(83)90175-X.

[6] T. D. Gottschalk, *An improved description of hadronization in the QCD cluster model for e^+e^- annihilation*, Nuclear Physics B **239**(2), 349 (1984), doi:https://doi.org/10.1016/0550-3213(84)90253-0.

[7] B. Webber, *A QCD model for jet fragmentation including soft gluon interference*, Nuclear Physics B **238**(3), 492 (1984), doi:http://dx.doi.org/10.1016/0550-3213(84)90333-X.

[8] T. Sjöstrand, S. Mrenna and P. Z. Skands, *PYTHIA 6.4 Physics and Manual*, JHEP **05**, 026 (2006), doi:10.1088/1126-6708/2006/05/026, `hep-ph/0603175`.

[9] T. Sjöstrand, S. Mrenna and P. Z. Skands, *A Brief Introduction to PYTHIA 8.1*, Comput. Phys. Commun. **178**, 852 (2008), doi:10.1016/j.cpc.2008.01.036, `0710.3820`.

[10] T. Sjöstrand, S. Ask, J. R. Christiansen, R. Corke, N. Desai, P. Ilten, S. Mrenna, S. Prestel, C. O. Rasmussen and P. Z. Skands, *An Introduction to PYTHIA 8.2*, Comput. Phys. Commun. **191**, 159 (2015), doi:10.1016/j.cpc.2015.01.024, `1410.3012`.

[11] K. Werner, F.-M. Liu and T. Pierog, *Parton ladder splitting and the rapidity dependence of transverse momentum spectra in deuteron-gold collisions at RHIC*, Phys. Rev. **C74**, 044902 (2006), doi:10.1103/PhysRevC.74.044902, `hep-ph/0506232`.

[12] T. Pierog, I. Karpenko, J. M. Katzy, E. Yatsenko and K. Werner, *EPOS LHC: Test of collective hadronization with data measured at the CERN Large Hadron Collider*, Phys. Rev. **C92**(3), 034906 (2015), doi:10.1103/PhysRevC.92.034906, `1306.0121`.

[13] M. Bähr *et al.*, *Herwig++ Physics and Manual*, Eur. Phys. J. **C58**, 639 (2008), doi:10.1140/epjc/s10052-008-0798-9, `0803.0883`.

[14] J. Bellm *et al.*, *Herwig 7.0/Herwig++ 3.0 release note*, Eur. Phys. J. **C76**(4), 196 (2016), doi:10.1140/epjc/s10052-016-4018-8, `1512.01178`.

[15] J. Bellm *et al.*, *Herwig 7.1 Release Note* (2017), `1705.06919`.

[16] T. Gleisberg, S. Hoeche, F. Krauss, M. Schönherr, S. Schumann, F. Siegert and J. Winter, *Event generation with SHERPA 1.1*, JHEP **02**, 007 (2009), doi:10.1088/1126-6708/2009/02/007, `0811.4622`.

[17] E. Bothmann *et al.*, *Event Generation with Sherpa 2.2*, SciPost Phys. **7**, 034 (2019), doi:10.21468/SciPostPhys.7.3.034, 1905.09127.

[18] A. Karneyeu, L. Mijovic, S. Prestel and P. Z. Skands, *MCPLOTS: a particle physics resource based on volunteer computing*, Eur. Phys. J. **C74**, 2714 (2014), doi:10.1140/epjc/s10052-014-2714-9, 1306.3436.

[19] J. Adam *et al.*, *Measurement of pion, kaon and proton production in proton–proton collisions at $\sqrt{s} = 7$ TeV*, Eur. Phys. J. **C75**(5), 226 (2015), doi:10.1140/epjc/s10052-015-3422-9, 1504.00024.

[20] S. Acharya *et al.*, *Multiplicity dependence of light-flavor hadron production in pp collisions at $\sqrt{s} = 7$ TeV*, Phys. Rev. **C99**(2), 024906 (2019), doi:10.1103/PhysRevC.99.024906, 1807.11321.

[21] V. Khachatryan *et al.*, *Observation of Long-Range Near-Side Angular Correlations in Proton-Proton Collisions at the LHC*, JHEP **09**, 091 (2010), doi:10.1007/JHEP09(2010)091, 1009.4122.

[22] D. Velicanu, *Ridge correlation structure in high multiplicity pp collisions with CMS*, J. Phys. **G38**, 124051 (2011), doi:10.1088/0954-3899/38/12/124051, 1107.2196.

[23] G. Aad *et al.*, *Observation of Long-Range Elliptic Azimuthal Anisotropies in $\sqrt{s}$ =13 and 2.76 TeV pp Collisions with the ATLAS Detector*, Phys. Rev. Lett. **116**(17), 172301 (2016), doi:10.1103/PhysRevLett.116.172301, 1509.04776.

[24] V. Khachatryan *et al.*, *Measurement of long-range near-side two-particle angular correlations in pp collisions at $\sqrt{s}$ =13 TeV*, Phys. Rev. Lett. **116**(17), 172302 (2016), doi:10.1103/PhysRevLett.116.172302, 1510.03068.

[25] V. Khachatryan *et al.*, *Evidence for collectivity in pp collisions at the LHC*, Phys. Lett. **B765**, 193 (2017), doi:10.1016/j.physletb.2016.12.009, 1606.06198.

[26] M. Aaboud *et al.*, *Measurements of long-range azimuthal anisotropies and associated Fourier coefficients for pp collisions at $\sqrt{s} = 5.02$ and 13 TeV and p+Pb collisions at $\sqrt{s_{\mathrm{NN}}} = 5.02$ TeV with the ATLAS detector*, Phys. Rev. **C96**(2), 024908 (2017), doi:10.1103/PhysRevC.96.024908, 1609.06213.

[27] M. Aaboud *et al.*, *Measurement of multi-particle azimuthal correlations in pp, p+Pb and low-multiplicity Pb+Pb collisions with the ATLAS detector*, Eur. Phys. J. **C77**(6), 428 (2017), doi:10.1140/epjc/s10052-017-4988-1, 1705.04176.

[28] S. Chatrchyan *et al.*, *Measurement of Neutral Strange Particle Production in the Underlying Event in Proton-Proton Collisions at $\sqrt{s} = 7$ TeV*, Phys. Rev. **D88**, 052001 (2013), doi:10.1103/PhysRevD.88.052001, 1305.6016.

[29] G. Aad *et al.*, *Measurement of K^0_S and Λ^0 production in $t\bar{t}$ dileptonic events in pp collisions at $\sqrt{s} = 7$ TeV with the ATLAS detector* (2019), 1907.10862.

[30] P. Cui, *Strangeness Production in Jets and Underlying Events in pp Collisions at $\sqrt{s}$ = 13 TeV with ALICE* (2019), 1909.05471.

[31] T. Sjöstrand, *Colour Reconnections from LEP to Future Colliders*, In *Proceedings, Parton Radiation and Fragmentation from LHC to FCC-ee: CERN, Geneva, Switzerland, November 22-23, 2016, arXiv:1702.01329*, pp. 144–148 (2017).

[32] C. Bierlich, G. Gustafson, L. Lönnblad and A. Tarasov, *Effects of Overlapping Strings in pp Collisions*, JHEP **03**, 148 (2015), doi:10.1007/JHEP03(2015)148, 1412.6259.

[33] C. Bierlich and J. R. Christiansen, *Effects of color reconnection on hadron flavor observables*, Phys. Rev. **D92**(9), 094010 (2015), doi:10.1103/PhysRevD.92.094010, 1507.02091.

[34] J. Ambjørn, P. Olesen and C. Peterson, *Stochastic confinement and dimensional reduction (ii). three-dimensional su(2) lattice gauge theory*, Nuclear Physics B **240**(4), 533 (1984), doi:https://doi.org/10.1016/0550-3213(84)90242-6.

[35] G. S. Bali, *Casimir scaling of SU(3) static potentials*, Phys. Rev. **D62**, 114503 (2000), doi:10.1103/PhysRevD.62.114503, hep-lat/0006022.

[36] C. Bierlich, G. Gustafson and L. Lönnblad, *A shoving model for collectivity in hadronic collisions* (2016), 1612.05132.

[37] C. Bierlich, G. Gustafson and L. Lönnblad, *Collectivity without plasma in hadronic collisions*, Phys. Lett. **B779**, 58 (2018), doi:10.1016/j.physletb.2018.01.069, 1710.09725.

[38] C. Flensburg, G. Gustafson and L. Lönnblad, *Inclusive and Exclusive Observables from Dipoles in High Energy Collisions*, JHEP **08**, 103 (2011), doi:10.1007/JHEP08(2011)103, 1103.4321.

[39] C. Bierlich, G. Gustafson, L. Lönnblad and H. Shah, *The Angantyr model for Heavy-Ion Collisions in PYTHIA8*, JHEP **10**, 134 (2018), doi:10.1007/JHEP10(2018)134, 1806.10820.

[40] A. Ortiz Velasquez, P. Christiansen, E. Cuautle Flores, I. Maldonado Cervantes and G. Paić, *Color Reconnection and Flowlike Patterns in pp Collisions*, Phys. Rev. Lett. **111**(4), 042001 (2013), doi:10.1103/PhysRevLett.111.042001, 1303.6326.

[41] J. R. Christiansen and P. Z. Skands, *String Formation Beyond Leading Colour*, JHEP **08**, 003 (2015), doi:10.1007/JHEP08(2015)003, 1505.01681.

[42] N. Fischer and T. Sjöstrand, *Thermodynamical String Fragmentation*, JHEP **01**, 140 (2017), doi:10.1007/JHEP01(2017)140, 1610.09818.

[43] S. Gieseke, P. Kirchgaeßer, S. Plätzer and A. Siodmok, *Colour Reconnection from Soft Gluon Evolution*, JHEP **11**, 149 (2018), doi:10.1007/JHEP11(2018)149, 1808.06770.

[44] C. B. Duncan and P. Kirchgaeßer, *Kinematic strangeness production in cluster hadronization*, Eur. Phys. J. **C79**(1), 61 (2019), doi:10.1140/epjc/s10052-019-6573-2, 1811.10336.

[45] S. Ferreres-Solé and T. Sjöstrand, *The space–time structure of hadronization in the Lund model*, Eur. Phys. J. **C78**(11), 983 (2018), doi:10.1140/epjc/s10052-018-6459-8, 1808.04619.

[46] J. S. Schwinger, *On gauge invariance and vacuum polarization*, Phys. Rev. **82**, 664 (1951), doi:10.1103/PhysRev.82.664.

[47] P. Skands, S. Carrazza and J. Rojo, *Tuning PYTHIA 8.1: the Monash 2013 Tune*, Eur. Phys. J. **C74**(8), 3024 (2014), doi:10.1140/epjc/s10052-014-3024-y, 1404.5630.

[48] S. Amoroso, S. Caron, A. Jueid, R. Ruiz de Austri and P. Skands, *Estimating QCD uncertainties in Monte Carlo event generators for gamma-ray dark matter searches*, JCAP **1905**(05), 007 (2019), doi:10.1088/1475-7516/2019/05/007, 1812.07424.

[49] L. Kramer, *Thermodynamic Behavior of Type-II Superconductors with Small κ near the Lower Critical Field*, Phys. Rev. B **3**, 3821 (1971), doi:10.1103/PhysRevB.3.3821.

[50] A. Chaves, F. M. Peeters, G. A. Farias and M. V. Milošević, *Vortex-vortex interaction in bulk superconductors: Ginzburg-landau theory*, Phys. Rev. B **83**, 054516 (2011), doi:10.1103/PhysRevB.83.054516.

[51] J. Bellm, C. B. Duncan, S. Gieseke, M. Myska and A. Siódmok, *Space-time colour reconnection in Herwig 7*, Eur. Phys. J. **C79**(12), 1003 (2019), doi:10.1140/epjc/s10052-019-7533-6, 1909.08850.

[52] R. Snellings, *Elliptic Flow: A Brief Review*, New J. Phys. **13**, 055008 (2011), doi:10.1088/1367-2630/13/5/055008, 1102.3010.

A String Fragmentation in Pythia

The Lund string fragments probabilistically by taking steps along the lightcone momenta $W_\pm$, where $W_+W_- = W^2$. A hadron is created by taking a fraction z_h of a given end's lightcone momentum and the rest of the string keeps $1 - z_h$ of the lightcone momentum. In order to put the hadron on shell, we also need to take some lightcone momentum from the other end.

Following the notational convention of [4], if we have taken i iterative steps in the fragmentation process, producing $q_i\bar{q}_i$ pairs, each of which take a fraction z_i, and $0 \leq z_i \leq 1$, we can write the fractions of the initial total $W_\pm$ taken at each step:

$$\begin{aligned} x_{+,i} &= z_i \prod_{j=1}^{i-1} (1 - z_j)\,, \\ \text{and}\ \ x_{-,i} &= \frac{m_{\perp,i}^2}{x_{+,i}W^2}, \\ \text{since}\ \ m_{\perp,i}^2 &= x_{+,i}x_{-,i}W^2, \end{aligned} \tag{34}$$

where we have assumed without loss of generality that the hadrons have been fragmenting from the W_+ end of the string.

Since the string can fragment from either end of the string, Pythia needs two sets of these $x_\pm$ pairs, where now the $\pm$ sign refers to the lightcone momenta of the opposite end of the given fragmenting end. We will label them x and $\tilde{x}$. These two pairs track how much has been taken from the two end points in the two different directions, and the differences are the amount of lightcone momentum actually left:

$$\bar{x}_{\text{tot},+} = x_+ - \tilde{x}_-, \text{and } \bar{x}_{\text{tot},-} = \tilde{x}_+ - x_-, \tag{35}$$

Using Eq. (3), we can now calculate the rapidity span of the string that a fragmenting hadron i takes with it:

$$\Delta y = \ln\left(\frac{\bar{x}_{\text{tot},+}\bar{x}_{\text{tot},-}}{(\bar{x}_{\text{tot},+} - x_{h,+})(\bar{x}_{\text{tot},-} - x_{h,-})}\right), \tag{36}$$

where $x_{h,\pm}$ is the lightcone momentum fraction taken by a new hadron fragmentation from the positive end and negative end respectively.

At some cutoff invariant mass W^2_{stop}, this fragmentation process stops, and the remnant string is broken into two final hadrons.

B Shoving Model Parameters

In the shoving model (as implemented in Pythia 8.2), there are several parameters that govern the rate and amount of shoving. We summarise the parameter values we used to produce Fig. 3 in Tab. 1. We did not include the flavour changing aspects of the Rope model.

Parameter	Value
`Ropewalk:rCutOff`	10.0
`Ropewalk:limitMom`	on
`Ropewalk:pTcut`	2.0
`Ropewalk:r0`	0.41
`Ropewalk:m0`	0.2
`Ropewalk:gAmplitude`	10.0
`Ropewalk:gExponent`	1.0
`Ropewalk:deltat`	0.1
`Ropewalk:tShove`	1.0
`Ropewalk:deltay`	0.1
`Ropewalk:tInit`	1.5

Table 1: Input parameters used in Fig. 3 for the shoving model.

We also set the two strings' endpoints to have $m_u = 0.33$ GeV, though this configuration and our massless endpoint configuration were set to have the same total invariant mass for each string. Since the shoving model also requires partons to have transverse spacetime coordinates, we set the strings to be 2.46 fm apart in transverse space (six times the input parameter `Ropewalk:r0`). We chose to set the strings relatively far apart, relative to the transverse radius of the string, since we discovered that for the above parameter set, a transverse separation between our two straight strings of $d_\perp < 5r_0$ lead to, in our opinion, pathological results. To understand what each parameter governs in the model, we direct the reader to [37].

6.2 Errata for *Fragmentation of Two Repelling Lund Strings*

1. In the third paragraph of §2 - Lund String Model, the final sentence should read: *"In the ordinary Lund string model, each string fragments independently, unaware of the environment around them."*

2. In the first paragraph of §3.2 - Repulsion, the sentence: *"Using Eq. (36), a hadron receives a corresponding fraction of ..."* has a typographical error. This sentence should read: *"Using Eq. (**3**), a hadron receives a corresponding fraction of ..."* where the boldface type indicates the change.

3. In the final paragraph of §3.2 - Repulsion, the amount of transverse momentum given to the string remnant is implemented as:

$$p_{\perp,R}^{(\mathrm{rem})} = p_{\perp,R} - \sum_h p_{\perp,R}^{(h)}, \tag{6.2}$$

namely the total repulsion transverse momentum calculated previously minus the sum of repulsion transverse momentum taken by the earlier produced hadrons $p_{\perp,R}^{(h)}$. This is equivalent to calculating it as:

$$p_{\perp,R}^{(\mathrm{rem})} = \frac{\Delta y_{\mathrm{rem}}}{\Delta y_{\mathrm{string}}} p_{\perp,R}, \tag{6.3}$$

where Δy_{rem} and $\Delta y_{\mathrm{string}}$ are the rapidities spans of the string remnant, and the string before any fragmentations occur respectively.

4. In §3.3 - Results, the second paragraph has a typographical error: *"The red dashed histogram shows ..."*. This sentence should read: *"The red **solid** histogram ..."* where the boldface indicates the change.

5. In Fig. (3), the final clause: *"Right: the effect that varying the repulsion strength C_R"* has a typographical error. The sentence should read: *"Right: the effect **of** varying the repulsion strength C_R"* where boldface indicates the change.

6. In §5.1, in the sixth paragraph, the sentences: *"The amount of repulsion $\perp$ given to each hadron during the fragmentation process should be proportional to the (over-*

lapping portion of the) rapidity span it takes. The definition, Eq. (36), is given in terms of the quantities used to characterize the fragmentation of each string in its own CM frame, along the axis defined by its endpoints in that frame, whereas we here want to along the chosen common axis in the string-string CM frame." have typographical errors. The correct sentences should read: *"The amount of repulsion* $\mathbf{p}_\perp$ *given to each hadron during the fragmentation process should be proportional to the (overlapping portion of the) rapidity span it takes. The definition, Eq. **(3)**, is given in terms of the quantities used to characterize the fragmentation of each string in its own CM frame, along the axis defined by its endpoints in that frame. **We instead want to consider the chosen common axis defined in the string-string CM frame.**"* where boldface indicates the changes.

7. In §5.1, in the seventh paragraph, the sentence immediately before Eq. (27): *"To provide some variability and in order to have a well-defined repulsion axis also in the* $p_{\perp,rel}$ *to0 limit, we add a random component as well:"* has a typographical error. The sentence should read: *"To provide some variability and in order to have a well-defined repulsion axis also in the* $\mathbf{p_{\perp,rel}} \rightarrow \mathbf{0}$ *limit, we add a random component as well:"* where boldface indicates the change.

8. In §5.4, in the second paragraph, the sentences: *"In the specific example shown in 8,* $p_{\perp,res} = 0$ *since each of the (1,4) and (2,3) strings have zero net* $p_\perp$*. Compression factors are computed from the longitudinal momentum components as in Eq. (25, ..."* have typographical errors. The sentences should read: *"In the specific example shown in **Fig. (8)**,* $p_{\perp,res} = 0$ *since each of the (1,4) and (2,3) strings have zero net* $p_\perp$*. Compression factors are computed from the longitudinal momentum components as in Eq. (25**)**, ..."* where boldface indicates the changes.

9. In §8 - Strings with Massive Endpoints, as well as in Fig. (13), the masses of the endpoints was not quoted. The masses used in the plot and the study were the constituent mass of the up quark - 330 MeV.

10. In Appendix A, the paragraph between Eq. (34) and Eq. (35) is somewhat unclear. The paragraph should read: *"In the Pythia implementation of the string model, the string probabilistically fragments from either endpoint. As such, Pythia keeps track of the lightcone momenta available for either endpoint. We will label the*

lightcone momenta of the positive rapidity endpoint as x*, and that of the negative rapidity endpoint as* $\tilde{x}$*. These lightcone momenta each have two components - the endpoint's relative positive and negative lightcone momenta, denoted by subscripts* $\pm$*. The amount of lightcone momentum left at any point during the fragmentation process is given by:"*

7

Conclusion

The work presented in this thesis has been focused on Monte Carlo event generators and the development of novel extensions to the non-perturbative regime of high-energy collision simulation. Monte Carlo event generators are a key part of testing our understanding of the physical processes involved in collisions, not only to deepen our knowledge of the Standard Model, but also to better model the background processes that dominate in colliders.

The foundations of QCD, and the various physical processes modelled in Monte Carlo event generators were reviewed in Chap. 2, highlighting the place hadronization has in overall high-energy modelling. In Chap. 3, the two major models of hadronization have been reviewed, comparing and contrasting the Lund string model and the cluster model, as well as the shortcomings of the current models to describe recent data. These chapters form the background for this thesis and the published work presented in the following chapters.

In Chap. 4, the non-perturbative strangeness production in Herwig 7 was first studied and retuned. Building on the work started in [219], we quantify the data-preferred relative rates during the three main stages of evolution in the cluster model: gluon splitting, cluster fission, and cluster decay. The strangeness weight was modified to depend on the invariant mass of the respective colour singlet breaking apart during these stages. Performing a retuning to e^+e^- and LHC data, we showed a better agreement between the two environments. The code has been implemented and made public in Herwig 7.2.

We build a framework to introduce spacetime coordinates to the Monte Carlo event generator Herwig 7 in Chap. 5, though our considerations are easily translatable and implementable in other event generators. We show that the spacetime coordinates are predominately affected by the multiple parton interactions stage and at the end of the parton shower, where the softest partons are produced. These spacetime coordinates are used to govern the baryonic colour reconnection probability for the cluster model. Comparing the model again to minimum-bias data from the LHC showed reasonable agreement, though diffractive events still need to be better understood from, among other ones, a spacetime perspective. This code will be implemented in a future release of Herwig 7.

Switching focus from the cluster model to the Lund string model, Chap. 6 presents a model that builds on the Lund string fragmentation model. In the standard Lund model, string fragmentation is independent of any other strings in the event, and uses a Gaussian distribution to impart non-perturbative transverse momentum to the primary hadrons. In our model, two strings overlapping in rapidity compress and repel off each other at the level of string fragmentation, circumventing the need to perform microscopic (and time consuming) gluon kicks to the entire string. The model is developed to handle any two-string configuration, from parallel strings, to transversely boosted ones, to finally rotated ones. We show that with our framework, one can introduce significant two-particle azimuthal correlations, a clear sign of collective effects in proton-proton collisions. One issue remains at hand: to extend this model to more complicated string topologies and to multiple strings. The code will be made public in a future release of Pythia 8.

Event generators offer a means to explore our understanding of QCD, and to rigorously test it against experimental data. As parton showers and hard process generation improve in precision, it becomes a pressing issue to investigate the deficiencies in contemporary hadronization models. In the absence of first-principles guiding lights, hadronization phenomenology plays a vital role of mapping coloured partons produced from parton showers and multiple parton interactions onto the hadrons detected by experiments. No matter the type of potential future collider built, processes involving QCD will be present in at least the final state of the event, and having increasingly sophisticated models will be important to finding any new physics, either from beyond the Standard Model, or from unknown aspects of QCD.

As the era of the firewall between the high-energy and heavy-ion communities is coming to a hopeful end, testing the physics and event generators developed in each field against the other will be an extremely active area of research. It will allow physicists to begin to understand the transition from one regime to the other, but to do so, we need to build up the relevant frameworks. As an example, Chap. 5 aims to not only improve our understanding of the relevance of spacetime coordinates in proton-proton collisions, but also to allow future research into applying Herwig to heavy-ion collisions.

Potential Future Work

Event generators are constantly evolving and undergoing new developments in order to better match the unprecedented levels of data being published by the various experiments at the LHC. With regards to innovation in the hadronization and soft-physics community, there are several directions that the work in this thesis would underpin. Better understanding the non-perturbative strangeness production mechanisms remains a vital ingredient to improving event generators' predictions for species-specific hadron-level observables. Similarly, baryon production is still poorly modelled in both the Lund string and cluster models, particularly with respect to (anti-)baryon-(anti-)baryon azimuthal correlations, as reported in [32].

With the spacetime coordinates framework in place for event generation in Herwig, one will be readily able to build a heavy-ion event generator to comprehensively test the QCD modeling in Herwig in a new environment. Testing the performance of general-purpose Monte Carlo event generators against established heavy-ion event generators, which typically use the drastically different paradigm of relativistic hydrodynamics, is an important step in gaining a better insight into how QCD behaves at different scales and in different environments.

In a similar vein, one potential avenue of research could be to develop novel MPI models that incorporate more transverse-space considerations, such as the gluonic hot spots model in [247], as well as studying their ability to quantitatively describe and generate collective effects in high-multiplicity events. It is also imperative to simultaneously test and improve the modelling of the colour structures created from the MPI generation, since this colour topology sets the initial framework for any later colour reconnections between strings/clusters or colour connections between partons.

Cluster-based Monte Carlo event generators do not currently have any interactions between the clusters, other than a simple rearrangement of the constituents via colour reconnection. The interacting strings framework presented in Chap. 6 focuses on simple $q\bar{q}$ strings which are analogous to clusters, resulting in a highly transferable model. Testing this model in the cluster hadronization framework would give a real insight into whether the correlations seen in the published work are still observable in real, high-multiplicity events. It is also important to continue the interacting strings model in the Lund string framework and build a fully-fledged phenomenological model, that incorporates more of the rich physics of the string structures mentioned in Sec. 3.2.3, in order to test it against LHC data.

Bibliography

[1] C. N. Yang and R. L. Mills, “Conservation of isotopic spin and isotopic gauge invariance,” *Phys. Rev.*, vol. 96, pp. 191–195, Oct 1954.

[2] S. Glashow, “Partial Symmetries of Weak Interactions,” *Nucl. Phys.*, vol. 22, pp. 579–588, 1961.

[3] N. Cabibbo, “Unitary Symmetry and Leptonic Decays,” *Phys. Rev. Lett.*, vol. 10, pp. 531–533, 1963.

[4] P. W. Higgs, “Broken symmetries, massless particles and gauge fields,” *Phys. Lett.*, vol. 12, pp. 132–133, 1964.

[5] G. Guralnik, C. Hagen, and T. Kibble, “Global Conservation Laws and Massless Particles,” *Phys. Rev. Lett.*, vol. 13, pp. 585–587, 1964.

[6] F. Englert and R. Brout, “Broken Symmetry and the Mass of Gauge Vector Mesons,” *Phys. Rev. Lett.*, vol. 13, pp. 321–323, 1964.

[7] P. W. Higgs, “Spontaneous Symmetry Breakdown without Massless Bosons,” *Phys. Rev.*, vol. 145, pp. 1156–1163, 1966.

[8] S. Weinberg, “A Model of Leptons,” *Phys. Rev. Lett.*, vol. 19, pp. 1264–1266, 1967.

[9] T. Kibble, “Symmetry breaking in non-Abelian gauge theories,” *Phys. Rev.*, vol. 155, pp. 1554–1561, 1967.

[10] R. P. Feynman, “Very High-Energy Collisions of Hadrons,” *Phys. Rev. Lett.*, vol. 23, pp. 1415–1417, Dec 1969.

[11] J. D. Bjorken and E. A. Paschos, “Inelastic electron-proton and γ-proton scattering and the structure of the nucleon,” *Phys. Rev.*, vol. 185, pp. 1975–1982, Sep 1969.

[12] “LHC Machine,” *JINST*, vol. 3, p. S08001, 2008.

[13] A. Buckley *et al.*, “General-purpose event generators for LHC physics,” *Phys. Rept.*, vol. 504, pp. 145–233, 2011.

[14] T. Sjöstrand, S. Ask, J. R. Christiansen, R. Corke, N. Desai, P. Ilten, S. Mrenna, S. Prestel, C. O. Rasmussen, and P. Z. Skands, “An Introduction to PYTHIA 8.2,” *Comput. Phys. Commun.*, vol. 191, pp. 159–177, 2015.

[15] J. Bellm *et al.*, “Herwig 7.1 Release Note,” 2017.

[16] E. Bothmann *et al.*, "Event Generation with Sherpa 2.2," *SciPost Phys.*, vol. 7, no. 3, p. 034, 2019.

[17] T. Sjöstrand and M. van Zijl, "A Multiple Interaction Model for the Event Structure in Hadron Collisions," *Phys. Rev.*, vol. D36, p. 2019, 1987.

[18] V. N. Gribov and L. N. Lipatov, "Deep inelastic e p scattering in perturbation theory," *Sov. J. Nucl. Phys.*, vol. 15, pp. 438–450, 1972. [Yad. Fiz.15,781(1972)].

[19] Y. L. Dokshitzer, "Calculation of the Structure Functions for Deep Inelastic Scattering and e+ e- Annihilation by Perturbation Theory in Quantum Chromodynamics.," *Sov. Phys. JETP*, vol. 46, pp. 641–653, 1977. [Zh. Eksp. Teor. Fiz.73,1216(1977)].

[20] G. Altarelli and G. Parisi, "Asymptotic Freedom in Parton Language," *Nucl. Phys.*, vol. B126, pp. 298–318, 1977.

[21] G. Gustafson and U. Pettersson, "Dipole Formulation of QCD Cascades," *Nucl. Phys.*, vol. B306, pp. 746–758, 1988.

[22] D. A. Kosower, "Antenna factorization of gauge theory amplitudes," *Phys. Rev.*, vol. D57, pp. 5410–5416, 1998.

[23] S. Catani and M. Seymour, "A General algorithm for calculating jet cross-sections in NLO QCD," *Nucl. Phys. B*, vol. 485, pp. 291–419, 1997. [Erratum: Nucl.Phys.B 510, 503–504 (1998)].

[24] S. Catani and M. Seymour, "The Dipole formalism for the calculation of QCD jet cross-sections at next-to-leading order," *Phys. Lett. B*, vol. 378, pp. 287–301, 1996.

[25] S. Catani, F. Krauss, R. Kuhn, and B. R. Webber, "QCD matrix elements + parton showers," *JHEP*, vol. 11, p. 063, 2001.

[26] B. Andersson, G. Gustafson, G. Ingelman, and T. Sjöstrand, "Parton Fragmentation and String Dynamics," *Phys. Rept.*, vol. 97, pp. 31–145, 1983.

[27] T. Sjostrand, "Jet Fragmentation of Nearby Partons," *Nucl. Phys. B*, vol. 248, pp. 469–502, 1984.

[28] B. Webber, "A QCD model for jet fragmentation including soft gluon interference," *Nuclear Physics B*, vol. 238, no. 3, pp. 492 – 528, 1984.

[29] D. Lange, "The EvtGen particle decay simulation package," *Nucl. Instrum. Meth. A*, vol. 462, pp. 152–155, 2001.

[30] K. Aamodt *et al.*, "The ALICE experiment at the CERN LHC," *JINST*, vol. 3, p. S08002, 2008.

[31] J. Adam *et al.*, "Measurement of pion, kaon and proton production in proton–proton collisions at $\sqrt{s} = 7$ TeV," *Eur. Phys. J.*, vol. C75, no. 5, p. 226, 2015.

[32] J. Adam *et al.*, "Insight into particle production mechanisms via angular correlations of identified particles in pp collisions at $\sqrt{s} = 7$ TeV," *Eur. Phys. J.*, vol. C77, no. 8, p. 569, 2017. [Erratum: Eur. Phys. J.C79,no.12,998(2019)].

[33] P. Cui, "Strangeness Production in Jets and Underlying Events in pp Collisions at $\sqrt{s} = 13$ TeV with ALICE," *JPS Conf. Proc.*, vol. 26, p. 024017, 2019.

[34] S. Chatrchyan *et al.*, "The CMS Experiment at the CERN LHC," *JINST*, vol. 3, p. S08004, 2008.

[35] V. Khachatryan *et al.*, "Observation of Long-Range Near-Side Angular Correlations in Proton-Proton Collisions at the LHC," *JHEP*, vol. 09, p. 091, 2010.

[36] D. Velicanu, "Ridge correlation structure in high multiplicity pp collisions with CMS," *J. Phys.*, vol. G38, p. 124051, 2011.

[37] G. Aad *et al.*, "The ATLAS Experiment at the CERN Large Hadron Collider," *JINST*, vol. 3, p. S08003, 2008.

[38] G. Aad *et al.*, "Charged-particle multiplicities in pp interactions measured with the ATLAS detector at the LHC," *New J. Phys.*, vol. 13, p. 053033, 2011.

[39] G. Aad, B. Abbott, D. C. Abbott, O. Abdinov, A. A. Abud, K. Abeling, D. K. Abhayasinghe, S. H. Abidi, O. S. AbouZeid, and et al., "Measurement of k_s^0 and λ^0 production in $t\bar{t}$ dileptonic events in pp collisions at $\sqrt{s} =$ tev with the atlas detector," *The European Physical Journal C*, vol. 79, Dec 2019.

[40] T. Cheng and L. Li, *Gauge Theory of Elementary Particle Physics*. 1984.

[41] F. Mandl and G. Shaw, *Quantum Field Theory*. 1 1985.

[42] R. Ellis, W. Stirling, and B. Webber, *QCD and collider physics*, vol. 8. Cambridge University Press, 2 2011.

[43] M. E. Peskin and D. V. Schroeder, *An Introduction to quantum field theory*. Reading, USA: Addison-Wesley, 1995.

[44] S. Weinberg, *The Quantum theory of fields. Vol. 1: Foundations*. Cambridge University Press, 6 2005.

[45] S. Weinberg, *The quantum theory of fields. Vol. 2: Modern applications*. Cambridge University Press, 8 2013.

[46] G. Dissertori, I. G. Knowles, and M. Schmelling, *High energy experiments and theory*. Oxford University Press, 2003.

[47] M. Srednicki, *Quantum field theory*. Cambridge University Press, 1 2007.

[48] S. L. Glashow, "The renormalizability of vector meson interactions," *Nucl. Phys.*, vol. 10, pp. 107–117, 1959.

[49] A. Salam, "Weak and Electromagnetic Interactions," *Conf. Proc. C*, vol. 680519, pp. 367–377, 1968.

[50] F. Halzen and A. D. Martin, *Quarks and Leptons: An Introductory Course in Modern Particle Physics*. 1 1984.

[51] Dirac, Paul A. M., "A Theory Of Electrons and Protons," in *Proceedings of the Royal Society A*, p. 360–365, 1930.

[52] C. Wu, E. Ambler, R. Hayward, D. Hoppes, and R. Hudson, "Experimental Test of Parity Conservation in β Decay," *Phys. Rev.*, vol. 105, pp. 1413–1414, 1957.

[53] M. Goldhaber, L. Grodzins, and A. Sunyar, "Helicity of Neutrinos," *Phys. Rev.*, vol. 109, pp. 1015–1017, 1958.

[54] Y.-R. Liu, H.-X. Chen, W. Chen, X. Liu, and S.-L. Zhu, "Pentaquark and Tetraquark States," *Prog. Part. Nucl. Phys.*, vol. 107, pp. 237–320, 2019.

[55] R. Aaij *et al.*, "Observation of the resonant character of the $Z(4430)^-$ state," *Phys. Rev. Lett.*, vol. 112, no. 22, p. 222002, 2014.

[56] R. Aaij *et al.*, "Observation of $J/\psi\phi$ structures consistent with exotic states from amplitude analysis of $B^+ \to J/\psi\phi K^+$ decays," *Phys. Rev. Lett.*, vol. 118, no. 2, p. 022003, 2017.

[57] R. Aaij *et al.*, "Amplitude analysis of $B^+ \to J/\psi\phi K^+$ decays," *Phys. Rev.*, vol. D95, no. 1, p. 012002, 2017.

[58] R. Aaij *et al.*, "Observation of $J/\psi p$ Resonances Consistent with Pentaquark States in $\Lambda_b^0 \to J/\psi K^- p$ Decays," *Phys. Rev. Lett.*, vol. 115, p. 072001, 2015.

[59] W. A. Bardeen, A. J. Buras, D. W. Duke, and T. Muta, "Deep Inelastic Scattering Beyond the Leading Order in Asymptotically Free Gauge Theories," *Phys. Rev.*, vol. D18, p. 3998, 1978.

[60] M. Tanabashi *et al.*, "Review of particle physics," *Phys. Rev. D*, vol. 98, p. 030001, Aug 2018.

[61] M. Schmelling, "Averaging correlated data," *Phys. Scripta*, vol. 51, pp. 676–679, 1995.

[62] R. Feynman, "Mathematical formulation of the quantum theory of electromagnetic interaction," *Phys. Rev.*, vol. 80, pp. 440–457, 1950.

[63] L. Faddeev and V. Popov, "Feynman Diagrams for the Yang-Mills Field," *Phys. Lett. B*, vol. 25, pp. 29–30, 1967.

[64] C. Baker *et al.*, "An Improved experimental limit on the electric dipole moment of the neutron," *Phys. Rev. Lett.*, vol. 97, p. 131801, 2006.

[65] M. Dine, "TASI lectures on the strong CP problem," in *Theoretical Advanced Study Institute in Elementary Particle Physics (TASI 2000): Flavor Physics for the Millennium*, pp. 349–369, 6 2000.

[66] J. E. Kim, "A Review on axions and the strong CP problem," *AIP Conf. Proc.*, vol. 1200, no. 1, pp. 83–92, 2010.

[67] K. Wilson and J. B. Kogut, "The Renormalization group and the epsilon expansion," *Phys. Rept.*, vol. 12, pp. 75–199, 1974.

[68] J. C. Collins, *Renormalization: An Introduction to Renormalization, The Renormalization Group, and the Operator Product Expansion*, vol. 26 of *Cambridge Monographs on Mathematical Physics*. Cambridge: Cambridge University Press, 1986.

[69] D. J. Gross and F. Wilczek, "Ultraviolet Behavior of Nonabelian Gauge Theories," *Phys. Rev. Lett.*, vol. 30, pp. 1343–1346, 1973. [,271(1973)].

[70] H. D. Politzer, "Reliable Perturbative Results for Strong Interactions?," *Phys. Rev. Lett.*, vol. 30, pp. 1346–1349, 1973. [,274(1973)].

[71] K. G. Wilson, "Confinement of Quarks," *Phys. Rev.*, vol. D10, pp. 2445–2459, 1974. [,45(1974); ,319(1974)].

[72] E. V. Shuryak, *The QCD vacuum, hadrons and the superdense matter*, vol. 71. 10 2004.

[73] C. Gattringer and C. B. Lang, *Quantum chromodynamics on the lattice*, vol. 788. Berlin: Springer, 2010.

[74] J. C. Collins and G. F. Sterman, "Soft Partons in QCD," *Nucl. Phys.*, vol. B185, pp. 172–188, 1981.

[75] J. C. Collins, D. E. Soper, and G. F. Sterman, "Factorization for Short Distance Hadron - Hadron Scattering," *Nucl. Phys.*, vol. B261, pp. 104–142, 1985.

[76] J. C. Collins, D. E. Soper, and G. F. Sterman, "Soft Gluons and Factorization," *Nucl. Phys.*, vol. B308, pp. 833–856, 1988.

[77] J. C. Collins, D. E. Soper, and G. F. Sterman, "Factorization of Hard Processes in QCD," *Adv. Ser. Direct. High Energy Phys.*, vol. 5, pp. 1–91, 1989.

[78] J. C. Collins and A. Freund, "Proof of factorization for deeply virtual Compton scattering in QCD," *Phys. Rev.*, vol. D59, p. 074009, 1999.

[79] J. Collins, "Foundations of perturbative QCD," *Camb. Monogr. Part. Phys. Nucl. Phys. Cosmol.*, vol. 32, pp. 1–624, 2011.

[80] J. R. Gaunt and W. J. Stirling, "Double Parton Distributions Incorporating Perturbative QCD Evolution and Momentum and Quark Number Sum Rules," *JHEP*, vol. 03, p. 005, 2010.

[81] M. Diehl, D. Ostermeier, and A. Schafer, "Elements of a theory for multiparton interactions in QCD," *JHEP*, vol. 03, p. 089, 2012. [Erratum: JHEP03,001(2016)].

[82] B. Blok, Yu. Dokshitser, L. Frankfurt, and M. Strikman, "pQCD physics of multiparton interactions," *Eur. Phys. J.*, vol. C72, p. 1963, 2012.

[83] A. V. Manohar and W. J. Waalewijn, "A QCD Analysis of Double Parton Scattering: Color Correlations, Interference Effects and Evolution," *Phys. Rev.*, vol. D85, p. 114009, 2012.

[84] M. Diehl, J. R. Gaunt, and K. Schönwald, "Double hard scattering without double counting," *JHEP*, vol. 06, p. 083, 2017.

[85] B. Cabouat, J. R. Gaunt, and K. Ostrolenk, "A Monte-Carlo Simulation of Double Parton Scattering," *JHEP*, vol. 11, p. 061, 2019.

[86] B. Cabouat and J. R. Gaunt, "Combining single and double parton scatterings in a parton shower," 8 2020.

[87] T. Kinoshita, "Mass singularities of Feynman amplitudes," *J. Math. Phys.*, vol. 3, pp. 650–677, 1962.

[88] T. Lee and M. Nauenberg, "Degenerate Systems and Mass Singularities," *Phys. Rev.*, vol. 133, pp. B1549–B1562, 1964.

[89] E. C. Poggio and H. R. Quinn, "Infrared behavior of zero-mass green's functions and the absence of quark confinement in perturbation theory," *Phys. Rev. D*, vol. 14, pp. 578–582, Jul 1976.

[90] G. F. Sterman, "Kinoshita's Theorem in Yang-Mills Theories," *Phys. Rev. D*, vol. 14, pp. 2123–2125, 1976.

[91] T. Sjostrand, S. Mrenna, and P. Z. Skands, "PYTHIA 6.4 Physics and Manual," *JHEP*, vol. 05, p. 026, 2006.

[92] M. Bähr *et al.*, "Herwig++ Physics and Manual," *Eur. Phys. J.*, vol. C58, pp. 639–707, 2008.

[93] J. Bellm *et al.*, "Herwig 7.2 Release Note," 2019.

[94] T. Gleisberg, S. Hoeche, F. Krauss, M. Schönherr, S. Schumann, F. Siegert, and J. Winter, "Event generation with SHERPA 1.1," *JHEP*, vol. 02, p. 007, 2009.

[95] S. Frixione and B. R. Webber, "Matching NLO QCD computations and parton shower simulations," *JHEP*, vol. 06, p. 029, 2002.

[96] P. Nason, "A New method for combining NLO QCD with shower Monte Carlo algorithms," *JHEP*, vol. 11, p. 040, 2004.

[97] L. Lonnblad, "Correcting the color dipole cascade model with fixed order matrix elements," *JHEP*, vol. 05, p. 046, 2002.

[98] K. Hamilton and P. Nason, "Improving NLO-parton shower matched simulations with higher order matrix elements," *JHEP*, vol. 06, p. 039, 2010.

[99] N. Fischer, *Improved QCD Calculations and Phenomenological Studies at the Large Hadron Collider*. PhD Thesis, Monash University, 2018.

[100] T. Gleisberg and S. Hoeche, "Comix, a new matrix element generator," *JHEP*, vol. 12, p. 039, 2008.

[101] J. Alwall, M. Herquet, F. Maltoni, O. Mattelaer, and T. Stelzer, "MadGraph 5 : Going Beyond," *JHEP*, vol. 06, p. 128, 2011.

[102] J. Alwall, R. Frederix, S. Frixione, V. Hirschi, F. Maltoni, O. Mattelaer, H. S. Shao, T. Stelzer, P. Torrielli, and M. Zaro, "The automated computation of tree-level and next-to-leading order differential cross sections, and their matching to parton shower simulations," *JHEP*, vol. 07, p. 079, 2014.

[103] K. Arnold *et al.*, "VBFNLO: A Parton level Monte Carlo for processes with electroweak bosons," *Comput. Phys. Commun.*, vol. 180, pp. 1661–1670, 2009.

[104] J. Baglio *et al.*, "VBFNLO: A Parton Level Monte Carlo for Processes with Electroweak Bosons – Manual for Version 2.7.0," 2011.

[105] J. M. Campbell and R. K. Ellis, "An Update on vector boson pair production at hadron colliders," *Phys. Rev.*, vol. D60, p. 113006, 1999.

[106] J. M. Campbell, R. K. Ellis, and C. Williams, "Vector boson pair production at the LHC," *JHEP*, vol. 07, p. 018, 2011.

[107] J. M. Campbell, R. K. Ellis, and W. T. Giele, "A Multi-Threaded Version of MCFM," *Eur. Phys. J.*, vol. C75, no. 6, p. 246, 2015.

[108] S. Platzer and M. Sjodahl, "Subleading N_c improved Parton Showers," *JHEP*, vol. 07, p. 042, 2012.

[109] T. Sjostrand, "A Model for Initial State Parton Showers," *Phys. Lett.*, vol. 157B, pp. 321–325, 1985.

[110] T. D. Gottschalk, "Backwards Evolved Initial State Parton Showers," *Nucl. Phys.*, vol. B277, pp. 700–738, 1986.

[111] W. T. Giele and E. W. N. Glover, "Higher order corrections to jet cross-sections in e+ e- annihilation," *Phys. Rev.*, vol. D46, pp. 1980–2010, 1992.

[112] M. Bengtsson and T. Sjostrand, "Coherent Parton Showers Versus Matrix Elements: Implications of PETRA - PEP Data," *Phys. Lett.*, vol. B185, p. 435, 1987.

[113] G. Marchesini and B. R. Webber, "Monte Carlo Simulation of General Hard Processes with Coherent QCD Radiation," *Nucl. Phys.*, vol. B310, pp. 461–526, 1988.

[114] S. Gieseke, P. Stephens, and B. Webber, "New formalism for QCD parton showers," *JHEP*, vol. 12, p. 045, 2003.

[115] T. Sjostrand and P. Z. Skands, "Transverse-momentum-ordered showers and interleaved multiple interactions," *Eur. Phys. J.*, vol. C39, pp. 129–154, 2005.

[116] F. Krauss, A. Schalicke, and G. Soff, "APACIC++ 2.0: A Parton cascade in C++," *Comput. Phys. Commun.*, vol. 174, pp. 876–902, 2006.

[117] L. Lonnblad, “ARIADNE version 4: A Program for simulation of QCD cascades implementing the color dipole model,” *Comput. Phys. Commun.*, vol. 71, pp. 15–31, 1992.

[118] Z. Nagy and D. E. Soper, “Matching parton showers to NLO computations,” *JHEP*, vol. 10, p. 024, 2005.

[119] W. T. Giele, D. A. Kosower, and P. Z. Skands, “A simple shower and matching algorithm,” *Phys. Rev.*, vol. D78, p. 014026, 2008.

[120] M. Dinsdale, M. Ternick, and S. Weinzierl, “Parton showers from the dipole formalism,” *Phys. Rev.*, vol. D76, p. 094003, 2007.

[121] S. Schumann and F. Krauss, “A Parton shower algorithm based on Catani-Seymour dipole factorisation,” *JHEP*, vol. 03, p. 038, 2008.

[122] J.-C. Winter and F. Krauss, “Initial-state showering based on colour dipoles connected to incoming parton lines,” *JHEP*, vol. 07, p. 040, 2008.

[123] S. Platzer and S. Gieseke, “Coherent Parton Showers with Local Recoils,” *JHEP*, vol. 01, p. 024, 2011.

[124] J. J. Lopez-Villarejo and P. Z. Skands, “Efficient Matrix-Element Matching with Sector Showers,” *JHEP*, vol. 11, p. 150, 2011.

[125] W. T. Giele, D. A. Kosower, and P. Z. Skands, “Higher-Order Corrections to Timelike Jets,” *Phys. Rev.*, vol. D84, p. 054003, 2011.

[126] M. Ritzmann, D. A. Kosower, and P. Skands, “Antenna Showers with Hadronic Initial States,” *Phys. Lett.*, vol. B718, pp. 1345–1350, 2013.

[127] L. Hartgring, E. Laenen, and P. Skands, “Antenna Showers with One-Loop Matrix Elements,” *JHEP*, vol. 10, p. 127, 2013.

[128] S. Höche and S. Prestel, “The midpoint between dipole and parton showers,” *Eur. Phys. J.*, vol. C75, no. 9, p. 461, 2015.

[129] N. Fischer, S. Prestel, M. Ritzmann, and P. Skands, “Vincia for Hadron Colliders,” *Eur. Phys. J.*, vol. C76, no. 11, p. 589, 2016.

[130] G. ’t Hooft, “A Planar Diagram Theory for Strong Interactions,” *Nucl. Phys.*, vol. B72, p. 461, 1974. [,337(1973)].

[131] E. Witten, “Baryons in the 1/n Expansion,” *Nucl. Phys.*, vol. B160, pp. 57–115, 1979.

[132] R. Kleiss and R. Verheyen, “Final-state QED Multipole Radiation in Antenna Parton Showers,” *JHEP*, vol. 11, p. 182, 2017.

[133] G. Marchesini and B. R. Webber, “Simulation of QCD Jets Including Soft Gluon Interference,” *Nucl. Phys.*, vol. B238, pp. 1–29, 1984.

[134] M. Bengtsson and T. Sjostrand, “A Comparative Study of Coherent and Noncoherent Parton Shower Evolution,” *Nucl. Phys.*, vol. B289, pp. 810–846, 1987.

[135] Z. Nagy and D. E. Soper, “Effects of subleading color in a parton shower,” *JHEP*, vol. 07, p. 119, 2015.

[136] J. Isaacson and S. Prestel, “Stochastically sampling color configurations,” *Phys. Rev.*, vol. D99, no. 1, p. 014021, 2019.

[137] S. Plätzer, M. Sjodahl, and J. Thorén, “Color matrix element corrections for parton showers,” *JHEP*, vol. 11, p. 009, 2018.

[138] M. Sjodahl and J. Thorén, “QCD multiplet bases with arbitrary parton ordering,” *JHEP*, vol. 11, p. 198, 2018.

[139] Z. Nagy and D. E. Soper, “Parton showers with more exact color evolution,” *Phys. Rev.*, vol. D99, no. 5, p. 054009, 2019.

[140] Z. Nagy and D. E. Soper, “Effect of color on rapidity gap survival,” *Phys. Rev.*, vol. D100, no. 7, p. 074012, 2019.

[141] Z. Nagy and D. E. Soper, “Exponentiating virtual imaginary contributions in a parton shower,” *Phys. Rev.*, vol. D100, no. 7, p. 074005, 2019.

[142] S. Hoeche and D. Reichelt, “Numerical resummation at full color in the strongly ordered soft gluon limit,” 2020.

[143] R. Ángeles Martínez, M. De Angelis, J. R. Forshaw, S. Plätzer, and M. H. Seymour, “Soft gluon evolution and non-global logarithms,” *JHEP*, vol. 05, p. 044, 2018.

[144] J. R. Forshaw, J. Holguin, and S. Plätzer, “Parton branching at amplitude level,” *JHEP*, vol. 08, p. 145, 2019. [JHEP08,145(2019)].

[145] H. T. Li and P. Skands, “A framework for second-order parton showers,” *Phys. Lett.*, vol. B771, pp. 59–66, 2017.

[146] S. Höche and S. Prestel, “Triple collinear emissions in parton showers,” *Phys. Rev.*, vol. D96, no. 7, p. 074017, 2017.

[147] S. Höche, F. Krauss, and S. Prestel, “Implementing NLO DGLAP evolution in Parton Showers,” *JHEP*, vol. 10, p. 093, 2017.

[148] F. Dulat, S. Höche, and S. Prestel, “Leading-Color Fully Differential Two-Loop Soft Corrections to QCD Dipole Showers,” *Phys. Rev.*, vol. D98, no. 7, p. 074013, 2018.

[149] A. J. Larkoski, J. J. Lopez-Villarejo, and P. Skands, “Helicity-Dependent Showers and Matching with VINCIA,” *Phys. Rev.*, vol. D87, no. 5, p. 054033, 2013.

[150] N. Fischer, A. Lifson, and P. Skands, “Helicity Antenna Showers for Hadron Colliders,” *Eur. Phys. J.*, vol. C77, no. 10, p. 719, 2017.

[151] J. C. Collins, “Spin Correlations in Monte Carlo Event Generators,” *Nucl. Phys.*, vol. B304, pp. 794–804, 1988.

[152] I. G. Knowles, "Angular Correlations in QCD," *Nucl. Phys.*, vol. B304, pp. 767–793, 1988.

[153] I. G. Knowles, "A Linear Algorithm for Calculating Spin Correlations in Hadronic Collisions," *Comput. Phys. Commun.*, vol. 58, pp. 271–284, 1990.

[154] I. G. Knowles, "Spin Correlations in Parton - Parton Scattering," *Nucl. Phys.*, vol. B310, pp. 571–588, 1988.

[155] P. Richardson, "Spin correlations in Monte Carlo simulations," *JHEP*, vol. 11, p. 029, 2001.

[156] Z. Nagy and D. E. Soper, "Parton showers with quantum interference: Leading color, with spin," *JHEP*, vol. 07, p. 025, 2008.

[157] P. Richardson and S. Webster, "Spin Correlations in Parton Shower Simulations," 2018.

[158] T. Sjostrand and P. Z. Skands, "Multiple interactions and the structure of beam remnants," *JHEP*, vol. 03, p. 053, 2004.

[159] J. M. Butterworth, J. R. Forshaw, and M. H. Seymour, "Multiparton interactions in photoproduction at HERA," *Z. Phys.*, vol. C72, pp. 637–646, 1996.

[160] L. Durand and H. Pi, "High-energy Nucleon Nucleus Scattering and Cosmic Ray Cross-sections," *Phys. Rev.*, vol. D38, pp. 78–84, 1988.

[161] L. Durand and H. Pi, "Semihard QCD and High-energy pp and $\bar{p}p$ Scattering," *Phys. Rev.*, vol. D40, p. 1436, 1989.

[162] I. Borozan and M. H. Seymour, "An Eikonal model for multiparticle production in hadron hadron interactions," *JHEP*, vol. 09, p. 015, 2002.

[163] M. Azarkin, P. Kotko, A. Siodmok, and M. Strikman, "Studying minijets and MPI with rapidity correlations," *Eur. Phys. J.*, vol. C79, no. 3, p. 180, 2019.

[164] J. Bellm, S. Gieseke, and P. Kirchgaesser, "Improving the description of multiple interactions in Herwig," 2019.

[165] B. Andersson, "The Lund model," *Camb. Monogr. Part. Phys. Nucl. Phys. Cosmol.*, vol. 7, pp. 1–471, 1997.

[166] J.-C. Winter, F. Krauss, and G. Soff, "A Modified cluster hadronization model," *Eur. Phys. J.*, vol. C36, pp. 381–395, 2004.

[167] H. Brooks and P. Skands, "Coherent showers in decays of colored resonances," *Phys. Rev.*, vol. D100, no. 7, p. 076006, 2019.

[168] T. Sjostrand, "High-energy physics event generation with PYTHIA 5.7 and JETSET 7.4," *Comput. Phys. Commun.*, vol. 82, pp. 74–90, 1994.

[169] S. Jadach, J. H. Kuhn, and Z. Was, "TAUOLA: A Library of Monte Carlo programs to simulate decays of polarized tau leptons," *Comput. Phys. Commun.*, vol. 64, pp. 275–299, 1990.

[170] S. Jadach, Z. Was, R. Decker, and J. H. Kuhn, "The tau decay library TAUOLA: Version 2.4," *Comput. Phys. Commun.*, vol. 76, pp. 361–380, 1993.

[171] P. Golonka, B. Kersevan, T. Pierzchala, E. Richter-Was, Z. Was, and M. Worek, "The Tauola photos F environment for the TAUOLA and PHOTOS packages: Release. 2.," *Comput. Phys. Commun.*, vol. 174, pp. 818–835, 2006.

[172] S. Agostinelli *et al.*, "GEANT4: A Simulation toolkit," *Nucl. Instrum. Meth.*, vol. A506, pp. 250–303, 2003.

[173] J. Allison *et al.*, "Recent developments in Geant4," *Nucl. Instrum. Meth.*, vol. A835, pp. 186–225, 2016.

[174] I. G. Knowles and G. D. Lafferty, "Hadronization in Z^0 decay," *J. Phys.*, vol. G23, pp. 731–789, 1997.

[175] A. Krzywicki and B. Petersson, "Breakdown of hadronic scaling or evidence for clustering?," *Phys. Rev.*, vol. D6, pp. 924–928, 1973.

[176] R. D. Field and R. P. Feynman, "Quark Elastic Scattering as a Source of High Transverse Momentum Mesons," *Phys. Rev.*, vol. D15, pp. 2590–2616, 1977.

[177] R. D. Field and R. P. Feynman, "A Parametrization of the Properties of Quark Jets," *Nucl. Phys.*, vol. B136, p. 1, 1978. [,763(1977)].

[178] B. Andersson, G. Gustafson, and C. Peterson, "A Semiclassical Model for Quark Jet Fragmentation," *Z. Phys.*, vol. C1, p. 105, 1979.

[179] B. Andersson, G. Gustafson, and B. Soderberg, "A General Model for Jet Fragmentation," *Z. Phys.*, vol. C20, p. 317, 1983.

[180] T. Sjöstrand, "Jet fragmentation of multiparton configurations in a string framework," *Nuclear Physics B*, vol. 248, no. 2, pp. 469 – 502, 1984.

[181] A. Bazavov *et al.*, "Nonperturbative QCD Simulations with 2+1 Flavors of Improved Staggered Quarks," *Rev. Mod. Phys.*, vol. 82, pp. 1349–1417, 2010.

[182] G. S. Bali, "QCD forces and heavy quark bound states," *Phys. Rept.*, vol. 343, pp. 1–136, 2001.

[183] G. S. Bali, "Casimir scaling of SU(3) static potentials," *Phys. Rev.*, vol. D62, p. 114503, 2000.

[184] P. D. B. Collins, "Regge theory and particle physics," *Phys. Rept.*, vol. 1, pp. 103–234, 1971.

[185] N. Brambilla *et al.*, "Heavy Quarkonium: Progress, Puzzles, and Opportunities," *Eur. Phys. J.*, vol. C71, p. 1534, 2011.

[186] E. Eichten, K. Gottfried, T. Kinoshita, K. D. Lane, and T.-M. Yan, "Charmonium: The Model," *Phys. Rev.*, vol. D17, p. 3090, 1978. [Erratum: Phys. Rev.D21,313(1980)].

[187] G. Ripka, "Dual superconductor models of color confinement," *Lect. Notes Phys.*, vol. 639, pp. pp.1–135, 2004.

[188] B. Andersson, G. Gustafson, G. Ingelman, and T. Sjostrand, "Baryon Production in Lepton - Nucleon Scattering and Diquark Fragmentation," *Z. Phys.*, vol. C13, p. 361, 1982.

[189] B. Andersson, G. Gustafson, and T. Sjostrand, "Baryon Production in Jet Fragmentation and Υ Decay," *Phys. Scripta*, vol. 32, p. 574, 1985.

[190] P. Eden and G. Gustafson, "Baryon production in the string fragmentation picture," *Z. Phys.*, vol. C75, pp. 41–49, 1997.

[191] M. G. Bowler, "e+ e- Production of Heavy Quarks in the String Model," *Z. Phys.*, vol. C11, p. 169, 1981.

[192] C. Peterson, D. Schlatter, I. Schmitt, and P. M. Zerwas, "Scaling Violations in Inclusive e+ e- Annihilation Spectra," *Phys. Rev.*, vol. D27, p. 105, 1983.

[193] R. Brandelik *et al.*, "Evidence for Planar Events in e+ e- Annihilation at High-Energies," *Phys. Lett. B*, vol. 86, pp. 243–249, 1979.

[194] W. Bartel *et al.*, "Experimental Study of Jets in electron - Positron Annihilation," *Phys. Lett.*, vol. 101B, pp. 129–134, 1981.

[195] W. Bartel *et al.*, "Test of Fragmentation Models by Comparison with Three Jet Events Produced in e+ e- —> Hadrons," *Phys. Lett. B*, vol. 134, p. 275, 1984.

[196] W. Bartel *et al.*, "Experimental Studies on Multi-Jet Production in e+ e- Annihilation at PETRA Energies," pp. 53–60, 1986.

[197] J. R. Christiansen and P. Z. Skands, "String Formation Beyond Leading Colour," *JHEP*, vol. 08, p. 003, 2015.

[198] K.-I. Kondo, S. Kato, A. Shibata, and T. Shinohara, "Quark confinement: Dual superconductor picture based on a non-Abelian Stokes theorem and reformulations of Yang–Mills theory," *Phys. Rept.*, vol. 579, pp. 1–226, 2015.

[199] K. Johnson, "The M.I.T. Bag Model," *Acta Phys. Polon.*, vol. B6, p. 865, 1975.

[200] K. Johnson and C. B. Thorn, "String-Like Solutions of the Bag Model," *Phys. Rev.*, vol. D13, p. 1934, 1976.

[201] S. Chun and C. Buchanan, "A Simple plausible path from QCD to successful prediction of e+ e- —> hadronization data," *Phys. Rept.*, vol. 292, pp. 239–317, 1998.

[202] X. Artru and G. Mennessier, "String model and multiproduction," *Nucl. Phys.*, vol. B70, pp. 93–115, 1974.

[203] X. Artru, "Classical String Phenomenology. 1. How Strings Work," *Phys. Rept.*, vol. 97, p. 147, 1983.

[204] T. D. Gottschalk and D. A. Morris, "A New Model for Hadronization and e^+e^- Annihilation," *Nucl. Phys.*, vol. B288, pp. 729–781, 1987.

[205] M. Cardoso, N. Cardoso, and P. Bicudo, "Lattice QCD computation of the colour fields for the static hybrid quark-gluon-antiquark system, and microscopic study of the Casimir scaling," *Phys. Rev.*, vol. D81, p. 034504, 2010.

[206] N. Cardoso, M. Cardoso, and P. Bicudo, "Inside the SU(3) quark-antiquark QCD flux tube: screening versus quantum widening," *Phys. Rev.*, vol. D88, p. 054504, 2013.

[207] P. Cea, L. Cosmai, F. Cuteri, and A. Papa, "Flux tubes in the SU(3) vacuum: London penetration depth and coherence length," *Phys. Rev.*, vol. D89, no. 9, p. 094505, 2014.

[208] P. Cea, L. Cosmai, F. Cuteri, and A. Papa, "Flux tubes at finite temperature," *JHEP*, vol. 06, p. 033, 2016.

[209] C. Bierlich, G. Gustafson, L. Lönnblad, and A. Tarasov, "Effects of Overlapping Strings in pp Collisions," *JHEP*, vol. 03, p. 148, 2015.

[210] A. Chaves, F. M. Peeters, G. A. Farias, and M. V. Milošević, "Vortex-vortex interaction in bulk superconductors: Ginzburg-landau theory," *Phys. Rev. B*, vol. 83, p. 054516, Feb 2011.

[211] L. Kramer, "Thermodynamic Behavior of Type-II Superconductors with Small κ near the Lower Critical Field," *Phys. Rev. B*, vol. 3, pp. 3821–3825, Jun 1971.

[212] D. Amati and G. Veneziano, "Preconfinement as a property of perturbative QCD," *Physics Letters B*, vol. 83, no. 1, pp. 87 – 92, 1979.

[213] S. Gieseke, P. Kirchgaeßer, and S. Plätzer, "Baryon production from cluster hadronisation," *Eur. Phys. J.*, vol. C78, no. 2, p. 99, 2018.

[214] T. Sjöstrand, "Colour reconnection and its effects on precise measurements at the LHC," 2013.

[215] S. Argyropoulos and T. Sjöstrand, "Effects of color reconnection on $t\bar{t}$ final states at the LHC," *JHEP*, vol. 11, p. 043, 2014.

[216] L. Lönnblad, "Reconnecting colored dipoles," *Z. Phys.*, vol. C70, pp. 107–114, 1996.

[217] E. Avsar, G. Gustafson, and L. Lonnblad, "Small-x dipole evolution beyond the large-N(c) imit," *JHEP*, vol. 01, p. 012, 2007.

[218] J. Bellm, "Colour Rearrangement for Dipole Showers," *Eur. Phys. J.*, vol. C78, no. 7, p. 601, 2018.

[219] S. Gieseke, P. Kirchgaeßer, S. Plätzer, and A. Siodmok, "Colour Reconnection from Soft Gluon Evolution," *JHEP*, vol. 11, p. 149, 2018.

[220] T. Sjostrand and V. A. Khoze, "On Color Rearrangement in Hadronic W+ W- Events," *Z. Phys.*, vol. C62, pp. 281–310, 1994.

[221] S. Gieseke, C. Rohr, and A. Siodmok, "Colour reconnections in Herwig++," *Eur. Phys. J.*, vol. C72, p. 2225, 2012.

[222] D. Reichelt, P. Richardson, and A. Siodmok, "Improving the Simulation of Quark and Gluon Jets with Herwig 7," *Eur. Phys. J.*, vol. C77, no. 12, p. 876, 2017.

[223] S. Kirkpatrick, C. D. Gelatt, and M. P. Vecchi, "Optimization by simulated annealing," *Science*, vol. 220, no. 4598, pp. 671–680, 1983.

[224] S. Acharya *et al.*, "Multiplicity dependence of light-flavor hadron production in pp collisions at $\sqrt{s} = 7$ TeV," *Phys. Rev.*, vol. C99, no. 2, p. 024906, 2019.

[225] C. Bierlich, G. Gustafson, L. Lönnblad, and H. Shah, "The Angantyr model for Heavy-Ion Collisions in PYTHIA8," *JHEP*, vol. 10, p. 134, 2018.

[226] C. Flensburg, G. Gustafson, and L. Lönnblad, "Inclusive and Exclusive Observables from Dipoles in High Energy Collisions," *JHEP*, vol. 08, p. 103, 2011.

[227] K. Werner, F.-M. Liu, and T. Pierog, "Parton ladder splitting and the rapidity dependence of transverse momentum spectra in deuteron-gold collisions at RHIC," *Phys. Rev.*, vol. C74, p. 044902, 2006.

[228] T. Pierog, I. Karpenko, J. M. Katzy, E. Yatsenko, and K. Werner, "EPOS LHC: Test of collective hadronization with data measured at the CERN Large Hadron Collider," *Phys. Rev.*, vol. C92, no. 3, p. 034906, 2015.

[229] A. Ortiz Velasquez, P. Christiansen, E. Cuautle Flores, I. Maldonado Cervantes, and G. Paić, "Color Reconnection and Flowlike Patterns in pp Collisions," *Phys. Rev. Lett.*, vol. 111, no. 4, p. 042001, 2013.

[230] C. Bierlich and J. R. Christiansen, "Effects of color reconnection on hadron flavor observables," *Phys. Rev.*, vol. D92, no. 9, p. 094010, 2015.

[231] N. Fischer and T. Sjöstrand, "Thermodynamical String Fragmentation," *JHEP*, vol. 01, p. 140, 2017.

[232] V. I. Shevchenko and Yu. A. Simonov, "Casimir scaling as a test of QCD vacuum," *Phys. Rev. Lett.*, vol. 85, pp. 1811–1814, 2000.

[233] C. Bierlich, G. Gustafson, and L. Lönnblad, "A shoving model for collectivity in hadronic collisions," 2016.

[234] C. Bierlich, G. Gustafson, and L. Lönnblad, "Collectivity without plasma in hadronic collisions," *Phys. Lett.*, vol. B779, pp. 58–63, 2018.

[235] K. Werner, I. Karpenko, T. Pierog, M. Bleicher, and K. Mikhailov, "Event-by-Event Simulation of the Three-Dimensional Hydrodynamic Evolution from Flux Tube Initial Conditions in Ultrarelativistic Heavy Ion Collisions," *Phys. Rev.*, vol. C82, p. 044904, 2010.

[236] G. 't Hooft, "Dimensional regularization and the renormalization group," *Nucl. Phys. B*, vol. 61, pp. 455–468, 1973.

[237] S. Weinberg, "New approach to the renormalization group," *Phys. Rev. D*, vol. 8, pp. 3497–3509, 1973.

[238] K. Abe *et al.*, "Production of pi+, pi-, K+, K-, p and anti-p in light (uds), c and b jets from Z0 decays," *Phys. Rev. D*, vol. 69, p. 072003, 2004.

[239] T. Sjöstrand, "The Development of MPI Modeling in Pythia," *Adv. Ser. Direct. High Energy Phys.*, vol. 29, pp. 191–225, 2018.

[240] K. Konishi, A. Ukawa, and G. Veneziano, "A Simple Algorithm for QCD Jets," *Phys. Lett. B*, vol. 78, pp. 243–248, 1978.

[241] K. Konishi, A. Ukawa, and G. Veneziano, "Jet Calculus: A Simple Algorithm for Resolving QCD Jets," *Nucl. Phys. B*, vol. 157, pp. 45–107, 1979.

[242] V. Shelest, A. Snigirev, and G. Zinovev, "The Multiparton Distribution Equations in QCD," *Phys. Lett. B*, vol. 113, p. 325, 1982.

[243] B. Blok, Y. Dokshitzer, L. Frankfurt, and M. Strikman, "The Four jet production at LHC and Tevatron in QCD," *Phys. Rev. D*, vol. 83, p. 071501, 2011.

[244] S. Ferreres-Solé and T. Sjöstrand, "The space–time structure of hadronization in the Lund model," *Eur. Phys. J.*, vol. C78, no. 11, p. 983, 2018.

[245] V. A. Abramovsky, E. V. Gedalin, E. G. Gurvich, and O. V. Kancheli, "Long Range Azimuthal Correlations in Multiple Production Processes at High-energies," *JETP Lett.*, vol. 47, pp. 337–339, 1988. [Pisma Zh. Eksp. Teor. Fiz.47,281(1988)].

[246] B. Andersson, G. Gustafson, J. Hakkinen, M. Ringner, and P. Sutton, "Is there screwiness at the end of the QCD cascades?," *JHEP*, vol. 09, p. 014, 1998.

[247] J. L. Albacete and A. Soto-Ontoso, "Hot spots and the hollowness of proton–proton interactions at high energies," *Phys. Lett.*, vol. B770, pp. 149–153, 2017.

Appendix A

Symmetric Lund Fragmentation Function

The symmetric Lund fragmentation function, $f(z)$, governs the fraction of lightcone momenta a hadron will take from the fragmenting string, and has the form:

$$f(z) = N\frac{(1-z)^a}{z}\exp\left(\frac{-bm_\perp^2}{z}\right), \tag{A.1}$$

where we have reproduced the fragmentation function from Sec. 3.2.2, and will use the terminology developed there. To obtain the form of the fragmentation function, the Lund model [165] starts by taking a step between two vertices which correspond to two independent string breaks. The vertices are given by the points 1 and 2 depicted in Fig. A.1, after taking many steps along the positive lightcone during the fragmentation process and producing a hadron with transverse mass $m_\perp = \sqrt{m^2 + p_\perp^2}$. One may have instead chosen to do the same process, but taking many steps along the negative lightcone, and take one more step, going from 2 to 1 consequently.

Vertex 1 has hyperbolic coordinates given by the proper time Γ, and the rapidity y of the string fragmentation:

$$\Gamma_1 = \kappa^2 x_{+1} x_{-1}, \quad y_1 = \frac{1}{2}\log\left(\frac{x_{+1}}{x_{-1}}\right) \tag{A.2}$$

where $x_{\pm 1} = t_1 \pm x_1$ are the lightcone distance variables for the vertex 1, and similarly for vertex 2. Taking steps from the positive lightcone end, the lightcone momentum in the string before the hadron is produced is $W_{+1} = \kappa x_{+1}$. The hadron takes a

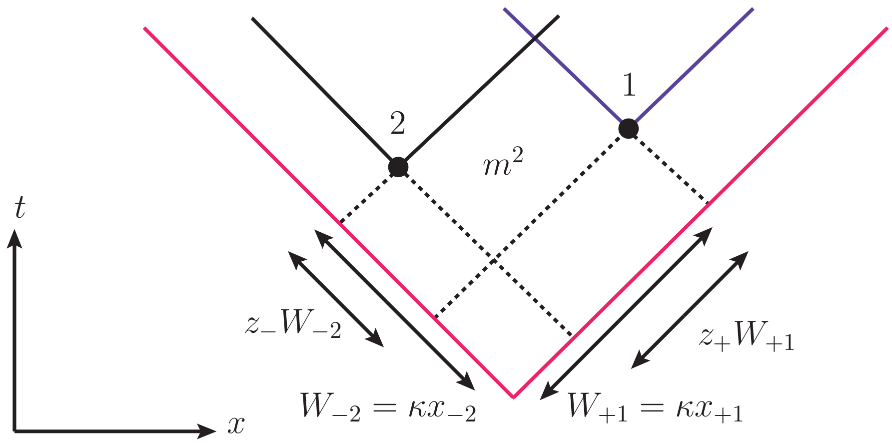

Figure A.1: Producing a hadron of mass m^2 with two string breaks at the vertices 1 and 2, taking positive lightcone momentum fraction z_+, or alternatively taking negative lightcone momenutm fraction z_-.

fraction z_+ of this. Similarly, from the negative lightcone direction, the negative momentum before producing the hadron is $W_{-2} = \kappa x_{-2}$.

The probability to arrive at vertex 1 after the many steps from the positive direction before can be written as:

$$H(\Gamma_1)\mathrm{d}\Gamma_1\mathrm{d}y_1, \tag{A.3}$$

where H is an a priori unknown probability distribution. The probability for producing a hadron with momentum fraction z_+ at vertex 1 is given by: $f(z_+)\mathrm{d}z_+$. Producing this hadron will require taking one more step to production vertex 2. Thus the joint probability is then simply the product of these two individual probabilities. Similarly, one can obtain the joint probability from the negative direction, this time taking momentum fraction z_- from the negative lightcone momentum.

Since we wish the physics to be agnostic to our choice of direction, a property known in the Lund model as left-right symmetry, the two joint probabilities are equated:

$$H(\Gamma_1)\mathrm{d}\Gamma_1\mathrm{d}y_1 f(z_+)\mathrm{d}z_+ = H(\Gamma_2)\mathrm{d}\Gamma_2\mathrm{d}y_2 f(z_-)\mathrm{d}z_-. \tag{A.4}$$

Letting the hadron mass $m^2 = z_-W_{-2}z_+W_{+1}$ be fixed, and noting that the quantities $\mathrm{d}y_1 = \mathrm{d}y_2$ are identical, one can also obtain relations between the vertex coordinates and the momentum fractions:

$$\Gamma_1 = \frac{m^2(1-z_-)}{z_-z_+}, \quad \Gamma_2 = \frac{m^2(1-z_+)}{z_-z_+}. \tag{A.5}$$

Since the proper time coordinates Γ are wholly dependent on $z_{\pm}$, one can insert them into Eq. A.4 and rewrite it as:

$$h(\Gamma_1) + g(z_+) = h(\Gamma_2) + g(z_-), \tag{A.6}$$

where $h(\Gamma) = \log(H(\Gamma))$, and $g(z) = \log(zf(z))$. One can eliminate the g dependence from Eq. A.6 by taking partial derivatives of the two momentum fractions independently.

Following the steps of [165], one can arrive at a differential equation that both vertex proper times must obey:

$$\frac{\mathrm{d}}{\mathrm{d}\Gamma}\left(\Gamma\frac{\mathrm{d}h}{\mathrm{d}\Gamma}\right) = -b, \tag{A.7}$$

where b is some constant. Solving Eq. A.7, one obtains the following form for the unknown probability distribution H:

$$H(\Gamma) = C\Gamma^a \exp\left(-b\Gamma\right), \tag{A.8}$$

for constants C and a. Using the results of Eq. A.8 and inserting into Eq. A.6, one obtains the uniquely defined form of the fragmentation function in Eq. A.1, assuming that the constant a is species-independent of the $q\bar{q}$ pair produced during the string fragmentation.